Title
Thermal Energy Transport and Conversion in Disordered Materials

Author
Zheng, Jianlin

Publication Date
2018

UNIVERSTIY OF CALIFORNIA SAN DIEGO

Thermal Energy Transport and Conversion in Disordered Materials

A dissertation submitted in partial satisfaction of the requirements for the degree Doctor of Philosophy

in

Doctor of Philosophy in Engineering Sciences (Mechanical Engineering)

by

Jianlin Zheng

Committee in charge:

Professor Renkun Chen, Chair
Professor Prabhakar R. Bandaru
Professor Shengqiang Cai
Professor Javier E. Garay
Professor Paul Yu

2018

The Dissertation of Jianlin Zheng is approved, and it is acceptable in quality and form for publication on microfilm and electronically:

Chair

University of California, San Diego

2018

Dedication

Dedicated to my family.

Table of Contents

List of Figures

List of Tables

Acknowledgements

My PhD study at UC San Diego is an important chapter of my life, and I would like to thank many people. Firstly, I am very grateful to my advisor, Prof. Renkun Chen, for giving me the opportunity to explore the exciting field of heat transfer. I didn't have lots of experimental experience before joining the group. Most of my research skills, including modeling and experiments, were obtained during my PhD study. Prof. Chen is always willing to discuss any problems that we have in our projects, and provide all the support that he has. He is one of the most diligent and smartest people that I have known, and I appreciate very much the opportunity to work with him and learn from him.

I would also like to thank my two favorite class instructors at UCSD, Prof. Prabhakar R. Bandaru and Prof. Paul Yu. I took the "Electronic and Photonic Properties of Materials" and "Semiconductor Physics" classes from them in my first year, and were very impressed by their interesting and inspiring class style. I also want to thank Prof. Javier E. Garay for allowing me to get access to the Current Activated Pressure Assisted Densification system in his lab, and providing valuable suggestions in the thermoelectric project. I also thank Prof. Shengqiang Cai for the collaboration opportunity with him and his student Qiguang He on the liquid crystal elastomers project. I sincerely appreciate the time that the professors have taken out of their busy schedules to be in the committee.

I would like to thank the two former PhD students in our group, Dr. Matthew C. Wingert and Dr. Edward Dechaumphai. I feel very fortunate to know them and work closely with them during my early stay in the group. They were very nice and always willing to discuss the problems in the measurements with me. Their joyful and easy-going personalities also brought lots of fun in the lab. I would also like to thank Dr.

Soonshin Kwon and Dr. Jaeyun Moon (now a Prof. at UNLV) for growing the nanowires or nanotubes and fabricating the suspended devices in the collaborating projects.

Additionally, I would like to thank Dr. Robin Ihnfeldt and Dr. Xia Xu (General Engineering & Research, L.L.C), Prof. Sungho Jin, Eun-Jeong Kim, and Lizzie Rubin for the great collaboration in the past 2 years. Dr. Robin Ihnfeldt was always willing to provide the materials or tools that I needed for the projects, and gave me full trust to use the great facilities at GE&R. Dr. Xia Xu was a great person to work with, very focused and hardworking at work and very humorous in daily life. I would also like to thank Dr. Yasuhiro Kodera for helping me prepare samples when I first started the thermoelectric project, and discussing the measurement data. I must also acknowledge the help from Prof. Hiroyuki Fujita's group at University of Tokyo, especially Prof. Hiroyuki Fujita, Dr. Laurent Jalabert, and Dr. Takaaki Sato, who gave me tremendous help and advices during my stay in Japan.

Furthermore, I appreciate all the help and friendship of my group mates, Shuang Cui, Sahngki Hong, Sunmi Shin, Qingyang Wang, Lizzie Rubin, Jian Zeng, and Yang Shi. I think our group members are all very hardworking and self-motivated. I appreciate the chance to finish my PhD in such a great lab. I also want to thank many of my friends in San Diego for their company and encouragement along the way.

Finally, I must thank my family for their love, support and understanding. They may not know the field that I have been studying, but they always believe I can solve the problems, and reach the goals.

I appreciate my collaborators allowing me to use the following publications in my dissertation:

Part of the chapter 1 is a reprint of M. C. Wingert, J. Zheng, S. Kwon, and R. Chen, “Thermal Transport in Amorphous Materials: A Review,” *Semiconductor Science and Technology*, 31, 113003 (2016). For this publication, I was responsible for the introduction and theoretical background parts, and wrote these two sections in the publication.

Chapter 2 is a reprint of S. Kwon*, J. Zheng*, M. C. Wingert, S. Cui, and R. Chen, “Unusually High and Anisotropic Thermal Conductivity in Amorphous Silicon Nanostructures,” *ACS Nano*, 11, 2470-2476 (2017). *These authors contributed equally to the respective works. For this publication, I performed the theoretical analysis and part of the experimental work and wrote the paper.

The majority of chapter 3 is a reprint of J. Zheng, M. C. Wingert, and R. Chen, “Simultaneous Specific Heat and Thermal Conductivity Measurement of Individual Nanostructures,” *Semiconductor Science and Technology*, 31(8), 084005 (2016), with some portions of J. Zheng*, M. C. Wingert*, E. Dechaumphai*, R. Chen, “Sub-picowatt/Kelvin Resistive Thermometry for Probing Nanoscale Thermal Transport,” *Review of Scientific Instruments*, 84, 114901 (2013). *These authors contributed equally to the respective works. For both publications, I did the modeling and experimental work and wrote the paper.

Chapter 4 is a reprint of material currently being prepared for submission for publication by J. Zheng, X. Xu, R. Ihnfeldt, L. Rubin, S. Jin, and R. Chen, “Suppression of Thermal Conductivity of Nano-grained Materials by Embedding Nanoparticles at Low Temperature,” (To be submitted). The dissertation author was the primary investigator and author of this material. For this work, I prepared and measured the samples, modeled and analyzed the results, and wrote the paper.

Vita

2012	Bachelor of Science, Huazhong University of Science and Technology
2013	Master of Science, University of California San Diego
2018	Doctor of Philosophy, University of California San Diego

Publications

1. J. Zheng, X. Xu, R. Ihnfeldt, L. Rubin, S. Jin, and R. Chen, “Suppression of Thermal Conductivity of Nano-grained Materials by Embedding Nanoparticles at Low Temperature,” (To be submitted).

2. S. Kwon*, J. Zheng*, M. C. Wingert, S. Cui, and R. Chen, “Unusually High and Anisotropic Thermal Conductivity in Amorphous Silicon Nanostructures,” *ACS Nano*, 11, 2470-2476 (2017).
   *These authors contributed equally to this work.

3. S. Shin, R. Kumar, J. W. Roh, D. S. Ko, H. S. Kim, S. I. Kim, L. Yin, S. M. Schlossberg, S. Cui, J. M. You, S. Kwon, J. Zheng, J. Wang and R. Chen, “High-Performance Screen-Printed Thermoelectric Films on Fabrics,” *Scientific reports*, 7(1), 7317 (2017).

4. M. C. Wingert, J. Zheng, S. Kwon, and R. Chen, “Thermal Transport in Amorphous Materials: A Review,” *Semiconductor Science and Technology*, 31, 113003 (2016).

5. S. Kwon, M. C. Wingert, J. Zheng, J. Xiang, and R. Chen, “Thermal Transport in Si and Ge Nanostructures in the ‘Confinement’ Regime,” *Nanoscale*, 8, 13155-13167 (2016).

6. J. Zheng, M. C. Wingert, and R. Chen, “Simultaneous Specific Heat and Thermal Conductivity Measurement of Individual Nanostructures,” *Semiconductor Science and Technology*, 31(8), 084005 (2016).

7. Q. He, Z. Wang, Y. Yan, J. Zheng, and Shengqiang Cai. "Polymer Nanofiber Reinforced Double Network Gel Composite: Strong, Tough and Transparent," *Extreme Mechanics Letters*, 9, 165 (2016).

8. J. Zheng*, M. C. Wingert*, E. Dechaumphai*, R. Chen, “Sub-picowatt/Kelvin Resistive Thermometry for Probing Nanoscale Thermal Transport,” *Review of Scientific Instruments*, 84, 114901 (2013)
   *These authors contributed equally to this work.

Abstract of the Dissertation

Thermal Energy Transport and Conversion in Disordered Materials

by

Jianlin Zheng

Doctor of Philosophy in Engineering Sciences (Mechanical Engineering)

University of California San Diego, 2018

Professor Renkun Chen, Chair

Thermal properties (thermal conductivity and specific heat) of the disordered materials, such as amorphous silicon (a-Si), polymer, and nano-crystalline semiconductors, are of significant interests for fundamental understanding of thermal transport process and for technical applications in thermal energy management and conversion. Due to the random distribution of atoms or molecules in disordered materials, the study of thermal transport is more challenging than that in crystalline materials. Understanding of the heat carrier transport behavior can be utilized to engineer the thermal properties in disordered materials, which can be applied for better devices thermal design and improving thermal energy conversion efficiency.

We have studied the size dependent thermal conductivity of a-Si thin films and nanotubes, and observed unusually high and anisotropic thermal conductivity in the isotropic a-Si nanostructure. This manifests surprisingly broad mean free path distribution of the propagating modes (propagons), which is found to range from 10 nm to 10 μm, in the disordered and isotropic structure. Constraining the long MFP propagons by boundary scattering in thin film and nanotubes explains the appreciable size effect in a-Si. Additionally, we developed a novel platform to measure the specific heat of low-dimensional disordered materials. By measuring the frequency dependent temperature rise data along the Nylon nanofibers (NFs), we are able to extract the specific heat and thermal conductivity simultaneously. While the thermal conductivity is increased by 50% over the bulk value in the 600 nm NFs, the specific heat exhibits bulk-like behavior. Finally we engineered the thermal conductivity in nano-crystalline bismuth-antimony-telluride (BST) by embedding SiO_2 or diamond nanoparticles (NPs) at temperature below 300K, which has important application in thermoelectric cooling. We have shown that the embedded NPs work as additional scattering centers for lattice vibration (or called phonons), and can efficiently scatter the long MFP phonons in BST. We have observed 23% reduction of thermal conductivity, and 15% improvement of thermoelectric figure of merit (ZT) in the 0.5 vol. % Diamond NPs mixing sample, compared to the non-NPs nano-crystalline BST.

Chapter 1: Introduction

1.1 Introduction to Disordered Materials

Disordered materials, including nano-crystalline and amorphous types, are ubiquitous and critical for modern and emerging semiconductor devices, such as amorphous Si (a-Si) photovoltaic (PV) solar cells, gate dielectrics, thermoelectric (TE) devices, solid state non-volatile phase change memory (PCM), memristors, and displays. Performance, reliability, and functionality of these devices are often closely related to operating temperature, which in turn is dictated by the thermal properties of the constituent materials, including disordered ones. Therefore, an in-depth understanding of thermal transport in disordered materials is very important for optimizing the thermal design of these devices. Moreover, from a fundamental perspective, understanding of thermal transport mechanisms in many disordered materials is still elusive, and much less advanced compared to that of crystalline materials.

Among disordered materials, a-Si is one of the most widely used in semiconductor devices due to its excellent electronic and optical properties and low cost potential [1, 2]. For instance, a-Si is an excellent material for PV solar cells (Fig. 1.1(a)) due to its direct band gap with a high optical absorption coefficient[3], lower cost, and compatibility with flexible substrates. With a lower density of localized states, hydrogenated a-Si is of more technological importance than non-passivated a-Si[3]. Hydrogenated a-Si thin film multi-junction solar cells have achieved efficiency around 13%[4]. In these multi-junction modules, a-Si thin film thickness can be as small as 10nm[5, 6]. The thermal properties of a-Si thin films could strongly influence the temperature profile within the PV modules, which directly affects the output current, voltage, and power[1]. Chow[7] showed that typically there is a 0.4% drop in cell efficiency for every 1 K above room temperature, and the associated thermal stress may cause structural damage to the PV module.

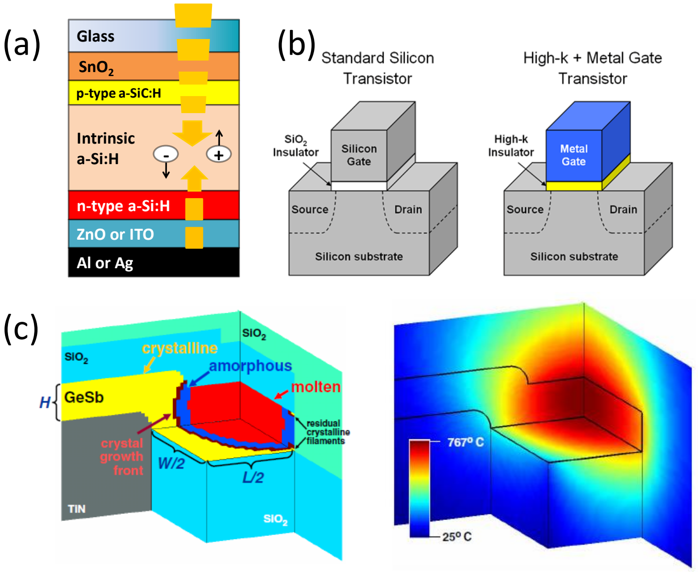

Figure 1.1: (a) Schematic view of typical a-Si:H solar cell (reproduced from ref. [8]). (b) Comparison between transistors based on SiO2 and high-k amorphous materials. High-k amorphous HfO_2 with metal gate helps to shrink the chips further. (c) Distribution of material phase (left) and temperature (right) within a PCM device[9]. (b) Reprinted with permission from ref. [10], copyright 2011 American Chemical Society. (c) Reprinted with permission from ref. [9], copyright 2006 IEEE.

Disordered materials also have a wide-range of applications in other microelectronic devices. Thin film transistors (TFTs) based on amorphous materials are widely used as switching devices in liquid crystal displays (LCD) and image sensors. Yang *et al.*[11] showed that a-Si TFTs can be formed at low temperatures on transparent plastic substrates. More recently, much effort has been made in the field of amorphous oxide TFTs, which have the advantage of room temperature fabrication and excellent uniformity over a large area[12]. A-Si thin films have also been used in microbolometer technology for infrared imaging[13, 14], owing to their high temperature coefficient of resistance (TCR) (e.g., up to 3%/K[15]) and low thermal conductivity. Understanding the thermal transport characteristics of disordered thin films is important for the thermal design and management of these novel electronic devices.

Furthermore, disordered dielectric materials, such as SiO_2, HfO_2, and SiN_x, are widely used as inter-conductor gate dielectric layers in microelectronics[16]. The thermal properties of these thin dielectric layers, including their interfaces with the semiconductor devices, is important for heat dissipation from the active device junction to the heat sinks of various transistors [16, 17]. Oxide based dielectrics are also commonly used in magneto-optic recording devices[18], cavity emitting lasers[19], and as optical coatings[20]. The thermal conductivity of SiN_x[16] and SiO_2[21] thin films have been extensively studied. The semiconductor industry has been seeking alternatives to SiO_2 as the gate dielectric in CMOS technology with higher dielectric constant (k) since the SiO_2 gate-dielectric thickness is expected to shrink below 1 nm in the near future[22], which may cause current leakage and reliability to become an important issue[23]. High-k amorphous zirconia (ZrO_2) and hafnia (HfO_2) have been proposed as promising alternatives for SiO_2 to provide required capacitance with relatively large film thickness[24]. For the first time in 2007, Intel reported that high-k materials were adopted in its 45-nm technology chips, shown in Fig. 1.1(b) and, more recently in 2014, for its 14 nm 3D tri-gate technology chips. The thermal properties of ZrO_2 and HfO_2 have not been as intensively studied as their electrical and chemical properties. However, increased research will provide meaningful information for thermal management of the electronics incorporating these thin film materials. For example, Lee and Cahill[25] showed that sputtered microcrystalline HfO_2 with an average grain size of 15 nm displays glasslike thermal conductivity (1.2 W m^{-1} K^{-1} at room temperature). However, Panzer *et al.*[26] observed film-thickness-dependent thermal conductivity of ultra-thin HfO_2 films after post-deposition thermal processing.

Disordered materials are also attractive for thermoelectric applications. Poudel *et al.*[27] showed a peak ZT of 1.4 at 373K in a nano-crystalline Bi-Sb-Te alloys. The significant ZT improvement originated from the reduction of lattice thermal conductivity, which is due to stronger boundary by the numerous grain boundaries created during high-energy ball milling process. Besides the nano-crystalline materials, it was proposed by Nolas and Goldsmid[28] in 2002 that if phonons have a longer mean free path than electrons in a crystalline material, its corresponding amorphous structure could possess a higher thermoelectric figure-of-merit (ZT) since the atomic disorder may more strongly reduce phonon thermal conductivity as opposed to electrical conductivity. This has been demonstrated in a number of amorphous oxides, such as ZnO thin films[29], NbO_2[30], and TiO_2-PbO-V_2O_5[31]. More recently, Music *et al.*[32] showed that a novel Nb-Ru-O-N amorphous thin film exhibits an order of magnitude improvement in power factor compared to other Nb based oxides or oxy-nitrides. However, thermoelectric applications with amorphous materials have not been broadly exploited. A deep understanding of thermal transport in amorphous thermoelectric materials would be beneficial for the development of this field.

Another promising application for disordered materials lies in phase change memory (PCM), which exploits the large difference between the electrical resistance between the crystalline and amorphous states of a material, such as $Ge_2Sb_2Te_5$ (GST), to store information. This crystalline-amorphous phase transition is typically induced *via* Joule heating, which often requires a high programming current (0.1-0.5mA) [33]. In order to improve the efficiency of a PCM cell, a complete understanding and modeling of the temperature profile is essential. Chen *et al.*[9] showed the great potential of phase-change random access memory (PCRAM), and modeled the 3D phase and temperature distribution in a PCM cell, shown in Fig. 1.1(c). Reifenberg *et al.*[34] investigated the impact of thermal boundary resistance in PCM cells and showed that programming current can be substantially decreased by engineering thermal anisotropy between the constituent PCM materials. Additionally, low thermal conductivity (<1 W m^{-1} K^{-1}) amorphous materials can be used to protect phase change memory devices from thermal disturbances[35] and reduce power consumption[36].

1.2 Thermal Transport in Crystalline Materials

Crystals are made of atoms in an ordered and periodic array over a length scale much larger than the lattice constant. Vibration on one or a group of atoms will be transmitted as waves through the whole crystal. These lattice vibration waves carry energy and are responsible for thermal energy transport in crystalline solids. The quantization of the collective lattice vibration energy is called a phonon. This is the microscopic origin of thermal transport in many crystalline dielectrics, including semiconductors. Because of the atomic periodicity, phonon modes can spatially extend up to the entire crystal. Phonon wave-packets, which are ensembles of phonon modes with similar frequency, can travel over long distances, often much longer than the lattice constant, before they are scattered by impurities, grain boundaries, or other phonons. The thermal conductivity (κ) contributed by phonons is determined by the energy carried by each phonon (wave packet), the group velocity of the phonons (v_g), and the average distance (Λ) that phonons travel between two successive scattering event, known as the phonon mean free path (MFP). Based on kinetic theory[37], κ in a bulk solid can be expressed as:

$$\kappa = \frac{1}{3}\sum_p \int c(\omega) v_g(\omega) \Lambda(\omega)\, d\omega \tag{1.1}$$

where c is the specific heat per unit volume of the material, 'p' is polarization, including two transverse modes and one longitudinal mode. Note that each of the parameters is frequency dependent, owing to the broadband nature of the phonon spectra.

Next we would look at the quantum mechanics description of these three parameters: volumetric specific heat 'c', group velocity 'v_g', and MFP. The energy of a phonon at frequency ω is $\hbar\omega$, where $\hbar$ is Planck's constant divided by 2π. Phonon is Bosons, and follows Bose-Einstein distribution. At a given temperature T, the equilibrium number of phonons with given energy $\hbar\omega_j$ is given as,

$$\langle n_j \rangle = \frac{1}{e^{\hbar\omega_j/k_B T} - 1} \tag{1.2}$$

The total energy of a given vibration mode j can be expressed as

$$E_j = \left(\langle n_j \rangle + \frac{1}{2}\right)\hbar\omega_j \tag{1.3}$$

From thermodynamics, we know that the volumetric heat capacity can be defined as

$$C = \frac{\partial E}{\partial T} \tag{1.4}$$

Thus, the contribution to heat capacity from a given lattice vibration mode j is

$$\mathrm{C_j} = \frac{\partial E_j}{\partial T} = k_B \left(\frac{\hbar\omega_\mathrm{j}}{k_B T}\right)^2 \frac{e^{\hbar\omega_j/k_B T}}{\left(e^{\hbar\omega_j/k_B T}-1\right)^2} \tag{1.5}$$

For a system consisting N atoms, there are total 3N lattice vibration modes, thus the total lattice heat capacity can be written as

$$\mathrm{C} = \sum_{j=1}^{3N} C_j = \sum_{j=1}^{3N} k_B \left(\frac{\hbar\omega_\mathrm{j}}{k_B T}\right)^2 \frac{e^{\hbar\omega_j/k_B T}}{\left(e^{\hbar\omega_j/k_B T}-1\right)^2} \tag{1.6}$$

In order to convert the summation of Eq. (1.6) into integration, we will introduce the concept of density of states $\mathrm{D(\omega)}$, which density of modes between ω to $\omega + \mathrm{d}\omega$, therefore,

$$\int_0^\infty \mathrm{D(\omega)}\, d\omega = 3N \tag{1.7}$$

And Eq. (1.6) can be written as

$$\mathrm{C} = \int_0^\infty k_B \left(\frac{\hbar\omega}{k_B T}\right)^2 \frac{e^{\hbar\omega/k_B T}}{\left(e^{\hbar\omega/k_B T}-1\right)^2} \mathrm{D(\omega)d\omega} \tag{1.8}$$

In order to obtain $\mathrm{D(\omega)}$, we will look at the number of allowable phonon modes in a crystal space with side length L, which can be written as

$$\mathrm{N} = \frac{\frac{4}{3}\pi \mathrm{q}^3}{\left(\frac{2\pi}{L}\right)^3} = \frac{\mathrm{V}}{6\pi^2} q^3 \tag{1.9}$$

where $\mathrm{q} = \frac{2\pi}{\lambda}$ is the wave vector, λ is the phonon wavelength, $V=L^3$ is the volume of the crystal. Thus, density of state $\mathrm{D(\omega)}$ can be derived as

$$\mathrm{D(\omega)} = \frac{1}{\mathrm{V}} \frac{dN}{d\omega} = \frac{\mathrm{q}^2}{2\pi^2} \frac{dq}{d\omega} \tag{1.10}$$

The relation between ω and q is called phonon dispersion, and $\frac{dq}{d\omega}$ is group velocity v_g, as we have seen in Eq. (1.1). Actual dispersion relationship of a crystal can be very complicated. One most common used simplified model is Debye model, which assumes linear phonon dispersion, *i.e.*, $\omega = \mathrm{v_g q}$. Thus,

$$\mathrm{D}(\omega) = \frac{\omega^2}{2\pi^2 v_g^3} \tag{1.11}$$

Note that Debye model only considers low frequency phonons, and neglect the contribution to thermal conductivity and heat capacity from high frequency phonons. Therefore, there is a cut-off frequency (Debye frequency), which can be derived by combining Eq. (1.7), Eq. (1.10), and Debye dispersion relationship, and given as

$$\omega_\mathrm{D} = \mathrm{v_g}\left(\frac{6\pi^2 N}{V}\right)^{1/3} \tag{1.12}$$

Under Debye approximation, the heat capacity in Eq. (1.8) can be simplified as

$$\mathrm{C} = \frac{3\mathrm{V}}{2\pi^2 v_g^3}\int_0^{\omega_D} k_B\left(\frac{\hbar\omega}{k_B T}\right)^2 \frac{e^{\hbar\omega/k_B T}}{\left(e^{\hbar\omega/k_B T}-1\right)^2}\omega^2 d\omega \tag{1.13}$$

Next, we will look at the mean free path distribution. The MFP in Eq. (1.1) is effective phonon MFP, which considers scattering rates by impurity, boundaries, and other phonons, and is given by Matthiessen's rule as

$$\Lambda_{eff}^{-1} = \Lambda_i^{-1} + \Lambda_{bd}^{-1} + \Lambda_u^{-1} \tag{1.14}$$

where Λ_i, Λ_bd, and Λ_u are for impurity scattering, boundary scattering, and *Umklapp* phonon-phonon scattering.

Phonons with different MFP have different capacity to carry heat. This can be quantitatively described using the so-called MFP distribution function. As an example, Fig. 1.2 shows the MFP distribution of crystalline Si (c-Si) by molecular dynamics simulation[38]. The right plot shows that the range of MFP in c-Si spans from sub-10nm up to 100 um at 277K. The MFP larger than 100um or smaller than 1nm makes negligible contribution to thermal conductivity.

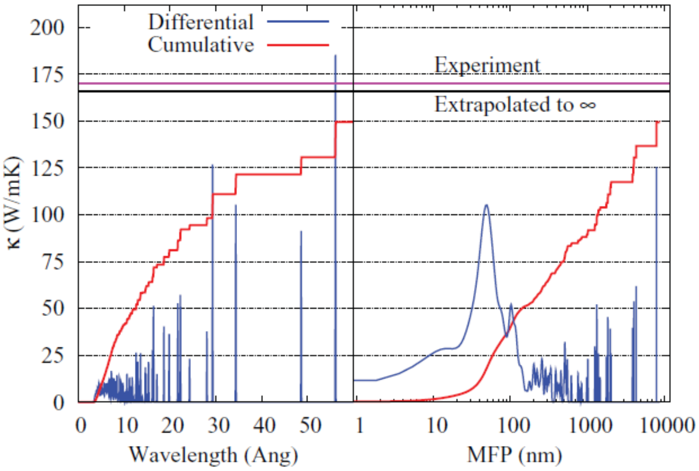

Figure 1.2: Cumulative contributions of phonons to the thermal conductivity at 277 K as a function of the wavelengths (left plot) and MFPs (right plot)[38]. The red line shows the cumulative thermal conductivities.

The MFP distribution function is very useful tool to engineer phonon transport. For example, from Fig. 1.2, if we can constrain the maximum phonon MFP up to 1 um by manipulating the scattering mechanism (e.g., increasing boundary scattering), we can reduce the total thermal conductivity down to 90 W/m-K, 40% lower than the bulk value.

Progress in modern microfabrication technology has led to the creation of numerous nanostructures, such as semiconductor thin films and nanowires. These nanostructures often exhibit distinct thermal properties compared to their bulk counterparts. Over the past decades, intensive work has been focused on understanding the effect of nanostructuring on thermal properties and its technological application. Unlike bulk materials, semiconductor nanostructures provide more opportunities for thermal property engineering. It has been well acknowledged that the phonon properties of semiconductor nanostructures can be modified, such as phonon mean-free-path (MFP)[39], group velocity[40] and density of states[41], to manipulate the thermal properties for different device applications. For example, Li *et al.*[42] observed that the thermal conductivity of crystalline Si nanowires can be reduced by two orders of magnitude compared to the corresponding bulk value. This is attributed to strong phonon-boundary scattering, which limits phonon MFPs to approximately the diameter of the nanowire, a regime called the 'Casimir limit' [43]. Hochbaum *et al.*[44] and Carrete *et al.*[45] further showed that surface roughness also plays an important role in reducing the thermal conductivity below the Casimir limit. Generally speaking, phonon transport mechanisms in crystalline materials are relatively well understood, and the size effect on thermal conductivity can often be understood through molecular simulations and semi-classical formalism (e.g., BTE).

1.3 Thermal Transport in Disordered Materials

Unlike crystals, disordered materials lack the translational symmetry and periodicity over a long distance. Therefore, the concept of extended phonon waves is not well defined, nor is the phonon wave vector, group velocity, or MFP. This imposes a tremendous challenge for modeling thermal transport in disordered solids. For numeric simulations, the lack of periodicity means that one has to be cautious when applying commonly-used periodic boundary conditions, especially when the super-cell size is small, because it imposes an artificial periodic structure on the material.

An earlier theoretical framework on heat conduction in amorphous materials was first proposed by Einstein[46] and later refined by Slack[47]. This theory is based on the assumption of independent or non-correlated vibrations among neighboring atoms or lattices, which is in contrast to that of extended waves in crystals. Heat conduction is described by a ‘random walk’ of these independent oscillators, each at a characteristic frequency, the Einstein frequency. Slack [47] formulated this problem by equating the minimum MFP to be the same as the wavelength of the phonon, namely $\Lambda = \lambda$. The thermal conductivity obtained from this model is known as the ‘minimum thermal conductivity’, κ_{min}. In 1992, Cahill *et al.*[48] further extended this model by dividing the sample into regions of size $\lambda/2$, with velocity being the low-frequency speed of sound (*i.e.*, Debye model). The MFP of each oscillator is assumed to be $\lambda/2$. The thermal conductivity can be formulated as the sum of three Debye integrals[48]:

$$\kappa_{min} = \left(\frac{\pi}{6}\right)^{\frac{1}{3}} k_B n^{\frac{2}{3}} \sum_i v_g \left(\frac{T}{\Theta_D}\right)^2 \int_0^{\Theta_D/T} \frac{x^3 e^x}{(e^x-1)^2} dx \tag{1.15}$$

which considers three acoustic modes with speed of sound, v_i, and the Debye temperature, Θ_D [48]. This model works very well for a large number of disordered materials, as shown in Figure 1.3.

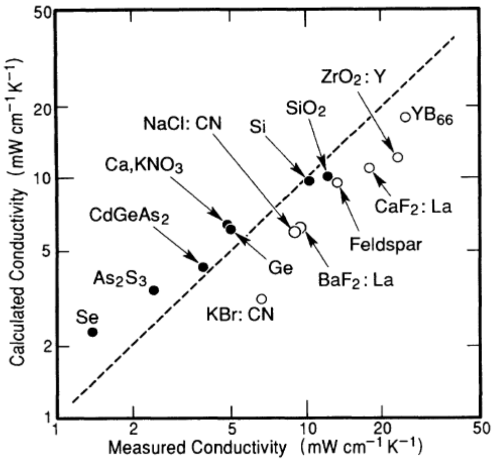

Figure 1.3: Calculated (based on Eq. (1.15)) vs. measured minimum conductivity at room temperature. Reprinted with permission from ref. [48], copyright 1992 American Physical Society.

While showing excellent agreement with many experimental data, one of the conceptual difficulties of the minimum thermal conductivity model is that the MFP is comparable to wavelength, so the mode wave-vector, velocity, and mean free path cannot be well defined to justify the use of Eq. (1.1), which is based on the BTE. Subsequently, Allen and Feldman studied thermal transport mechanism in amorphous materials theoretically and numerically[49, 50] and proposed to use an alternative formula, $\kappa = \frac{1}{V}\sum_i C_i(T)/D_i$, where $C_i(T)$ is the specific heat of the i^{th} mode and D_i is the "mode diffusivity". They found that the modes described by this equation are neither localized (which would have $D = 0$) nor propagating, but rather carry the heat through intrinsic harmonic diffusion with the aforementioned diffusivity. Hence, these modes are known as 'diffusons'. Their numerical calculation on a-Si with a 1000-atom supercell further showed that the majority of the modes are diffusons. If one would relate the diffusivity as 'diffusons'. Their numerical calculation on a-Si with a 1000-atom supercell further showed that the majority of the modes are diffusons. If one would relate the diffusivity and MFP through $D_k = \frac{1}{3}v\Lambda$, they found that Λ would be very small (only a few Å), which is consistent with the assumption used in the minimum thermal conductivity theory. However, unlike the treatment used in the Boltzmann theory, the wave vectors, and hence the modal velocity and MFP, of the diffusons are not well defined. Subsequently, Allen, Feldman and others [51] further extended the model and classified the vibrational modes into three different categories: propagons, diffusons, and locons (localized modes). Propagons are phonon-like modes which occupy the bottom of the frequency spectrum, have well defined wave vectors, travel at the sound velocity over distances greater than

$2a$, and contribute to about 4% of the total number of modes, while diffusons and locons contribute to about 93% and 3%, respectively, as shown in Fig. 1.4 (a).

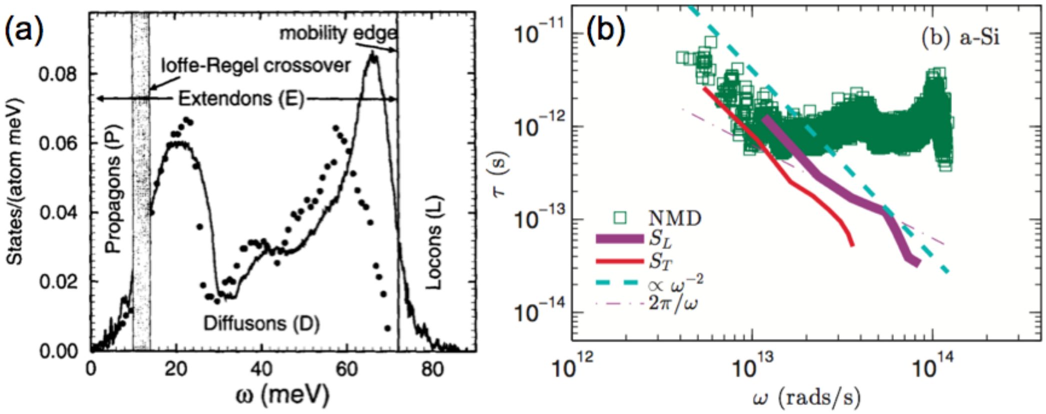

Figure 1.4: (a) Vibrational density of states in amorphous silicon (a-Si). (b) Calculated lifetime (τ) of propagons in a-Si, using equilibrium molecular dynamics (EMD), which follow a $\tau{\sim}\omega^{-2}$scaling for $\omega < 10^{13}$ rad/s, larger than the Ioffe-Regel limit ($\tau = 2\pi/\omega$). (a) Reprinted with permission from ref. [51], copyright 1999 Taylor & Francis Ltd. (b) Reprinted with permission from ref. [52], copyright 2014 American Physical Society.

One of the remaining issues in the studies by Feldman *et al.*[49] was the contribution of the progagons to the total κ of a-Si. Since the propagons are expected to have long MFPs, the small cell size (1000 atoms in ref. [49] and 4096 atoms in ref. [51], or super-cell side length of 28 Å and 44 Å, respectively) could have limited the calculated MFP of propagons and consequently their contribution to the total κ. The computed thermal conductivity (~1 W m^{-1} K^{-1} at 300 K), albeit being close to the experimental data available at the time[53], was found to be smaller than several more recent experimental results, which could be as high as 4 W m^{-1} K^{-1}, as we shall discuss later in Section 3. Recent MD and theoretical studies by He *et al.*[54] and Larkin and McGaughey[52] found that propagons could contribute significantly, up to 40% [52] to half[54], of the total κ of a-Si.

They found that the MFP of propagons can range from ~10 nm up to ~1 μm. Additionally, Larkin and McGaughey[52] also calculated the lifetime (τ) of the propagons using equilibrium MD (EMD), and showed that the simulated results follow the $\tau{\sim}\omega^{-2}$scaling for $\omega < 10^{13}$ rad/s (Fig. 1.4b). This indicates that the lifetimes are larger than the Ioffe-Regel limit, namely, $\tau = 2\pi/\omega$. The agreement between the simulation results and the structure factor time scale ($\tau{\sim}\omega^{-2}$) indicates that these low frequency modes are propagating[52]. In addition, Larkin and McGaughey[52] found that the contribution of propagons to κ of a-SiO_2 is very small (~0.1 W m^{-1} K^{-1}). More recently, Lv and Henry[55] computed the thermal conductivity of a-Si using Green-Kubo modal analysis, in which they combined lattice dynamics formalism with the Green-Kubo formula. The advantage of this method is that one can directly obtain modal contributions to thermal conductivity (using the Green-Kubo formula) without needing to define phonon velocity.

1.4 Thermoelectric Cooling

The study of thermoelectrics (TE) is of fundamental interest for the development of various techniques including refrigeration and waste heat recycling. However, most of the recent research work are focused on the application of waste heat recycling, which requires high TE efficiency at high temperature (>300K). The research in the low temperature range (<300K), which is very important for thermoelectric cooling application, are much less. The TE cooling is an appealing technique due to many advantages, such as quietness, compactness, fast response, and local cooling. TE cooling is firstly discovered by Peltier back to early 1800s. He found that the bismuth-antimony thermocouple junction will be cooled down by passing current from one direction, whereas when the current is passed from the other direction, the junction is heated up. This phenomenon is called Peltier effect, and it's the base of TE cooling devices, as shown in Fig. 1.5[56]. When current is passing through the p-type and n-type TE materials, the majority carriers absorb the heat from the cold side, and reject the heat to the hot side (heat sink), thus providing refrigeration capability.

The TE performance of a material is determined by the material's figure of merit,

$$\mathrm{ZT} = \frac{\mathrm{S}^2\sigma\mathrm{T}}{\kappa} \tag{1.16}$$

where S is Seebeck coefficient, σ is electric conductivity, $S^2\sigma$ is called power factor, T is temperature, κ is thermal conductivity, which includes electronic (κ_e) and lattice thermal conductivity (κ_{lat}).

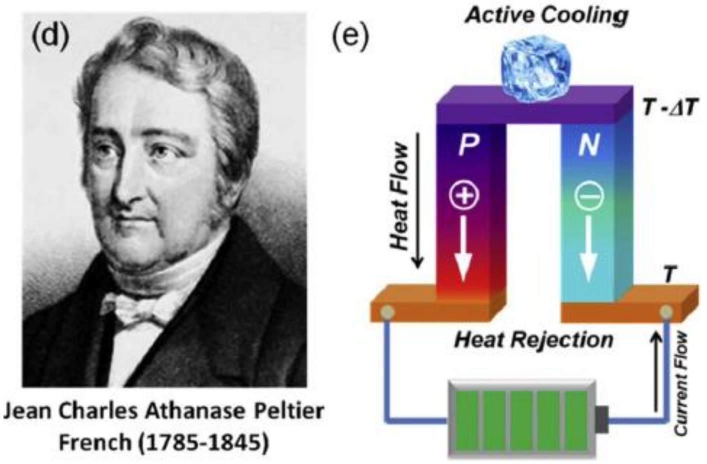

Figure 1.5: Schematic of Peltier effect for the active refrigeration. By passing current through the two TE legs, the carriers (electrons in the n-type leg and holes in the p-type leg) will absorb heat from the upper junction and release heat at the lower junction[56].

Based on Eq. (1.16), a good TE material candidate should have high Seebeck coefficient, which is defined as thermo voltage generated at certain temperature gradient across the sample, high electrical conductivity to reduce the parasitic joule heating, and low thermal conductivity to maintain the temperature gradient. ZT is closely related to the TE cooling efficiency. The higher the ZT number is, the better the TE performance will be. The relation between the TE cooling efficiency, the hot side temperature T_h, cold side temperature T_c, and ZT can be expressed as

$$\eta_c = \frac{T_h}{T_h - T_c}\left(\frac{\sqrt{1+ZT_{avg}} - T_h/T_c}{\sqrt{1+ZT_{avg}}+1}\right) \tag{1.17}$$

where ZT_{avg} is the average ZT value for both p-type and n-type legs shown in Fig. 4., and for each leg, it is averaged over the ZT temperature dependent curve between T_h and T_c, and is shown as

$$ZT_{avg} = \frac{1}{T_h - T_c}\int_{T_c}^{T_h} ZT\,dT \tag{1.18}$$

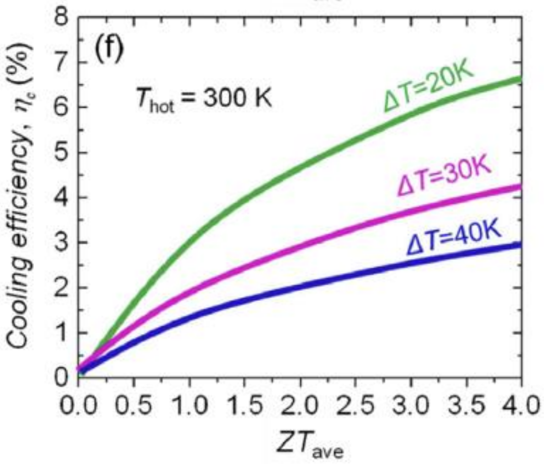

Figure 1.6: TE Cooling efficiency as a function of ZT_{avg} at different temperature difference[56].

Figure 1.6 shows the TE cooling efficiency η_c as a function of ZT_{avg} at different temperature difference ($\Delta T = 20K, 30K, \text{and } 40K$) assuming T_h=300K. The higher the ZT_{avg} is, the higher the η_c will be. And at the same ZT_{avg}, smaller temperature difference gives higher TE cooling efficiency. This is because of the reduction of the conduction heat loss through the legs at smaller temperature difference.

As discussed above, we can improve the ZT by maximizing the $S^2\sigma$ while reducing the κ ($\kappa = \kappa_e + \kappa_{lat}$). However, the interdependency between the S, σ, and κ_e limits the improvement of ZT. Figure 1.7 shows the carrier concentration dependency of S, σ, κ_e, and ZT. With increasing carrier concentration (n_e), the σ is increasing but the Seebeck coefficient is decreasing. The maximum power factor $S^2\sigma$ locates at $n_e = 10^{20}\ cm^{-3}$. Since κ_e and σ follow the Wiedemann–Franz law ($\kappa_e = L\sigma T$), where 'L' is Lorenz number, κ_e is increasing as the carrier concentration increases. The only independent parameter is lattice thermal conductivity κ_{lat}. Therefore, one of the most common way to improve ZT is to reduce the κ_{lat}.

According to Eq. (1.1), κ_{lat} can be reduced by limiting the MFP of phonons, which depends on the scattering mechanisms in the materials. Enhance the impurity scattering and boundary scattering can reduced the corresponding MFP Λ_i and Λ_{bd}, respectively, as shown in Eq. (1.14). Intensive research effort has been focused on reducing the κ_{lat} by introducing more impurity and boundary scattering in nanostructure materials. For example, Poudel *et al.*[27] found that the ZT of Bi-Sb-Te, which is one of the most commonly used TE materials at low temperature, can be improved up to 1.2 at room temperature by high energy ball milling. The ball milling process created high density of grain boundaries that strongly enhances the scattering of phonon, leading to reduction of κ_{lat} while the power factor remains similar value. Additionally, Kim *et al.*[57] showed the efficiency in $Bi_{0.5}Sb_{1.5}Te_3$ can be further improved by quickly squeezing out excess liquid during compaction. This method introduces dislocation arrays at grain boundaries, which can effectively scatter the mid-frequency phonons, and leads to further reduction of lattice thermal conductivity. The ZT can be further enhanced up to 1.86 at 320 K. Biswas *et al.*[58] showed that the nanostructure can be optimized to include various scattering sources, such as atomic scale doping, nano-precipitates, and mesocale grain boundaries. This optimal nanostrucutre has been shown to be able to scattering different MFP phonons, and the figure of merit ZT is up 2.2 at 915 K.

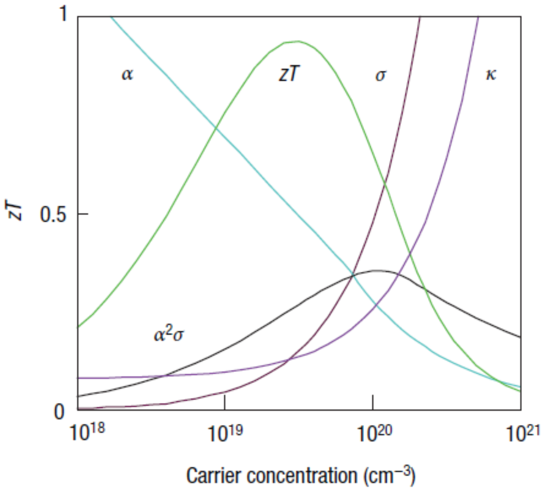

Figure 1.7: ZT as a function of carrier concentration[59]. The carrier concentration dependency of Seebeck coefficient (α), electrical (σ), thermal conductivity (κ), and power factor ($\alpha^2\sigma$) are also shown schematically on the same plot.

1.5 Thesis Objectives

Thermal properties of disordered materials are of great importance in both fundamental theoretical understanding of thermal transport and the broad practical applications. In this thesis, we are mainly focused on two questions: (1) understand the transport behavior of propagating lattice vibration modes (propagons) in amorphous solids; (2) Phonon engineering in nano-crystalline materials by embedding nanoparticles (NPs). We have done following work to answer the questions.

We have fabricated amorphous silicon (a-Si) films with thickness from 26nm to 1.6 um and nanotubes (NTs) with shell thickness from 5nm to 100 nm. By studying the temperature dependent and size dependent thermal conductivity of the a-Si films and NTs, we observed unusually high and anisotropic thermal conductivity in the isotropic a-Si nanostructure. This manifests surprisingly broad mean free path distribution of the propagating modes (propagons), which is found to range from 10 nm to 10 μm. And we unambiguously showed that the thermal conductivity of 'bulk' a-Si can be up to 5.5 W/m-K in experiment, which is important information for the future research and development on a-Si based devices.

Since some NTs and films have thermal conductance as low as hundreds of pW/K, in order to improve the measurement resolution, we developed a platform based on modulated heating. By selecting appropriate measurement frequency, the measurement platform can not only measure the thermal conductivity, but also measure the specific heat. The platform has been calibrated with SiO2 NT and NWs for thermal conductivity measurement, and specific heat measurement on Nylon-11 nanofibers (NFs).

Finally, we engineered the phonon transport in nano-grained BST at low temperature. Theoretical modeling shows that the transmission of long MFP phonons through the grain boundaries can be up to 1 at low temperature. If we can scatter these long MFP phonons, the thermal conductivity can be further reduced at low temperature. The strategy that we proposed is to embed NPs into the nano-grained BST matrix. We observed significant reduction of thermal conductivity in the NPs/BST samples. The scattering strength of two types of NPs (SiO2 and diamond) has been compared, and we found the diamond NPs has stronger scattering due to the larger thermal boundary resistance in diamond/BST interface. With the further reduction of thermal conductivity, we successfully achieved improved thermoelectric figure of merit in the diamond/BST, compared with the non-NPs BST.

1.6 Organization of the Thesis

Chapter 1 compares the thermal transport theory in crystalline and disordered materials, and gives an overview of thermoelectric principle and application in cooling.

Chapter 2 describes the temperature dependent and thickness dependent thermal conductivity of a-Si films and NTs, showing that the size effect occurs at thickness down to 5 nm, and that the reconstructed MFP spans from 10 nm to 10 μm.

Chapter 3 details the measurement platform that can measure the thermal conductivity and specific heat simultaneously, and demonstrates this technique by measuring the thermal conductivity of Nylon-11 NFs.

Chapter 4 discusses the enhanced phonon scattering by embedded NPs in nano-grained BST. Significant reduction of thermal conductivity has been achieved in the diamond NPs mixing samples, thus improving the thermoelectric figure of merit.

Chapter 5 summarizes the thesis and discusses the potential future work.

Acknowledgments

Part of the chapter 1 is a reprint of M. C. Wingert, J. Zheng, S. Kwon, and R. Chen, “Thermal Transport in Amorphous Materials: A Review,” Semiconductor Science and Technology, 31, 113003 (2016).

References

1. E. Radziemska, Progress in Energy and Combustion Science **29** (5), 407-424 (2003).

2. P. Lechner and H. Schade, Progress in Photovoltaics: Research and Applications **10** (2), 85-97 (2002).

3. S. R. O. a. A. Madan, Nature **276** (1978).

4. T. Matsui, H. Sai, K. Saito and M. Kondo, Progress in Photovoltaics: Research and Applications **21** (6), 1363-1369 (2013).

5. K. R. D. E. Carlson, R. R. Arya, F. Willing, and L. Yang, J. Mater. Res. **13** (1998).

6. C. H. a. H. W. S. A. Goetzbergera, Materials Science and Engineering R **40** (2003).

7. T. T. Chow, Applied Energy **87** (2), 365-379 (2010).

8. R. E. I. Schropp and M. Zeman, Ieee T Electron Dev **46** (1999).

9. C. T. R. Y. C. Chen, S. Raoux, G. W. Burr, S. H. Chen, R. M. Shelby, M. Salinga, W. P. Risk, T. D. Happ, G. M. McClelland, M. Breitwisch, A. Schrott, J. B. Philipp, M. H. Lee, R. Cheek, T. Nirschl, M. Lamorey, C. F. Chen, E. Joseph, S. Zaidi, B. Yee, H. L. Lung, R. Bergmann and C. Lam, International Electron Devices Meeting, San Francisco, CA **777** (2006).

10. Internet resource: https://pubs.acs.org/cen/news/85/i06/8506intel.html

11. C. S. Yang, L. L. Smith, C. B. Arthur and G. N. Parsons, Journal of Vacuum Science & Technology B: Microelectronics and Nanometer Structures **18** (2), 683 (2000).

12. J. S. Park, W.-J. Maeng, H.-S. Kim and J.-S. Park, Thin solid films **520** (6), 1679-1693 (2012).

13. L. Dong, R. Yue and L. Liu, Journal of Microelectromechanical Systems **14** (5) (2005).

14. L. Dong, R. Yue and L. Liu, The 12th International Conference on Solid State Sensors, Actuators and Microsystems (2003).

15. A. Heredia, F.J. De la Hidalga, A. Torres and A. Jaramillo, Proc. The Electrochemical Society (2003).

16. K. E. Goodson, M. I. Flik, L. T. Su and D. A. Antoniadis, Journal of Heat Transfer **116** (2), 317-324 (1994).

17. D. G. Cahill, Microscale Therm Eng **1** (2), 85-109 (1997).

18. E. C. G. M. H. Kryder, T. W. McDaniel, W. A. Challener, R. E. Rottmayer, G. Ju, Y. T. Hsia, and M. F. Erden, Proceedings of the IEEE **96** (2008).

19. A. M. K. L. Lear, K. D. Choquette, S. P. Kilcoyne, R. P. Schneider Jr, and K. M. Geib, Electronics Letters (1996).

20. H. U. N. Kaiser, U. B. Schallenberg, B. Anton, U. Kaiser, K. Mann, and E. Eva, Thin solid films **260** (1995).

21. S. M. Lee and D. G. Cahill, J Appl Phys **81** (6), 2590 (1997).

22. "International Technology Roadmap for Semiconductors (ITRS)," http://public.itrs.net.

23. D. Ceresoli and D. Vanderbilt, Phys Rev B **74** (12) (2006).

24. B. H. Lee, L. Kang, R. Nieh, W.-J. Qi and J. C. Lee, Applied Physics Letters **76** (14), 1926 (2000).

25. S. M. Lee, D. G. Cahill and T. H. Allen, Physical Review B **52** (1), 253-257 (1995).

26. M. A. Panzer, M. Shandalov, J. A. Rowlette, Y. Oshima, C. Yi Wei, P. C. McIntyre and K. E. Goodson, Electron Device Letters, IEEE **30** (12), 1269-1271 (2009).

27. B. Poudel, Q. Hao, Y. Ma, Y. Lan, A. Minnich, B. Yu, X. Yan, D. Wang, A. Muto and D. Vashaee, Science **320** (5876), 634-638 (2008).

28. G. S. N. a. H. J. Goldsmid, Phys. stat. sol. (a) **194** (2002).

29. M. O. Y. Inoue, T. Kawahara, Y. Okamoto and J. Morimoto, Materials Transactions **46** (2005).

30. D. Music, Y.-T. Chen, P. Bliem and R. W. Geyer, Journal of Physics D: Applied Physics **48** (27), 275301 (2015).

31. K. V. Ramesh and D. L. Sastry, Physica B: Condensed Matter **387** (1-2), 45-51 (2007).

32. D. Music, R. W. Geyer and M. Hans, Physica B: Condensed Matter **479**, 96-100 (2015).

33. F. Xiong, A. Liao and E. Pop, Appl Phys Lett **95** (24), 243103 (2009).

34. J. P. Reifenberg, D. L. Kencke and K. E. Goodson, Ieee Electr Device L **29** (10), 1112-1114 (2008).

35. T.-J. Ha, S. Shin, H. Keun Kim, M.-H. Hong, C.-S. Park, H. Hee Cho, D. Jin Choi and H.-H. Park, Applied Physics Letters **102** (14), 144102 (2013).

36. T.-J. Ha, H. K. Kim, D. J. Choi, S. Shin, H. H. Cho, H. W. Jang, S.-J. Yoon and H.-H. Park, Microporous and Mesoporous Materials **163**, 321-325 (2012).

37. G. Chen, Nanoscale Energy Transport and Conversion: A Parallel Treatment of Electrons, Molecules, Phonons, and Photons (Oxford University Press, 2005).

38. K. Esfarjani, G. Chen and H. T. Stokes, Physical Review B **84** (8), 085204 (2011).

39. Z. Tian, S. Lee and G. Chen, Journal of Heat Transfer **135** (6), 061605-061605 (2013).

40. J. Zou and A. Balandin, J Appl Phys **89** (5), 2932 (2001).

41. T. W. O. a. C. M. L. J. Hu, Acc. Chem. Res. **32** (1999).

42. D. Li, Y. Wu, P. Kim, L. Shi, P. Yang and A. Majumdar, Applied Physics Letters **83** (14), 2934-2936 (2003).

43. H. B. G. Casimir, Physica **5** (1938).

44. A. I. Hochbaum, R. Chen, R. D. Delgado, W. Liang, E. C. Garnett, M. Najarian, A. Majumdar and P. Yang, Nature **451** (7175), 163-167 (2008).

45. J. Carrete, L. J. Gallego, L. M. Varela and N. Mingo, Phys Rev B **84** (7) (2011).

46. A. Einstein, Ann. Phys. **340** (1911).

47. G. A. Slack, Solid State Physics (1979).

48. D. G. Cahill, S. K. Watson and R. O. Pohl, Physical Review B **46** (10), 6131-6140 (1992).

49. J. L. Feldman, M. D. Kluge, P. B. Allen and F. Wooten, Physical Review B **48** (17), 12589-12602 (1993).

50. P. B. Allen and J. L. Feldman, Physical Review B **48** (17), 12581-12588 (1993).

51. P. B. Allen, J. L. Feldman, J. Fabian and F. Wooten, Philos Mag B **79** (11-12), 1715-1731 (1999).

52. J. M. Larkin and A. J. H. McGaughey, Physical Review B **89** (14), 144303 (2014).

53. D. G. Cahill, H. E. Fischer, T. Klitsner, E. T. Swartz and R. O. Pohl, Journal of Vacuum Science & Technology A **7** (3), 1259-1266 (1989).

54. Y. He, D. Donadio and G. Galli, Appl Phys Lett **98** (14), 144101 (2011).

55. W. Lv and A. Henry, New Journal of Physics **18** (1), 013028 (2016).

56. X. Zhang and L.-D. Zhao, Journal of Materiomics **1** (2), 92-105 (2015).

57. S. I. Kim, K. H. Lee, H. A. Mun, H. S. Kim, S. W. Hwang, J. W. Roh, D. J. Yang, W. H. Shin, X. S. Li and Y. H. Lee, Science **348** (6230), 109-114 (2015).

58. K. Biswas, J. He, I. D. Blum, C.-I. Wu, T. P. Hogan, D. N. Seidman, V. P. Dravid and M. G. Kanatzidis, Nature **489** (7416), 414 (2012).

59. G. J. Snyder and E. S. Toberer, Nat Mater **7** (2), 105 (2008).

Chapter 2: Thermal Conductivity of Amorphous Silicon Films and Nanotubes

2.1 Introduction

Amorphous Si (a-Si) nanostructures are being broadly used numerous electronic and optoelectronic devices, such as solar cells[1], infrared thermal sensors[2, 3], transistors[4, 5], and displays[6]. Thermal management of these devices is often critical for their performance, reliability, and lifetime[7]. Thermal transport in a-Si, and more generally in amorphous materials, has been traditionally described by the 'amorphous limit' model that can be traced back to Einstein in 1911[8], who attributed heat conduction in disordered solids to random walk of independent oscillators with a characteristic frequency, known as the Einstein frequency. Subsequently, Slack[9], and Cahill and Pohl[10] refined Einstein's concept and proposed the widely-used minimum thermal conductivity (κ_{min}) model in disordered solids, referred to as the 'amorphous limit'. This model has worked effectively in explaining κ of a large number of amorphous materials, such as oxides[11-13].

However, thermal conductivity of a-Si garnered tremendous renewed interests in recent years as measurements[14-23] showed that thermal conductivity of a-Si can be considerably higher than the amorphous limit for a-Si, which is around ~1 W.m^{-1}K^{-1}. A summary of prior κ measurement results of a-Si is shown in Figure 2.1. While the measured κ values scatter, the general trend was that κ is close to the κ_{min} (~1 W.m^{-1}K^{-1}) for a-Si, when the film thickness (t) is ≤ 100 nm. This thermal conductivity is believed to be dominated by non-propagating higher-frequency modes, known as 'diffusons', as originally studied by Allen and Feldman[24-26]. However, for films greater than 1μm thick, κ measurement can be higher than 3 W.m^{-1}K^{-1}. This extra thermal conductivity is believed to be contributed by phonon-like propagating modes, referred to as 'propagons'[24-26].

The observed size dependent thermal conductivity provided insights into the mean free path (MFP) distribution of propagon in a-Si. As the κ only starts increasing with the thickness when t is ≥ 100 nm, these prior results suggested that the lower bound of propagon MFP must be considerably larger than 100 nm, otherwise propagon contribution would have been observed in films with $t < 100$ nm. This would mean a large discontinuity in the MFP in the transition from diffusons (interatomic distance) to propagons (> 100 nm). However, recent molecular dynamics (MD) and theoretical studies[27, 28] showed a smooth transition in the diffusivity, which is proportional to the MFP, from diffusons to propagons. These studies further showed that propagon MFP can range from ~10 nm to ~1 μm, but the bulk κ value is considerably lower than 4 W.m^{-1}K^{-1}. Clearly, there is still no consensus on the MFP distribution of propagons and the bulk 'κ' value of a-Si. Therefore, quantifying the MFP distribution of propagon in a-Si has fundamental significance in understanding thermal management of a large number devices based on a-Si nanostructures. Furthermore, it will shed light on the century-old problem of thermal transport in disordered solids , which is important to the general field of nano-phononics[29-31].

This discrepancy motivated us to re-examine the thermal conductivity of a-Si nanostructures and subsequently quantify its propagon MFP distribution. We realized that all but one[32] of the prior a-Si film κ measurements were done along the cross-plane direction. These measurements, most commonly using the 3ω [15, 17] or time-domain thermal reflectance (TDTR) method[16, 18], normally yield total cross-plane thermal resistance, which also includes the contact resistance (R_c) between the film and the substrate as well as the metal transducers. For films with very small thickness, e.g., t=50 nm, the intrinsic thermal resistance of the films is $R_{a-Si} = \mathrm{t}/\kappa \leq 5 \times 10^{-8}\ \mathrm{m}^2.\mathrm{K}.\mathrm{W}^{-1}$ (assuming $\kappa \geq 1$ W.m^{-1}K^{-1}), which is on the same order of magnitude as solid-solid interfacial thermal resistance[33]. Thus it is difficult to separate film resistance and R_c, resulting in a relative large uncertainty for the measured κ, especially for thin films ($t <$ 100 nm), as shown in our plot of reported κ values (Figure 2.1) and in Braun *et al.*'s work[14]. This issue is further complicated due to the quasi-ballistic transport nature of propagons across the film thickness[34].

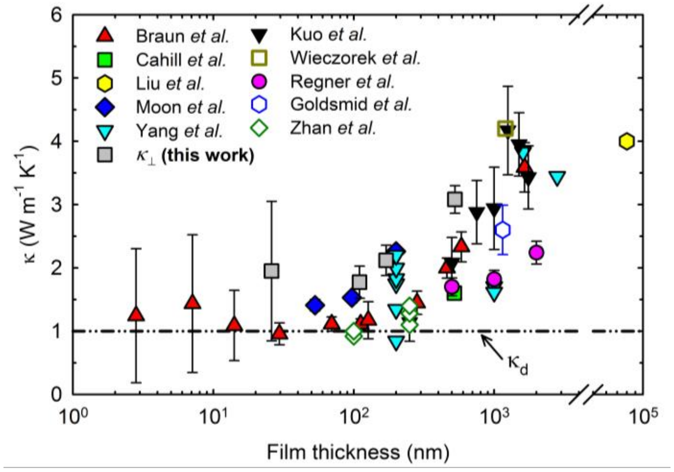

Figure 2.1: Prior $\kappa_\perp$ measurement results[14-22, 35] of a-Si films at 300 K**.** Our cross-plane data are shown as grey square boxes. Thermal conductivity of the diffusons (κ_d) (dash-dot-dot line) based on Allen-Feldman (AF) theory[25] is also shown as a reference.

In this work, in order to obtain intrinsic thermal conductivity value of a-Si nanostructures without the influence of contact resistance, we utilized novel structures and devices of a-Si nanotubes (NTs) and films that enabled precise in-plane thermal conductivity ($\kappa_{\parallel}$) measurements over a wide size range of 5 nm to 1.7 μm. The measured $\kappa_{\parallel}$ showed considerably higher values compared to $\kappa_{\perp}$: $\kappa_{\parallel}$ are ~1.5, ~3.0, and ~5.3 $W.m^{-1}K^{-1}$ for $t=$ ~5 nm, ~ 100 nm, and 1.7 μm, respectively. The size dependent $\kappa_{\parallel}$ data also suggests that propagons contribute significantly to κ of a-Si films even with thickness down to 5 nm, unlike the previously suggested lower bound of 100 nm. We also measured cross-plane thermal conductivity ($\kappa_{\perp}$) of films, and yielded results that were consistent with prior studies, but considerably lower than $\kappa_{\parallel}$. The anisotropic κ observed in the films further manifests the broad MFP spectra of propagon. With the measured size dependent κ along both directions, we extracted the MFP distribution of propagon using an algorithm developed by Minnich[36]. It is found that propagon MFP ranges from 10 nm to over 10 μm and those with MFP greater than 1 μm contributes to ~30 % of κ_p in 'bulk' a-Si at 300 K, which has a bulk value approaching ~5.5 $W.m^{-1}K^{-1}$ for $t > 2$ μm.

2.2 Preparation and Structural Analysis of a-Si Nanotubes and Films

The a-Si NTs were fabricated by depositing a-Si shells on Ge nanowires at 490 ^{o}C with four different nominal shell thicknesses of 5, 20, 40, and 100 nm, and then selectively etching the Ge cores[37]. Detailed geometry information of NTs can be found in Table 2.1.

Table 2.1: Geometry information of the NTs

Sample #	Shell thickness (nm)	Outer diameter (nm)	Length (μm)
1	96	219	9.72
2	36.6	137	6.06
3	38.7	125	13.3
4	39.5	136	10.3
5	20.9	150	9.29
6	19.3	109	10
7	21.2	101	9.88
8	5.6	81	10.5
9	5.1	88	5.67
10	5.2	46	6.23

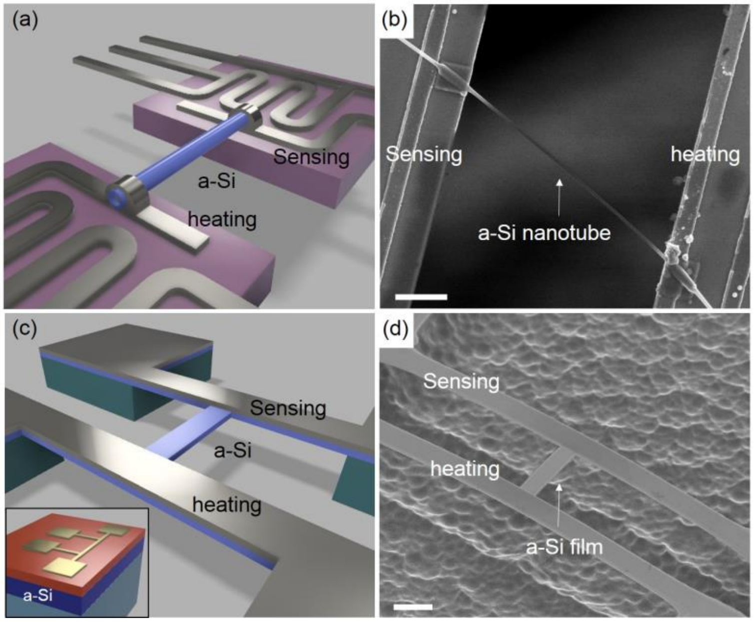

Figure 2.2: Thermal conductivity measurement schemes for in-plane and cross-plane configurations. (a) Schematic and (b) SEM image of in-plane a-Si NT device. (c) Schematics of either in-plane (main panel) or cross-plane 3ω (inset) a-Si film devices. (d) SEM image of suspended a-Si film supported by two Pt/Cr electrode bridges (marked as heating and sensing). Scale bars for (b) and (d) are 5 μm.

We prepared a-Si film samples of 26 nm to 1.7 μm for both $\kappa_{\parallel}$ and $\kappa_{\perp}$ measurements. First, we grew a-Si films on either Si or SiO_2/Si substrates using identical growth conditions as the a-Si NTs. After the film growth, devices were fabricated for suspended-beam in-plane (Figure 2.2c,d) and 3ω cross-plane κ measurements (inset in Figure 2.2c). To fabricate suspended a-Si film device for the in-plane thermal conductivity measurement, a-Si films with varying thickness were deposited using chemical vapor deposition (CVD) on p+ Si substrates covered with 100 nm thick thermal oxide. Using the same growth condition from a-Si NTs[37], only growth time was varied to change the target a-Si film thickness. On top of a-Si layer, metal electrodes and heating/sensing lines (10 nm Cr/70 nm Pt), as shown in Figure 2.2c,d, were fabricated via e-beam lithography (EBL), metal sputtering and lift off. Dimension of the sensing and heating lines are 60 μm in length and 3 μm in width. Across the heating and sensing electrodes, a-Si bridges of 3 μm wide and 10 μm long were patterned using EBL followed by dry etching (Oxford Plasmalab P100 RIE/ICP) of remaining a-Si and SiO_2 layers using SF_6 gas. After defining the a-Si bridges across the heating and sensing ribbons, the bridges were released by removing the underneath Si substrate using XeF_2 isotropic etching (Xactix XeF_2 Etcher). The devices were further treated by buffer oxide etchant (BOE) and acetone to remove the SiO_2 and e-beam resist layers attached on the suspended a-Si channel. Finally, the devices were dried using critical point dryer (Tousimis AutoSamdri 815A) to avoid possible damage effect by surface tension.

Table 2.2: Geometry information of the films

Sample #	Thickness (nm)	Width (μm)	Length (μm)
1	**26**	**2.6**	**9.2**
2	**170**	**2.5**	**9.45**
3	**525**	**2.8**	**9.8**
4	**1700**	**2.66**	**9.67**

In case of cross-plane κ measurement using the 3ω method, a-Si films were grown by identical CVD conditions on moderately p-doped Si substrate with resistivity of 1~10 Ω·cm. Also, reference devices without a-Si layer were prepared at the same time for all the following fabrication steps. On either a-Si layers or reference Si substrates, 60 nm thick Al_2O_3 layers were deposited using atomic layer deposition (Beneq TFS200) for electrical insulation. Finally, on top of Al_2O_3 layer, Cr/Au of 15/125 nm were patterned, as shown in Figure 2.7, by photolithography, sputtering, and lift off. Detailed geometry information is shown in Table 2.2.

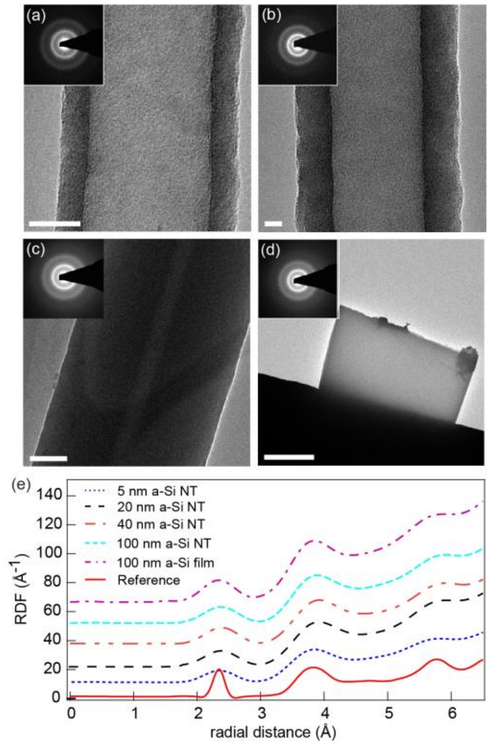

Figure 2.3: TEM images of (a) 5 nm thick a-Si NT, (b) 20 nm thick a-Si NT, (c) 100 nm thick a-Si NT, (d) 100 nm thick a-Si film, and (e) Radial distribution function (RDF) of the a-Si NTs and the 100 nm-thick a-Si film. The RDF of a reference a-Si film is from previous work by Laaziri *et al.*[38] The scale bars are 10 nm for (a) and (b), 50 nm for (c), and 5 µm for (d).

Radial distribution function (RDF) analysis (Figure 2.3e) from the SAED images further confirmed that our a-Si NTs and films have the same degree of atomic disorder as reference a-Si films which were fabricated through ion bombardment on crystalline Si[38].

2.3 Measurement Principles

We measured $\kappa_{\|}$ of the NTs using the suspended micro-device method[39, 40]. To calibrate our measurement, we measured an amorphous SiO_2 NT of similar geometry (shell thickness of 7.7 nm) and large amorphous SiO_2 nanowires (diameters of ~250 nm), and obtained results that match well with the established values of a-SiO_2 (Figure 2.4).

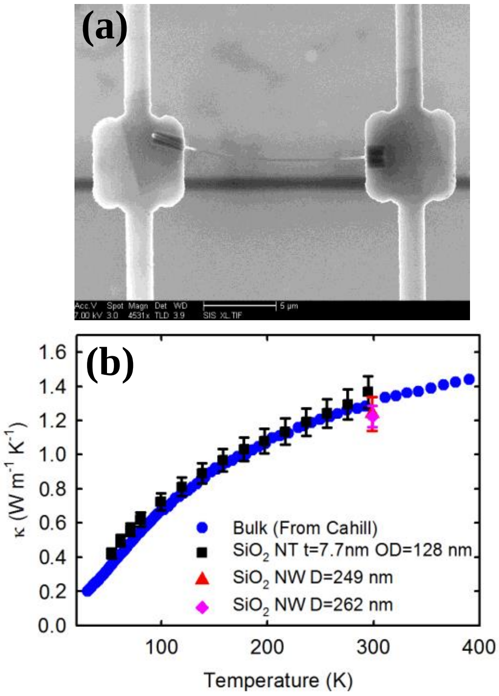

Figure 2.4: (a) SEM of an a-SiO_2 NT on a suspended device. (b) thermal conductivity vs. temperature of a-SiO_2 NT and nanowires (NWs). The SiO_2 NT (black square) and SiO_2 NWs (red triangle and pink diamond) were measured on the suspended devices shown in (a), using the same AC heating scheme as for the a-Si films. The measurement results agree well with the reference κ values of a-SiO_2 reported by Cahill[41].

The in-plane thermal conductivity of a-Si films was measured with the suspended device platform with modulated heating scheme developed by us (Zheng *et al.*[42]). Briefly, an AC current modulated at frequency f_h is applied on the heating beams. The Joule heat is dissipated partially through the heating beams to the substrate and partially through the a-Si thin-film bridge to the sensing beams, as shown in Figure 2.5a. It has been shown that the convection and radiation heat transfer effects are negligible compared to heat conduction along the beams and film sample. The heating and sensing beam temperature rises were detected using a high resolution resistive thermometry using the differential method[42].

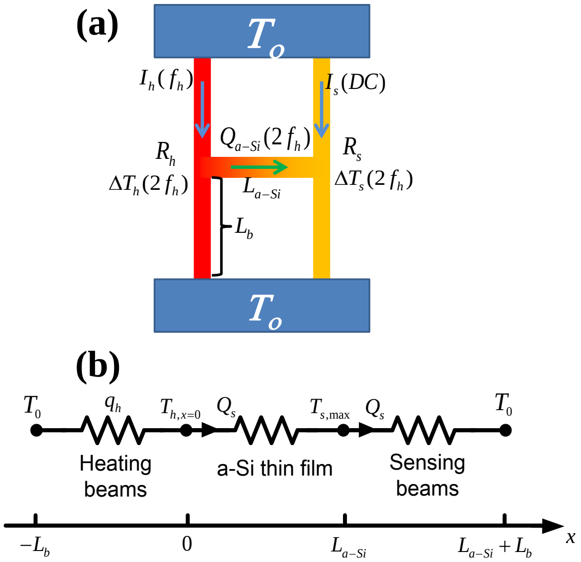

Figure 2.5: (a) Schematic diagram of the a-Si film device. (b) Corresponding thermal resistance circuit diagram.

Note that in the data analysis from our previous work[42], we assume that the heat transferred from the heating beam to the sensing beam is negligible compared to that through the heating beams. This assumption is only valid for samples with much smaller thermal conductance than the beams, such as nanowires and nanotubes. However, for the a-Si thin-film bridges studied here, thermal conductance of the samples is expected to be on the same order of magnitude as the beams. Therefore, a new analytical model has been developed to explicitly account for the heat conduction through the a-Si films. Figure 2.5b shows the thermal resistance circuit for the suspended device with a-Si film (see Figure 2.2c,d).

The heating side ($x = -L_b$ to $x = 0$ in Figure 2.5b) is heated up by Joule heating of metal films along the beams, and the steady state heat conduction equation can be written as,

$$-\kappa_{\mathrm{b}} \frac{\partial^2 \Delta T}{\partial x^2} = q_h, \tag{2.1}$$

where κ_{b} is the thermal conductivity of the beams, $\mathrm{q_h} = \frac{I_h^2 R_h}{2 L_b S_b}$, $\mathrm{I_h}$ is root-mean-squared (RMS) value of the applied modulated current, $\mathrm{R_h}$ is the heating beam resistance, $\mathrm{L_b}$ is the half beam length, $\mathrm{S_b}$ is the beam cross-section area.

The boundary conditions are:

$$\Delta \mathrm{T}(-\mathrm{L_b}) = T_0 - T_0 = 0, \tag{2.2}$$

$$-2\mathrm{S_b} \kappa_b \frac{\partial \Delta T}{\partial x}\bigg|_{x=0} = Q_s, \tag{2.3}$$

where Q_s is the heat conducted through the a-Si film and sensing beams.

Equation 2.1 can be solved and the heating beam temperature can be expressed as

$$\Delta \mathrm{T_h}(x) = -\frac{q_h}{2\kappa_b} x^2 - \frac{Q_s}{2 S_b \kappa_b} x + \frac{q_h}{2\kappa_b} L_b^2 - \frac{Q_s}{2 S_b \kappa_b} L_b. \tag{2.4}$$

Then we can get the average temperature along the heating beam,

$$\overline{\Delta T_h} = \frac{q_h}{3\kappa_b} L_b^2 - \frac{Q_s}{4S_b\kappa_b} L_b. \tag{2.5}$$

Similarly, solving the steady state heat conduction equation (without internal heating) for the sensing beam, we can get

$$\mathrm{Q_s} = 2\overline{\Delta T_s}\kappa_b \frac{2S}{L_b} = \frac{4\overline{\Delta T_s}S_b\kappa_b}{L_b}, \tag{2.6}$$

where $\overline{\Delta T_s}$ is the measured average temperature along the sensing beam.

The maximum temperature of the sensing beams is given as

$$\Delta T_{s,max} = 2\overline{\Delta T_s}\ . \tag{2.7}$$

Combining Eq. 2.5 and 2.6, we can obtain

$$\mathrm{Q_s} = \frac{4\overline{\Delta T_s}q_h S_b L_b}{3(\overline{\Delta T_h}+\overline{\Delta T_s})}, \tag{2.8}$$

and

$$\mathrm{\kappa_b} = \frac{q_h L_b^2}{3(\overline{\Delta T_h}+\overline{\Delta T_s})}\ , \tag{2.9}$$

where $\overline{\Delta T_h}$ and $\overline{\Delta T_s}$ are measured in the experiment.

From Eq. 2.4, at x=0, we can get

$$\Delta \mathrm{T_{h,x=0}} = \frac{q_h}{2\kappa_b} L_b^2 - \frac{Q_s}{2S_b\kappa_b} L_b. \tag{2.10}$$

Then the a-Si film thermal conductance and thermal conductivity can be expressed as

$$\mathrm{G_{a-Si}} = \frac{Q_s}{\Delta \mathrm{T_{h,x=0}} - \Delta \mathrm{T_{s,max}}} = \frac{4\overline{\Delta T_s}\mathrm{q_h} S_b L_b}{3(\overline{\Delta T_h} + \overline{\Delta T_s})(\Delta \mathrm{T_{h,x=0}} - \Delta \mathrm{T_{s,max}})}. \tag{2.11}$$

$$\kappa_{\mathrm{a-Si}} = \mathrm{G_{a-Si}} \frac{L_{a-Si}}{\mathrm{S_{a-Si}}} = \frac{4\overline{\Delta T_s}\mathrm{q_h} S_b L_b}{3(\overline{\Delta T_h} + \overline{\Delta T_s})(\Delta \mathrm{T_{h,x=0}} - \Delta \mathrm{T_{s,max}})} \frac{L_{a-Si}}{\mathrm{S_{a-Si}}}. \tag{2.12}$$

where L_{a-Si} and $\mathrm{S_{a-Si}}$ are length and cross-section area of the a-Si film, respectively.

Figure 2.6 shows the measured $\overline{\Delta T_h}$ and $\overline{\Delta T_s}$ as a function of input heating power for film with thickness of 525 nm at 300 K. After measuring $\overline{\Delta T_h}$ and $\overline{\Delta T_s}$, we can calculate the thermal conductivity of the a-Si film from Eq. 2.12.

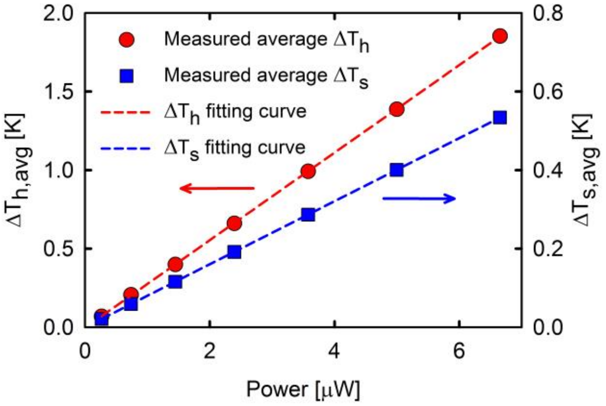

Figure 2.6: The measured $\overline{\Delta T_h}$ and $\overline{\Delta T_s}$ vs. input heating power for t=525nm a-Si film at 300 K.

The 3ω method[41] has been employed here to measure the cross-plane thermal conductivity of a-Si films. A metal strip was deposited by sputtering, functioning as both a heater for applying a periodic heat flux and a thermometer for measuring the surface temperature. A 60 nm thick Al_2O_3 thin film was deposited by atomic layer deposition (ALD) as an insulation layer, as shown in Figure 2.7a.

By applying an AC current I(ω) with angular modulation frequency ω through the metal line, the periodic heating will give rise to a heat flux oscillating at frequency 2ω, accompanying with the generated thermal wave diffusing into the specimen. The penetration depth is determined by the thermal diffusivity of the specimen and the frequency of the AC current. Because the resistance of the heater depends linearly on the temperature, the resistance will also oscillate at frequency 2ω. The voltage drop across the heater thus contains a third harmonic component ($V_{3\omega}$) that depends on the AC temperature rise ($\Delta T_{2\omega}$) of the heater, expressed as[41],

$$V_{3\omega} = \frac{I_0}{2}\frac{dR}{dT}\Delta T_{2\omega}\sin(3\omega t + \phi). \tag{2.13}$$

In our experiments, the 3ω measurement setup has been calibrated with standard samples, namely Si substrate covered with Al_2O_3, which also works as the reference here to extract the thermal conductivity of amorphous Si. The reference sample was firstly measured to obtain the thermal conductivity of the Si substrate (120 $W.m^{-1}.K^{-1}$) by the slope method,

$$\kappa_{\mathrm{Si,sub}} = -\frac{P}{2\pi L}\left(\frac{d(\Delta T_{ref})}{d(\ln(2\omega))}\right)^{-1}, \tag{2.14}$$

where $\frac{d(\Delta T_{ref})}{d(\ln(2\omega))}$ is the slope of the reference sample temperature rise (ΔT_{ref}) versus frequency (red triangle in Figure 2.7c). Then the thermal conductivity of Al_2O_3 insulation layer (1.02 $W.m^{-1}.K^{-1}$) was obtained by fitting the ΔT_{ref} to that calculated in the 2D heat conduction model (red solid line) in Figure 2.7c. This calibrated thermal conductivity of Al_2O_3 layer agrees well with the value reported in reference, which varies from 0.95 $W.m^{-1}.K^{-1}$ to 1.4 $W.m^{-1}.K^{-1}$ at room temperature.

Then we measured the temperature rise of the a-Si sample (Si substrate with a-Si layer, also covered with an Al_2O_3 coating, see Figure 2.7b), ΔT_{aSi}, as shown in Figure 2.7c (blue square), based on which the 'apparent' thermal conductivity can be determined as:

$$\kappa_a = q''t/(\Delta T_{aSi} - \Delta T_{ref}) \,, \tag{2.15}$$

where q'' is the heat flux applied onto the 3ω heater (in [W/m^2]), and t is the thickness of the a-Si film. For the a-Si sample shown in Figure 2.7b (thickness = 110 nm), the measured apparent cross-plane thermal conductivity κ_a is 1.48 ±0.13 W.m^{-1}.K^{-1}. Note that this apparent thermal conductivity includes the effect of the contact resistance (R_c) between the a-Si layer and the Si substrate, and needs to be corrected, especially for thin films (see the next section).

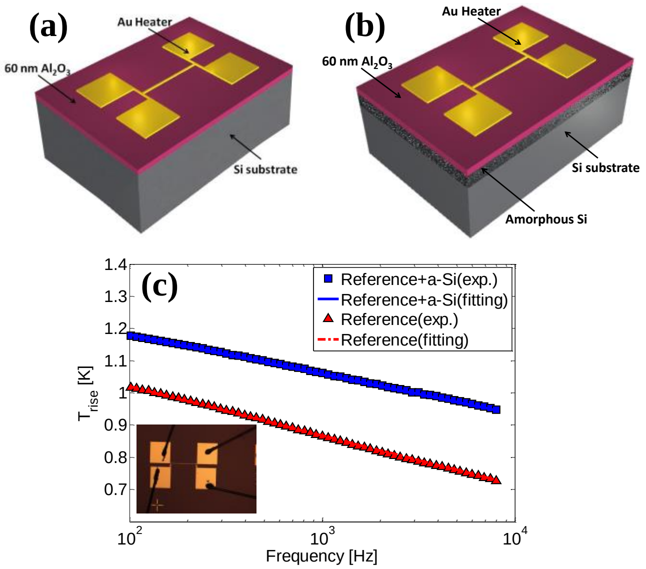

Figure 2.7. (a) Schematic diagram of the reference sample: Si substrate covered with 60 nm thick Al_2O_3, for the 3ω measurement calibration. (b) Schematic diagram of a device with a-Si film on top of Si substrate for the 3ω measurement. (b) Measured temperature rises on the reference sample (Si substrates without a-Si film) and the sample with the 110 nm thick a-Si film. The solid lines are the fitting results with a two-dimensional heat conduction model following Borca-Tasciuc *et al.*'s work[43]. Inset is the top view of the 3ω device.

2.4 Size Dependent Thermal Conductivity

Figure 2.8 shows the measured room temperature $\kappa_{\parallel}$ of a-Si NTs and films as a function of shell or film thickness (t). For NTs, we showed that no correlation between $\kappa_{\parallel}$ and sample length or outer diameter was observed (Figure S2), suggesting negligible thermal contact resistance between the NTs and the suspended devices and the similarity between the NTs and films with t being the characteristic size. It can be seen that $\kappa_{\parallel}$ shows strong size dependence, and increases with t from 5 nm to 1.7 μm. As discussed before, size dependence was not observed in sub-100 nm a-Si films in prior cross-plane measurements[14, 21]. However, our results showed that $\kappa_{\parallel}$ start increasing for $t \geq 5$ nm, revealing the important role that propagon plays in thermal transport in a-Si even down to 5 nm thickness. From the size dependent data at 300 K, we can also see that κ will saturate to ~5.5 $W.m^{-1}K^{-1}$ when the thickness is larger than 2 μm (inset of Figure 2.8). This 'bulk' value is much larger than what was expected for amorphous solids (~1 $W.m^{-1}K^{-1}$). Note that there is no true "bulk" a-Si with quasi-infinite three-dimensional size, because crystallization is very difficult to avoid for very large sample size. The "bulk" κ here is the saturation value extrapolated from our thickness dependent measurements, as well as from the phenomenological model. This 'bulk' value is consistent with previous studies on thicker a-Si films (> 1.6 μm).

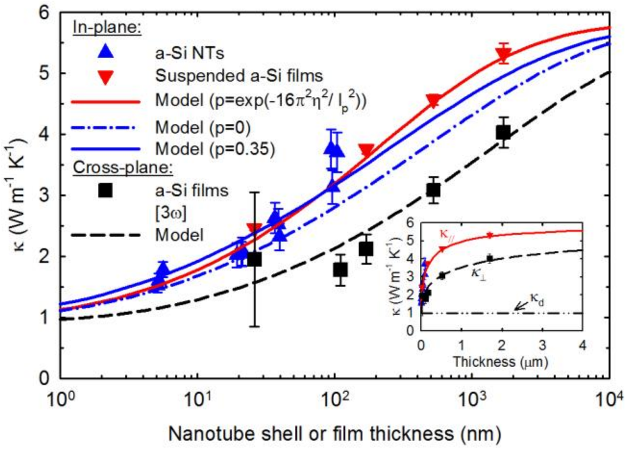

Figure 2.8: Thermal conductivity (κ) of the a-Si NTs (blue triangle up) and a-Si films for in-plane (red triangle down) and cross-plane (black square). The cross-plane data have been corrected after subtracting the contact resistance. The cross-plane 26 nm film shows large error bar mainly due the uncertainty of the contact resistance. Model based on *Landauer* approach[44] is used to calculate the thickness dependent thermal conductivity behavior of thin films. The model with specularity parameter p=0 (blue dash-dot line) gives poor fitting with our in-plane thin film and NTs data, while the model with frequency dependent 'p' by Ziman's formula (roughness η=0.60 nm) (red solid line) shows excellent agreement with the in-plane data. We also plot the model based on effective constant 'p=0.35' (blue solid line) for comparison. The inset shows the same data with linear scale on the x-axis. κ is saturating to ~5.5 W/m-K when thickness is larger than 2 μm. Thermal conductivity of the diffusons (κ_d) (dash-dot-dot line) based on Allen-Feldman (AF) theory[25, 28] is also shown in the inset as a reference.

Figure 2.8 also shows the thickness dependence of $\kappa_\perp$ at 300 K, which has been corrected after subtracting the contact resistance R_c. Lee and Cahill[45] showed that the measured apparent thermal resistance ($R_a = t/\kappa_a$) by the 3ω method can be considered as the sum of intrinsic film resistance ($R_f = t/\kappa_f$) and contact resistance (R_d), *i.e.*,

$$\frac{\mathrm{t}}{\kappa_\mathrm{a}} = \frac{t}{\kappa_\mathrm{f}} + R_c, \tag{2.16}$$

where *t* is the film thickness. Therefore, the intrinsic film thermal conductivity is given as

$$\kappa_\mathrm{f} = \frac{\kappa_\mathrm{a}}{1-\frac{R_c\kappa_\mathrm{a}}{t}}\,. \tag{2.17}$$

Table 2.3: 3ω measurement results before and after subtracting R_c

($R_{c,lower}$=0.5×10^{-8} K. m^2/W, $R_{c,upper}$=2×10^{-8} K. m^2/W).

Thickness (nm)	1700	525	170	110	26
Apparent κ_a (W.m^{-1}.K^{-1})	3.92	2.88	1.84	1.48	0.93
Intrinsic κ_f after subtracting $R_{c,lower}$ (W.m^{-1}.K^{-1})	3.97	2.96	1.95	1.59	1.13
Intrinsic κ_f after subtracting $R_{c,upper}$ (W.m^{-1}.K^{-1})	4.11	3.23	2.35	2.02	3.26
Average intrinsic κ_f (W.m^{-1}.K^{-1})	4.03	3.08	2.12	1.77	1.95

We employed R_c in the range of $0.5 - 2.0 \times 10^{-8}\ K.m^2/W$ to our 3ω samples, which is within the typical range of R_c for solid-solid interface[45], and calculated the κ_f for samples with different thicknesses based on Eq. (2.17) (see Table 2.3). Figure 2.8 shows the average intrinsic κ_f after subtracting R_c, and the error bars include the uncertainties both from the $\Delta T_{2\omega}$ measurement and of the contact resistance. Note that the normalized cross-plane data in Figure 2.12a is after subtracting $R_c = 2 \times 10^{-8}$ K. m^2/W. In the MFP distribution reconstruction procedure, we tried different values for the specularity parameter p for the in-plane data and various 'R_c' values for the cross-plane data, and found that the in-plane and cross-plane reconstructed MFP distribution shows excellent agreement with p=0.35 and $R_c = 2 \times 10^{-8}$ K. m^2/W.

As mentioned earlier, the 3ω method used here can only measure the sum of the intrinsic thermal resistance of the films and R_c, which is difficult to separate due to the quasi-ballistic nature of propagon transport across the films and the uncertainty involving in determining R_c. Therefore, the $\kappa_\perp$ reported here should only be considered as an effective value and has a larger uncertainty compared to the $\kappa_{\parallel}$ data, especially for smaller t. The measured $\kappa_{\perp}$ of the Si films are similar to prior $\kappa_{\perp}$ data (Table 2.3 and Figure 2.1), namely, only increase for $t \geq 100$ nm, but lower than $\kappa_{\parallel}$ measured from the films fabricated from the same batches. The observed anisotropy of thermal transport in a-Si films further suggests that the propagon MFP is comparable to film thickness investigated here, similar to the case of crystalline Si films[46, 47].

2.5 Temperature Dependent $\kappa_{\parallel}$ of a-Si Nanotubes and Films

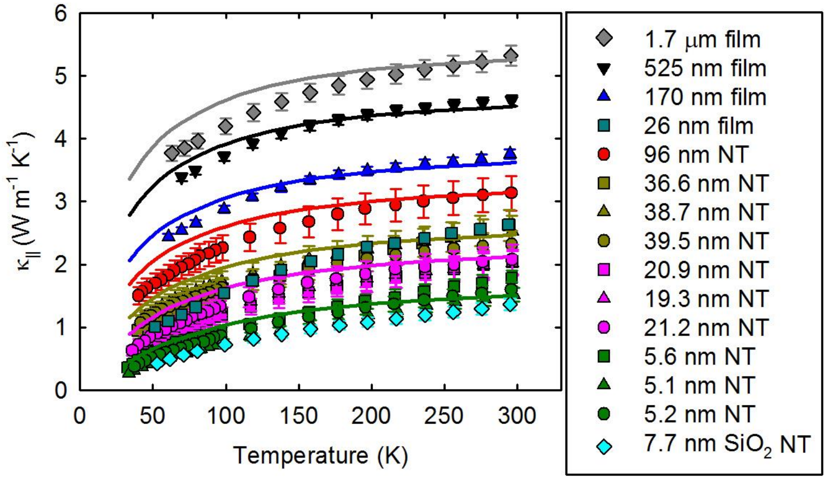

Figure 2.9: Temperature dependent $\kappa_{\parallel}$ for a-Si film and NT samples. Films with thickness of 1.7 μm (gray diamond), 525 nm (black triangle down), 170 nm (blue triangle up) and 26 nm (dark cyan square) show similar trend of temperature dependence as the NTs with thickness of 96 nm (red circle), ~40 nm (dark yellow symbols), ~20 nm (pink symbols) and ~5 nm (dark green symbols). Our model shows excellent agreement with the experimental data for all the samples down to 150 K. At T<150 K, the fitting slightly deviates from the experiment, suggesting the scattering strength for propagons may be underestimated at low temperature. A SiO_2 NT with shell thickness of 7.7 nm (cyan diamond) was measured for calibration.

Figure 2.9 shows the temperature dependent $\kappa_{\parallel}$ of a-Si films and NTs from 40K to 300K, along with the 7.7 nm SiO_2 NT. The films (t=1.7 μm, 525 nm, 170 nm, and 26 nm) and NTs (t = ~100, ~40, ~20 and ~5 nm) show similar trend in the temperature dependence. Notably, the ~5 nm a-Si NTs show similar κ as that of the SiO_2, which is known to possess negligible propagon contribution[28], indicating a similar behavior in a-Si when the size is approaching 5 nm.

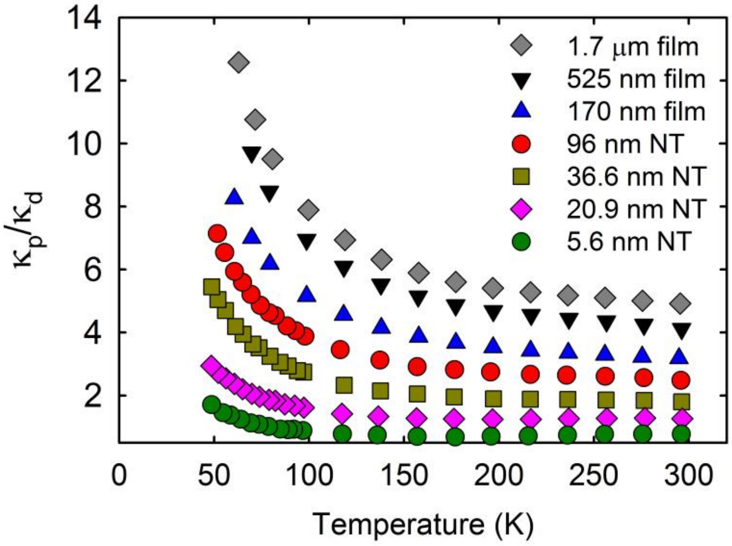

Figure 2.10: Ratio of propagon thermal conductivity (κ_p) to diffuson thermal conductivity (κ_d) as a function of temperature for samples with thickness from 1.7 μm to 5.6 nm.

Furthermore, $\kappa_{\parallel}$ decreases with lower temperature, and by subtracting the diffuson contribution obtained from previous numerical model by Allen *et al.*[25], we can show that propagon contribution is relatively more pronounced at lower temperature (Figure 2.10). For example, for t=1.7 μm film, the ratio of κ_p/κ_d increases from 4.9 at 300 K to 10.8 at 70 K. At 300 K, the ratio for t=1.7 μm, 525 nm, 170 nm, 96 nm, 36.6 nm, and 20.9 nm samples are larger than ‘1’, but t=5.6 nm NT sample is about 0.8, which is due to the stronger boundary scattering for propagons at this length scale.

2.6 Mean Free Path Distribution of Propagon in a-Si

The size and temperature dependence of κ in a-Si NTs and films can be utilized to quantify the cumulative MFP distribution of propagons, $F(\Lambda_\mathrm{p})$, at different temperatures. The cumulative MFP distribution for both directions ($F_\parallel(\Lambda_\mathrm{p})$ and $F_\perp(\Lambda_\mathrm{p})$), as shown in Figure 2.12a, are reconstructed based on the normalized size dependent κ_p (*i.e.*, $\kappa_\mathrm{p}/\kappa_\mathrm{p,bulk}$) for both in-plane and cross-plane at 300 K.

We followed the method proposed by Minnich[36] to reconstruct mean free path distribution from the measured size dependent $\kappa_\parallel$ and $\kappa_\perp$. For both $\kappa_\parallel$ and $\kappa_\perp$, the propagon contribution κ_p is obtained by subtracting the diffuson contribution κ_d[25] from the measured total κ, *i.e.*, $\kappa_\mathrm{p} = \kappa - \kappa_d$. Then κ_p is related to the propagon MFP (Λ_p)[36, 48] via,

$$\kappa_\mathrm{p} = \kappa_\mathrm{p,bulk} \int_0^\infty S\left(\frac{\Lambda_\mathrm{p}}{t}\right) f(\Lambda_\mathrm{p}) d\Lambda_\mathrm{p}, \tag{2.18}$$

where t is the film thickness, $\kappa_\mathrm{p,bulk}$ is κ_p of bulk a-Si, $f(\Lambda_\mathrm{p})$ is differential MFP distribution, and is related to $F(\Lambda_\mathrm{p})$ through $F(\Lambda_\mathrm{p}) = \int_0^{\Lambda_\mathrm{p}} f(x)dx$; $\mathrm{S}\left(\frac{\Lambda_\mathrm{p}}{t}\right)$ is the heat flux suppression function, representing the suppression effect on propagon MFP in thin films relative to bulk a-Si. Using integration by parts on Eq. (2.18), we can obtain[36, 49]

$$\kappa_\mathrm{p} = \kappa_\mathrm{p,bulk} \int_0^\infty t^{-1} H\left(\frac{\Lambda_\mathrm{p}}{t}\right) F(\Lambda_\mathrm{p}) d\Lambda_\mathrm{p}, \tag{2.19}$$

where the kernel $H\left(\frac{\Lambda_\mathrm{p}}{t}\right)$ is defined as $H\left(\frac{\Lambda_\mathrm{p}}{t}\right) = -\mathrm{dS}/\mathrm{d}\left(\frac{\Lambda_\mathrm{p}}{t}\right)$. With the measured κ_p for a-Si NTs and films with different thickness t we can reconstruct the smooth cumulative MFP distribution $F(\Lambda_\mathrm{p})$ from Eq. (2.19) using an algorithm proposed by Minnich[36] based on convex optimization. The suppression function $\mathrm{S}\left(\frac{\Lambda_\mathrm{p}}{t}\right)$ of films along the in-plane[48] and cross-plane[50] directions are given as

$$\mathrm{S}_\parallel\left(\frac{\Lambda_\mathrm{p}}{t}\right) = 1 - \frac{3(1-\mathrm{p})}{2}\frac{\Lambda_\mathrm{p}}{t}\int_0^1 (u-u^3)\,\frac{1-\exp(-\frac{t}{u\Lambda_\mathrm{p}})}{1-p\cdot\exp(-\frac{t}{u\Lambda_\mathrm{p}})}\,\mathrm{d}u, \tag{2.20}$$

$$\mathrm{S}_\perp\left(\frac{\Lambda_\mathrm{p}}{t}\right) = 1 - \frac{\Lambda_\mathrm{p}}{t}\left(1-\exp\left(-\frac{t}{\Lambda_p}\right)\right), \tag{2.21}$$

where p in Eq. (2.20) is the specularity parameter for boundary scattering, which can range from 0 (fully diffusive) to 1 (fully specular). While p depends on frequency and hence MFP, here we employed a single p value in order to reconstruct $F_\parallel(\Lambda_\mathrm{p})$. As we shall see later in the thermal conductivity model, this p value represents an effective one for all the propagon modes when frequency dependent p is taken into account.

Since there should be only one MFP distribution function for bulk a-Si, we varied p and R_c values, and found that $F_\parallel(\Lambda_\mathrm{p})$ and $F_\perp(\Lambda_\mathrm{p})$ shows excellent agreement with p=0.35 and $R_\mathrm{c} = 2\times10^{-8}\ \mathrm{m}^2.\mathrm{K}.\mathrm{W}^{-1}$. Note that the normalized cross-plane data we used to reconstruct $F_\perp(\Lambda_\mathrm{p})$ is after subtracting $\mathrm{R_c} = 2\times10^{-8}\ \mathrm{m}^2.\mathrm{K}.\mathrm{W}^{-1}$, and we do not include the 26 nm film due to the large uncertainty (Table S1). The value of $\mathrm{R_c} = 2\times10^{-8}\ \mathrm{m}^2.\mathrm{K}.\mathrm{W}^{-1}$ is consistent with previous study for Si-SiO$_2$ interface by Lee and Cahill[33]. The best fitting with p=0.35, instead of p=0, indicates that propagon scattering is partially specular at surface of our a-Si NT and thin film samples. This is not surprising given the fact that the typical wavelength of propagons in a-Si (>2 nm[28]) is much larger than the surface roughness of the a-Si NT (root mean square (rms)=0.815±0.04 nm), as determined from TEM imaging (Figure 2.11).

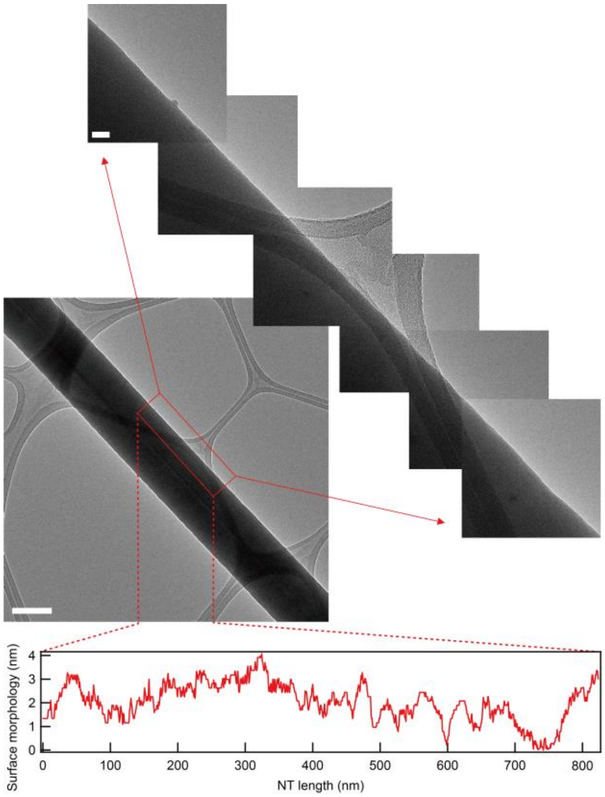

Figure 2.11: Surface roughness analysis on a-Si NTs with 100 nm shell thickness, by stitching a series of zoomed-in TEM images together. The RMS of the roughness is determined to be 0.815±0.04 nm. Scale bar, 200 nm for low magnification image (bottom) and 20 nm for the zoomed-in images. Bottom panel shows roughness profile along the NT surface inside the zoom-in region with exaggerated scale of y-axis to better visualize the roughness.

The extracted MFP spectra show that propagons with MFP down to 10 nm start contributing to κ at 300 K, which is much lower than the lower bound of MFP spectra (>100 nm) suggested by previous experimental studies[14, 21], but is consistent with the recent MD and theoretical predictions[27, 28]. In addition, instead of being saturated at 1 μm[21], we found that propagons with MFP greater than 1 μm contribute to ~30% of $\kappa_{\mathrm{p,bulk}}$. The role of these long MFP propagons might have been underestimated previously in both experiments[21] (due to the interfacial effect in $k_\perp$ measurements) and simulations[26, 28] (caused by the limited supercell size). The MFP distribution is surprisingly similar to that of phonon in crystalline Si [21, 51, 52]. This underscores the long range correlation in the amorphous structure [28].

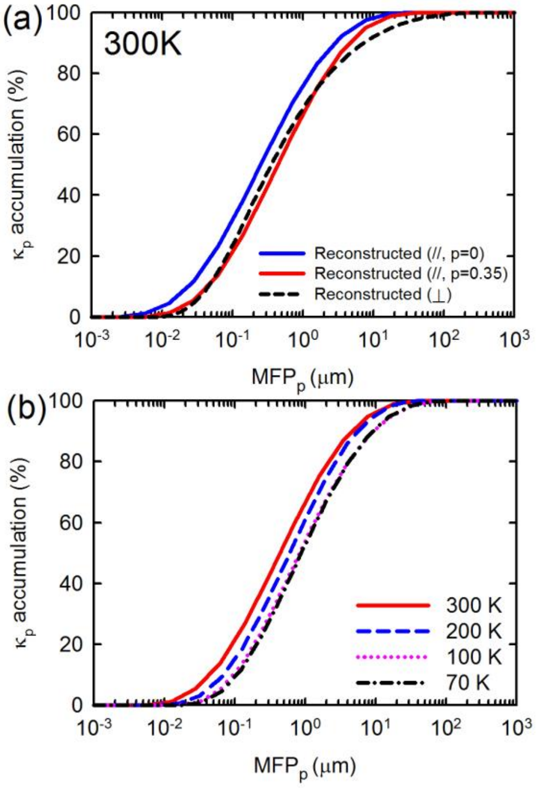

Figure 2.12: (a) Reconstructed propagon MFP distribution at 300K. With specularity parameter p=0.35 (red solid line), instead of p=0 (blue solid line), the MFP distribution reconstructed from $\kappa_{\parallel}$ agrees well with that from $k_\perp$ (black dash line), suggesting partial specular scattering. The MFP spectra range from 10 nm to 10 μm at 300 K. (b) Reconstructed propagon MFP distributions based on $\kappa_{\parallel}$ from 300 K to 70 K. The contribution to κ_{p} from propagons with MFP greater than 1 μm increases from 30% at 300 K to 50% at 70 K.

From the temperature dependent $\kappa_{\parallel}$ shown in Figure 2.9, we also reconstructed the $F_{\parallel}(\Lambda_{\mathrm{p}})$ at different temperatures, as shown in Figure 2.12b. The $F_{\parallel}(\Lambda_{\mathrm{p}})$ is shifting slightly towards longer MFP with decreasing temperature. The propagon MFP range at 70 K is from 40 nm to 20 μm, longer than that of 10 nm to 10 μm at 300 K. The contribution to $\kappa_{\mathrm{p,bulk}}$ from propagons with MFP greater than 1 μm increases from ~30% at 300 K to ~50% at 70 K. It should be noted that here we assumed p=0.35 from 300 K to 70 K. However, at lower temperature, propagons with longer wavelength, which are more likely to exhibit specular boundary scattering, are more dominant. Accordingly, the overall p would be higher at lower temperature. Therefore, the extracted propagon MFP shown in Figure 2.12b could represent the lower bound for T < 300 K.

2.7 Scattering Mechanisms of Propagons in a-Si

We used a phenomological model based on the *Landauer* formalism to understand the scattering mechanism of propagon and its MFP distribution.

For both in-plane and cross-plane directions, the overall κ includes the contribution from propagon and diffuson, *i.e.*, $\kappa = \kappa_{\mathrm{p}} + \kappa_d$. κ_d is obtained from previous work by Allen *et al.*[25] κ_{p} can be modeled based on the *Landauer* approach, namely[44]

$$\kappa_{\mathrm{p}} = \left(\frac{\mathrm{k_B^2 T \pi^2}}{\mathrm{3h}}\right) \int_0^{\omega_{c,j}} \left(\frac{M_p}{A}\right) \left(T_p L\right) W_p d(\hbar\omega), \tag{2.22}$$

where k_{B}, h, T, A, L are Boltzmann constant, Planck's constant, temperature, sample cross-section area, and length, respectively; $\omega_{c,j}$ is the cut-off frequency between propagons and diffusons for the j^{th} mode (transverse acoustic (TA) and longitudinal acoustic (LA) modes); M_p is the number of conducting channels at $\hbar\omega$; W_p is the "window" function defined as $W_\mathrm{p} = \frac{3}{\pi^2}\left(\frac{\hbar\omega}{k_B T}\right)^2\left(-\frac{\partial n_0}{\partial(\hbar\omega)}\right)$, where $\mathrm{n}_0(\omega)$ is Bose-Einstein distribution; and T_p is the transmission function at $\hbar\omega$. It has been shown that the *Landauer* approach is equivalent to that based on the Boltzmann Transport Equations, but provides a convenient approach to model both diffusive and ballistic transport and along different directions[44].

For propagons with a linear dispersion, $\omega = v_p q$, number of conducting channels (M_pr) and transmission (T_p) are given as[44, 53]

$$\frac{\mathrm{M}_\mathrm{p}(\hbar\omega)}{A} = \frac{(\hbar\omega)^2}{4\pi(\hbar v_p)^2} \text{ (for single mode in 3D case),} \tag{2.23}$$

$$T_p = \frac{\lambda_p(\omega)}{\lambda_p(\omega)+l} \quad , \tag{2.24}$$

where, v_p is the propagon group velocity, l being the sample length (L for in-plane and thickness t for cross-plane), λ_p is backscattering MPF, which can be related to conventional MFP $\Lambda_\mathrm{p}(\omega)$ as $\lambda_\mathrm{p}(\omega) = \frac{4}{3}\Lambda_p(\omega)$, and expressed in terms of group velocity v_p and frequency-dependent mode lifetime τ_p, *i.e.*

$$\lambda_\mathrm{p}(\omega) = \frac{4}{3}v_p(\omega)\tau_p(\omega) \ . \tag{2.25}$$

In Eq. (2.22), the only unknown parameter is the propagons MFP λ_p. Linear dispersion is applied for low frequency propagating modes[54], including TA and LA modes. The group velocity v_p of TA and LA modes are estimated using the elastic moduli for a-Si, *i.e.*, $v_{p,TA} = 3670\ m/s$ and $v_{p,LA} = 7640\ m/s$. The diffusivity of propagons is modeled by considering harmonic Rayleigh-type scattering ($\mathrm{D}_\mathrm{R}^{-1} = 3A\omega^4/v_p^2$)[18, 26, 54], anharmonic *Umklapp* scattering ($\mathrm{D}_\mathrm{U}^{-1} = 3BT\omega^2\exp(-C/T)/v_p^2$)[14, 25, 54], and anharmonic "two level system" (TLS) scattering ($\mathrm{D}_\mathrm{T}^{-1} = \frac{D\hbar\omega}{k_B}\tanh\left(\frac{\hbar\omega}{2k_BT}\right) + \frac{D}{2}\frac{ET^3}{1+Ek_BT^3/\hbar\omega}$)[26, 55, 56], where '$A$', '$B$', '$C$', '$D$', and '$E$' are adjustable parameters. Therefore, the propagon diffusivity and lifetime can be expressed as

$$\mathrm{D}_\mathrm{p}^{-1} = \mathrm{D}_\mathrm{R}^{-1} + \mathrm{D}_\mathrm{U}^{-1} + \mathrm{D}_\mathrm{T}^{-1}, \tag{2.26}$$

$$\tau_\mathrm{p} = \frac{3D_p}{v_p^2} = \frac{3}{v_p^2}\left(\mathrm{D}_\mathrm{R}^{-1} + \mathrm{D}_\mathrm{U}^{-1} + \mathrm{D}_\mathrm{T}^{-1}\right)^{-1}. \tag{2.27}$$

Substituting Eq. (2.23)-(2.27) in to Eq. (2.22), the thermal conductivity of the bulk a-Si can be obtained.

For a-Si thin films and nanotubes, boundary scattering significantly influences the MFP of propagons. For the cross-plane thermal conductivity, Eq. (2.24) is expressed as $T_p = \frac{\lambda_p(\omega)}{\lambda_p(\omega)+t}$, where t is the film thickness. For the in-plane thermal conductivity, T_pL can be reduced as $T_pL = \frac{\lambda_p(\omega)L}{\lambda_p(\omega)+L} \approx \lambda_p(\omega)$, because the sample length (L) parallel to the film direction is much larger than λ_p in our case. Additionally, for partially diffuse and partially specular boundaries, the in-plane backscattering MFP for films can be calculated from[57, 58]

$$\lambda_\mathrm{p,thin}(\omega) = \lambda_\mathrm{p,bulk}(\omega)\left[1 - \frac{3(1-p)}{2\delta}\int_0^1 (u-u^3) \times \frac{1-\exp(-\delta/u)}{1-p\exp(-\delta/u)}\,du\right], \tag{2.28}$$

where $\delta = \frac{4}{3}\frac{t}{\lambda_{p,bulk}}$, $\lambda_{p,bulk}(\omega)$ is the bulk backscattering MFP, t is the a-Si film thickness, and p is the specularity parameter, given by Ziman formula[59, 60]

$$p = \exp\left(-\frac{16\pi^2\eta^2}{l_p^2}\right), \tag{2.29}$$

where η is the characteristic dimension of the surface roughness, and l_p is the wavelength of the propagons.

The modeled in-plan and cross-plane results were fit to the room-temperature size-dependent data along both directions, as well as the temperature dependent in-plane data, by adjusting the fitting parameters: *A, B, C, D, E,* and η. The cross-plane data ($\kappa_\perp$) from the 26-nm thick film were not used for the fitting due to the large uncertainty. The corresponding cut-off frequency $\omega_{\mathrm{c,TA}}$ for TA and $\omega_{\mathrm{c,LA}}$ for LA modes were determined by examining the smooth cross-over of diffusivity for propagon ($\mathrm{D_p}$ in Eq. (2.26)) to diffuson, which is approximately 1-5 $\mathrm{mm^2/s}$[28]. The modeling results, along with the experimental data, are shown in Figure 2.8 for room temperature in-plane and cross-plane data, and in Figure 2.9 for temperature dependent in-plane data. The best fitting parameters are found to be: $\mathrm{A} = 9.1 \times 10^{-42}\ \mathrm{s^3.rads^{-4}}$, $\mathrm{B} = 4.2 \times 10^{-20}\ \mathrm{s.rads^{-2}.K^{-1}}$, $\mathrm{C} = 175$ K, $\mathrm{D} = 16.67\ \mathrm{s.m^{-2}K^{-1}}$, $\mathrm{E} = 4.4 \times 10^{-3}\ \mathrm{K^{-2}}$, and η = 0.60 nm. The modeling results show good fitting with *all* the experimental data (again, $\kappa_\perp$from the 26-nm thick film was not used for the fitting due to the large uncertainty). Below 150 K, the model shows slightly higher values compared to the experiment. This indicates that the model for κ_p may underestimate the scattering strength for propagons at low temperature, or ω_c could be different at lower temperature.

The cut-off frequency (transitioning from propagon to diffuson) of the TA and LA modes, which are not fitting parameters, are determined to be 1.76×10^{13} rads.s^{-1} and 3.20×10^{13} rads.s^{-1}, respectively. The corresponding diffusivity at ω_c are 5.1 mm^2.s^{-1} and 2.0 mm^2. s^{-1}, as shown in Figure 2.13, which are consistent with the average diffuson diffusivity at ω_c by Larkin and McGaughey, 8.9 mm^2.s^{-1} for ω^{-2} scaling and 1.7 mm^2.s^{-1} for ω^{-4} scaling[28]. The propagon diffusivity in our model, however, is larger than the results obtained from the MD simulation[28], which is reasonable because the limited supercell size in MD could have imposed an additional constraint on propagon MFP.

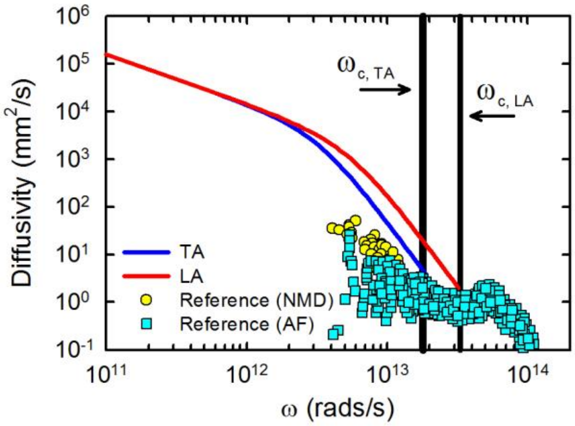

Figure 2.13: Propagon diffusivity as a function of frequency for TA (blue solid line) and LA (red solid line) modes at 300 K. The cut-off frequency for TA and LA modes are 1.76×10^{13} rads/s and 3.20×10^{13} rads/s, respectively. It shows smooth transition from propagon to diffuson diffusivity (cyan square)[28]. Our propagon diffusivity is remarkably higher than molecular-dynamics-based simulation (NMD) by Larkin *et al.*[28] (yellow circle). This may be because the NMD method is limited by the simulation cell size and cannot accurately predict the contribution from the long MFP propagons.

It is also necessary to comment on the role of the TLS scattering. If the model neglects the TLS scattering term, and only considers Rayleigh-type scattering and

Umklapp scattering, the integral of Eq. (2.22) will give increasing thermal conductivity at low temperature, as shown in Figure 2.14. This is because the *Umklapp* scattering will be exceedingly weak with decreasing temperature, resulting in higher κ. This implies the importance to introduce additional anharmonic scattering terms. TLS scattering, which is demonstrated by Liu *et al.*[61, 62] to exist and play an important role in a-Si, was then included in the scattering mechanisms in our model, in addition to the Rayleigh-type scattering and *Umklapp* scattering.

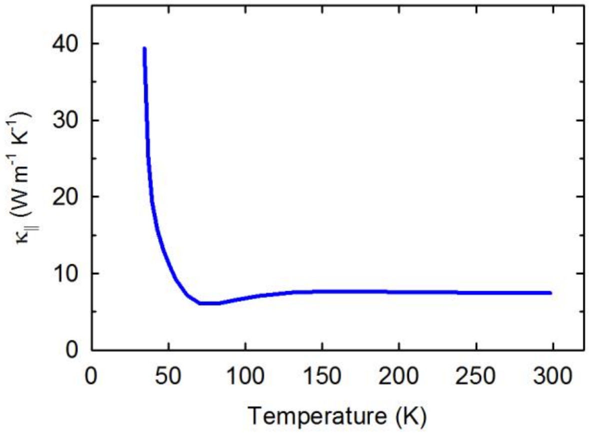

Figure 2.14: Temperature dependent thermal conductivity calculated from the model with only Rayleigh-type scattering and *Umklapp* scattering for film with thickness of 525 nm, *i.e.*, without the TLS scattering.

The size dependent modeling results are shown in Figure 2.8, along with the experimental data. The modeled in-plane and cross-plane results were fit to the room-temperature size-dependent data along both directions, by using *the same set* of the fitting parameters: *A, B, C, D, E,* and η, which are adjustable parameters in the scattering terms. The cross-plane data ($\kappa_\perp$) from the 26-nm thick film were not used for the fitting due to the large uncertainty. The corresponding cut-off frequency $\omega_{c,TA}$ for TA and $\omega_{c,LA}$ for LA modes were determined by examining the smooth cross-over of diffusivity for propagon to diffuson (Figure 2.13). The best fitting parameters were found to be: $\mathrm{A} = 9.1 \times 10^{-42}\ \mathrm{s^3.rads^{-4}}$, $\mathrm{B} = 4.2 \times 10^{-20}\ \mathrm{s.rads^{-2}.K^{-1}}$, $\mathrm{C} = 175\ \mathrm{K}$, $\mathrm{D} = 16.67\ \mathrm{s.m^{-2}K^{-1}}$, $\mathrm{E} = 4.4 \times 10^{-3}\ \mathrm{K^{-2}}$, and $\eta = 0.60$ nm. The modeling results show good fitting with *all* the experimental data (again, $\kappa_{\perp}$from the 26-nm thick film was not used for the fitting due to the large uncertainty).

For in-plane film modeling result shown in Figure 2.8, we found that $p = 0$ (fully diffusive boundary scattering) would not fit the $\kappa_{\parallel}$ data, which is consistent with the conclusion from the MFP reconstruction process (*i.e.*, $\mathrm{p} = 0.35$). Instead, using the 'p' calculated by the Ziman formula with η=0.60 nm shows excellent agreement with the $\kappa_{\parallel}$ data. The best fitted sample surface roughness η is only slightly smaller than the experimental measured rms of a-Si NTs (0.815±0.04 nm, see Figure 2.11). This small discrepancy is likely due to the fact that Ziman model tends to under-estimate 'p'[60]. Furthermore, instead of using Ziman's formula, we found that using a constant p of 0.35 also fits well the in-plane data. This is consistent with the p value obtained from the MFP reconstruction processes from the $\kappa_{\parallel}$ and $k_{\perp}$ data at 300 K.

With exactly the same parameters, we also modeled the temperature dependent behavior for NTs and films, as shown in Figure 2.9. The fitting agrees well with the experimental data for all the films and NTs down to 150 K, while below 150 K, the model shows slightly higher values compared to the experimental results. This indicates that our model for κ_{p} may underestimate the scattering strength for propagons at low temperature, or ω_c could be different at lower temperature. After fitting with all the temperature data for films and NTs, we also calculated bulk propagon thermal conductivity (*i.e.*, $\kappa_{\mathrm{p,bulk}}$ in Eq. 2.18 and 2.19), which are 4.9, 4.88, 4.73, 4.48 W.m^{-1}.K^{-1} at 300, 200, 100, and 70 K, respectively.

2.8 Conclusion

We utilized novel structures of a-Si nanotubes and suspended a-Si films to systematically studied size dependent thermal conductivity of a-Si nanostructures. The $\kappa_{\parallel}$ measurements eliminated the influence of the thermal contact resistance and enabled precise measurement over a wide size range of ~5 nm to 1.7 μm. The $\kappa_{\parallel}$ data showed unexpectedly high in-plane thermal conductivity ($\kappa_{\parallel}$ >3 W.m^{-1}K^{-1}) in a-Si nanotubes and films of ~100 nm thickness, which is further increased to ~5.3 W.m-1K-1 in 1.7 m thick film. The measured $\kappa_{\parallel}$ is significantly higher than that of $\kappa_{\perp}$ for films of of ~26 nm to 1.7 m thick. We find that the propagons have MFP spectra ranging from 10 nm to 10 m at 300 K, and the contribution to propagon thermal conductivity from propagons with MFP greater than 1 μm increase from ~30 % at 300K to ~50 % at 70 K. We also carried out phenomenological modeling to correlate the propagon scattering mechanisms to the observed MFP distribution, and showed that partially specular scattering boundary scattering and the broad MFP spectra account for the large κ anisotropy in the a-Si NTs and films.

Acknowledgments

Chapter 2 is a reprint of S. Kwon*, J. Zheng*, M. C. Wingert, S. Cui, and R. Chen, “Unusually High and Anisotropic Thermal Conductivity in Amorphous Silicon Nanostructures,” ACS Nano, 11, 2470-2476 (2017). *These authors contributed equally to the respective works.

References

1. T. Matsui, H. Sai, K. Saito and M. Kondo, Progress in Photovoltaics: Research and Applications **21** (6), 1363-1369 (2013).

2. L. Dong, R. Yue and L. Liu, presented at the TRANSDUCERS, Solid-State Sensors, Actuators and Microsystems, 12th International Conference on, 2003, 2003 (unpublished).

3. L. Dong, R. Yue and L. Liu, Journal of microelectromechanical systems **14** (5), 1167-1177 (2005).

4. M. Powell, C. Van Berkel and J. Hughes, Applied Physics Letters **54** (14), 1323-1325 (1989).

5. M. J. Powell, Ieee T Electron Dev **36** (12), 2753-2763 (1989).

6. C.-S. Yang, L. Smith, C. Arthur and G. Parsons, Journal of Vacuum Science & Technology B **18** (2), 683-689 (2000).

7. M. C. Wingert, J. Zheng, S. Kown and R. Chen, Semiconductor Science and Technology **31**, 113003 (2016).

8. A. Einstein, Ann. Phys. **340**, 679 (1911).

9. G. A. Slack, Solid state physics **34**, 1-71 (1979).

10. D. G. Cahill, S. K. Watson and R. O. Pohl, Physical Review B **46** (10), 6131-6140 (1992).

11. S. M. Lee, D. G. Cahill and T. H. Allen, Phys Rev B **52** (1), 253-257 (1995).

12. M. A. Panzer, M. Shandalov, J. A. Rowlette, Y. Oshima, Y. W. Chen, P. C. McIntyre and K. E. Goodson, IEEE Electron Device Letters **30** (12), 1269-1271 (2009).

13. S. M. Lee, G. Matamis, D. G. Cahill and W. P. Allen, Microscale Thermophysical Engineering **2** (1), 31-36 (1998).

14. J. L. Braun, C. H. Baker, A. Giri, M. Elahi, K. Artyushkova, T. E. Beechem, P. M. Norris, Z. C. Leseman, J. T. Gaskins and P. E. Hopkins, Phys Rev B **93** (14), 140201 (2016).

15. D. G. Cahill, M. Katiyar and J. Abelson, Phys Rev B **50** (9), 6077 (1994).

16. X. Liu, J. Feldman, D. Cahill, R. Crandall, N. Bernstein, D. Photiadis, M. Mehl and D. Papaconstantopoulos, Physical review letters **102** (3), 035901 (2009).

17. S. Moon, M. Hatano, M. Lee and C. P. Grigoropoulos, International Journal of Heat and Mass Transfer **45** (12), 2439-2447 (2002).

18. H.-S. Yang, D. G. Cahill, X. Liu, J. Feldman, R. Crandall, B. Sperling and J. Abelson, Phys Rev B **81** (10), 104203 (2010).

19. B. Kuo, J. Li and A. Schmid, Applied Physics A **55** (3), 289-296 (1992).

20. L. Wieczorek, H. Goldsmid and G. Paul, in *Thermal Conductivity 20* (Springer, 1989), pp. 235-241.

21. K. T. Regner, D. P. Sellan, Z. Su, C. H. Amon, A. J. McGaughey and J. A. Malen, Nature communications **4**, 1640 (2013).

22. H. Goldsmid, M. Kaila and G. Paul, physica status solidi (a) **76** (1), K31-K33 (1983).

23. P. Fan, W. F. Fan, Z. H. Zheng, Y. Zhang, J. T. Luo, G. X. Liang and D. P. Zhang, J Mater Sci-Mater El **25** (11), 5060-5065 (2014).

24. P. B. Allen and J. L. Feldman, Physical Review B **48** (17), 12581 (1993).

25. P. B. Allen, J. L. Feldman, J. Fabian and F. Wooten, Philosophical Magazine B **79** (11-12), 1715-1731 (1999).

26. J. L. Feldman, M. D. Kluge, P. B. Allen and F. Wooten, Phys Rev B **48** (17), 12589 (1993).

27. Z. T. Tian, K. Esfarjani, J. Shiomi, A. S. Henry and G. Chen, Applied Physics Letters **99** (5) (2011).

28. J. M. Larkin and A. J. H. McGaughey, Physical Review B **89** (14), 144303 (2014).

29. N. B. Li, J. Ren, L. Wang, G. Zhang, P. Hanggi and B. W. Li, Rev Mod Phys **84** (3), 1045-1066 (2012).

30. S. Y. Xiong, K. Saaskilahti, Y. A. Kosevich, H. X. Han, D. Donadio and S. Volz, Phys Rev Lett **117** (2), 025503 (2016).

31. D. G. Cahill, P. V. Braun, G. Chen, D. R. Clarke, S. H. Fan, K. E. Goodson, P. Keblinski, W. P. King, G. D. Mahan, A. Majumdar, H. J. Maris, S. R. Phillpot, E. Pop and L. Shi, Appl Phys Rev **1** (1), 011305 (2014).

32. B. Zink, R. Pietri and F. Hellman, Physical review letters **96** (5), 055902 (2006).

33. S. M. Lee and D. G. Cahill, Journal of applied physics **81** (6), 2590-2595 (1997).

34. Q. Fu, J. Yang, Y. Chen, D. Li and D. Xu, Applied Physics Letters **106** (3), 031905 (2015).

35. T. Zhan, Y. Xu, M. Goto, Y. Tanaka, R. Kato, M. Sasaki and Y. Kagawa, Appl Phys Lett **104** (7), 071911 (2014).

36. A. J. Minnich, Physical review letters **109** (20), 205901 (2012).

37. M. C. Wingert, S. Kwon, M. Hu, D. Poulikakos, J. Xiang and R. Chen, Nano Letters **15** (4), 2605-2611 (2015).

38. K. Laaziri, S. Kycia, S. Roorda, M. Chicoine, J. Robertson, J. Wang and S. Moss, Physical review letters **82** (17), 3460 (1999).

39. M. C. Wingert, Z. C. Chen, S. Kwon, J. Xiang and R. Chen, Review of Scientific Instruments **83** (2), 024901 (2012).

40. A. I. Hochbaum, R. K. Chen, R. D. Delgado, W. J. Liang, E. C. Garnett, M. Najarian, A. Majumdar and P. D. Yang, Nature **451** (7175), 163-U165 (2008).

41. D. G. Cahill, Review of scientific instruments **61** (2), 802-808 (1990).

42. J. Zheng, M. C. Wingert, E. Dechaumphai and R. Chen, Review of Scientific Instruments **84** (11), 114901 (2013).

43. T. Borca-Tasciuc, A. Kumar and G. Chen, Review of scientific instruments **72** (4), 2139-2147 (2001).

44. C. Jeong, S. Datta and M. Lundstrom, Journal of Applied Physics **111** (9), 093708 (2012).

45. H.-S. Yang, D. G. Cahill, X. Liu, J. L. Feldman, R. S. Crandall, B. A. Sperling and J. R. Abelson, Physical Review B **81** (10), 104203 (2010).

46. J. E. Turney, A. J. McGaughey and C. H. Amon, Journal of Applied Physics **107** (2), 024317 (2010).

47. D. P. Sellan, J. Turney, A. J. McGaughey and C. H. Amon, Journal of Applied Physics **108** (11), 113524 (2010).

48. J. Cuffe, J. K. Eliason, A. A. Maznev, K. C. Collins, J. A. Johnson, A. Shchepetov, M. Prunnila, J. Ahopelto, C. M. S. Torres and G. Chen, Physical Review B **91** (24), 245423 (2015).

49. F. Yang and C. Dames, Physical Review B **87** (3), 035437 (2013).

50. H. Zhang, X. Chen, Y.-D. Jho and A. J. Minnich, Nano letters **16** (3), 1643-1649 (2016).

51. Y. J. Hu, L. P. Zeng, A. J. Minnich, M. S. Dresselhaus and G. Chen, Nat Nanotechnol **10** (8), 701-706 (2015).

52. A. J. Minnich, J. A. Johnson, A. J. Schmidt, K. Esfarjani, M. S. Dresselhaus, K. A. Nelson and G. Chen, Physical Review Letters **107** (9) (2011).

53. C. Jeong, S. Datta and M. Lundstrom, Journal of Applied Physics **109** (7), 073718 (2011).

54. J. M. Larkin and A. J. McGaughey, Physical Review B **89** (14), 144303 (2014).

55. P. Sheng and M. Zhou, Science **253** (5019), 539-542 (1991).

56. J. Graebner, B. Golding and L. Allen, Phys Rev B **34** (8), 5696 (1986).

57. E. H. Sondheimer, Advances in physics **50** (6), 499-537 (2001).

58. M. Asheghi, M. Touzelbaev, K. Goodson, Y. Leung and S. Wong, Journal of Heat Transfer **120** (1), 30-36 (1998).

59. J. M. Ziman, *Electrons and phonons: the theory of transport phenomena in solids*. (Oxford University Press, 1960).

60. A. Malhotra and M. Maldovan, Scientific Reports **6**, 25818 (2016).

61. X. Liu, B. White Jr, R. Pohl, E. Iwanizcko, K. Jones, A. Mahan, B. Nelson, R. Crandall and S. Veprek, Physical review letters **78** (23), 4418 (1997).

62. X. Liu and R. Pohl, Phys Rev B **58** (14), 9067 (1998).

Chapter 3: Thermal Conductivity and Specific Heat of Nylon Nano-fibers

3.1 Introduction

Nanostructured materials often exhibit distinct thermophysical properties compared to their bulk counterparts due to size effects, and have therefore attracted extensive research interest over the past decades. One of the widely studied parameters is the thermal conductivity (κ) of individual nanostructures[1]. These measurements have shed lights on phonon transport mechanisms in nanowires[2, 3], nanotubes[4, 5], and more recently two dimensional (2D) materials[6-10]. On the other hand, specific heat (C_p) is also an important property that reflects the thermodynamics of solids, and in the case of dielectric materials, the phonon spectra [11, 12]. However, due to the small volume and mass, specific heat measurements of individual rod-like and 2D nanostructures have been very challenging and less explored. The most common method is based on the measurement of ensembles of nanostructures using commercial calorimeters, usually with masses on the order of nano- to micro-grams. For instance, Hone *et al.*[11] investigated the C_p of single-wall carbon nanotube (CNT) bundles and showed quantized phonon spectra in the reduced dimensionality within the temperature range of 2 to 8 K. Dames *et al.*[12] found that the C_p of anatase TiO_2 nanotube ensembles exhibits a significant increase over the bulk value below 50 K, presumably also due to the confined phonon spectra. Using a miniaturized AC calorimeter [13], J. Kurtz *et al.*[14] measured C_p of superconducting Zn nanowires with 0.1 mg mass, and revealed that the thermodynamic properties of superconducting Zn NWs are still three-dimensional, even when the nanowire diameter is below the superconducting coherence length. Lu *et al.*[15] presented a 3ω self-heating method to measure the C_p of bundles of multiwall CNTs with nano-gram scale mass.

However, these previous measurements on the specific heat of NWs[14] and NTs[11, 12] were carried out on ensembles or bundles of nanostructures. It requires great effort to identify the coupling effect between the NWs/NTs in these measurements, especially at low temperature. In addition, nanostructures inherently exhibit inhomogeneity among samples and the average properties of ensembles might not truly represent the individual ones. Also, it would be difficult in many cases to collect nanostructures with sufficiently large quantity and uniformity. Lu's 3ω method [15] can in principle be extended to individual nanostructures, but the self-heating technique would only work for metallic structures. Therefore, it is attractive to be ale to measure the specific heat of individual free-standing nanostructures, especially those made from semiconductors which may not be compatible with the self-heating 3ω technique. Such measurements will shed lights on the phonon spectra of individual nanostructures without the influence of inter-structure coupling. While the thermal conductivity of single nanostructures has been measured extensively[1, 2, 16, 17], to our best knowledge, the specific heat of individual nanostructures, such as nanowires and 2D structures which often possess mass below 10^{-11}g, has not yet been measured.

In this work, we show for the first time the simultaneous measurements of thermal conductivity and specific heat of individual 1D nanostructures, demonstrated on Nylon-11 nanofibers (NFs) with approximate masses of 2×10^{-14} g. Our results show the κ of these approximately 600-700 nm diameter (D) NFs are enhanced by about ~50%

compared to bulk values while C_p remains bulk-like. Temperature dependent measurements indicate that the thermal diffusivity α ($\alpha = \kappa / \rho C_p$), which reflects phonon mean free path l, is decreasing with temperature, indicating that anharmonic phonon-phonon scattering plays a role in the NFs. Therefore, combined κ and C_p measurements provide new insights regarding phonon spectrum and transport physics. Our technique can be readily extended to other nanostructures, provided that the conditions on the sample geometries are satisfied.

3.2 Devices and Samples Preparation

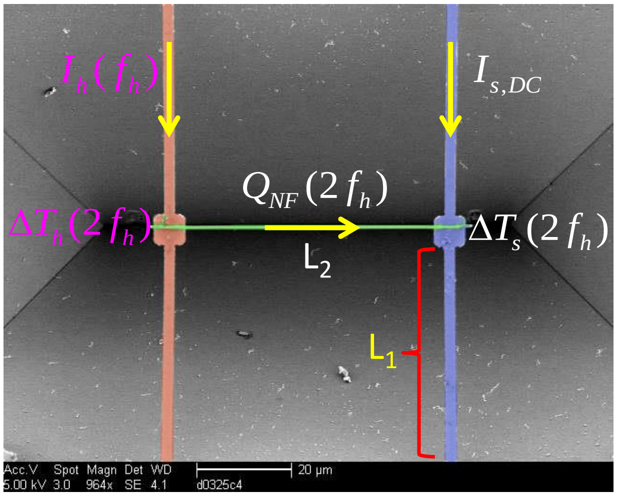

Figure 3.1: Scanning electron microscopy (SEM) image of the micro-fabricated suspended device for simultaneous κ and C_p measurements of individual nanofibers (NFs). The heating side (left side) temperature, ΔT_h, oscillates at $2f_h$ with a modulated current, $I_h(f_h)$. A portion of the heat current, Q_{NF}, is conducted along the NF to the sensing side (right side), raising its temperature to ΔT_s, which is measured using a full Wheatstone bridge[18] with a DC driving current. The half-beam length of the device (L_1) is 50 μm, and the length of the NF (L_2) is about 50 μm.

We have designed and fabricated micro-devices for simultaneous κ and C_p measurements of rod-like structures such as NFs, as shown in Fig. 3.1. The device consists of two suspended SiNx beams with integrated deposited Pt thin films. The beams are approximately 2 μm wide and 100 μm long. The thickness of the SiNx and Pt are 100 nm and 60 nm, respectively.

Devices were fabricated on a <100> Si wafer using micro-fabrication techniques. A 300-nm thick film of silicon nitride (SiN_x) was deposited on Si using plasma-enhanced chemical vapor deposition (PECVD) (Fig. 3.2(a)). The uniformity and low stress characteristics of the deposited SiN_x film were obtained using mixed frequency PECVD to control film stress and density. A PMMA (poly-(methyl-methacrylate)) layer was spin-coated and patterned using electron beam lithography (EBL). After electron beam pattern exposure, the sample was developed using MIBK:IPA (1:3) and underwent further descum using O_2 plasma to eliminate possible organic/photoresist residuals. 10 nm thick Cr and 40 nm thick Pt films were then sputtered, where Cr was used as an adhesion layer between SiN_x and Pt. PMMA lift-off was then carried out using acetone. EBL patterning after lift-off is shown in Fig. 3.2(b).

EBL was also used to pattern a window in the SiN_x film in order to release the suspended beam structure (Fig. 3.2(c)). The SiN_x window was selectively etched by reactive ion etching (RIE) with CHF_3 and O_2. PMMA was then removed using acetone, leaving a window for selective silicon etching, shown in Fig. 3.2(d). The suspended structure was released by wet etching of Si under the SiN_x beams in a KOH solution at 80 ^oC for approximately 1 hr (etching rate approximately ~ 1 μm/min). The sample was cleaned after KOH etching by dipping in DI water and methanol. Methanol was used due to its low surface tension to ensure that the device would not collapse during air-drying.

No critical point drying was used in the fabrication process. Fig. 3.2(e) shows the final fabricated device.

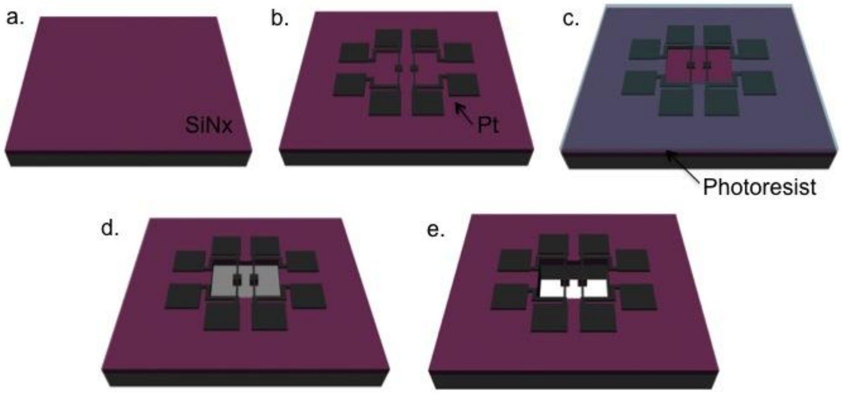

Figure 3.2: Device fabrication flow: (a) Coating of the Si wafer by low-stressed SiN_x using PECVD. (b) Patterning and lift-off to define the beams and pads made of Pt. (c) Opening of the window for subsequent SiN_x etching. (d) Etching of SiN_x. (e) Release of the suspended structures by etching the Si substrate using KOH.

The Nylon-11 NFs were fabricated using the electrospinning method[19] by Dr. Z. Jiang (Argonne National Laboratory), and were transferred to suspended devices using a custom-built optical micro-manipulator[20], as shown in Fig. 3.1. The diameters of the NFs were determined using scanning electron microscopy (SEM).

3.3 Measurement Principles

We used an AC heating scheme for the κ and C_p measurements. As shown in Fig. 3.1, in this scheme, the left beam, referred to as the 'heating' beam, is used for joule heating by applying an alternating current (AC), $I_h(f_h)$, modulated at frequency f_h. The NF sample bridging the centers of the two beams conducts a portion of the heat current to the other beam, referred to as the 'sensing' beam. In our experiments, the temperature rise of the heating beam, $\Delta T_h(2f_h)$, was measured from the root mean square (RMS) of the 3rd harmonic voltage ($V_{h,3f_h}$) using a lock-in amplifier (Stanford Research SR830). Such a modulated self-heating method, widely known as the '3ω method', has been used for measuring κ and C_p of suspended rod-like structures[15, 21]. On the sensing beam, we used a differential bridge scheme [18], which has been shown by us [22] and Sadat *et al.*[23] to achieve sub-100 μK resolution. The temperature rise of the sensing beam, $\Delta T_s(2f_h)$, also oscillating at frequency $2f_h$, was measured from the RMS of the 2nd harmonic voltage ($V_{s,2f_h}$) using another lock-in amplifier with a DC driving current ($2I_{s,DC}$) applied to the bridge circuit[24]. The complete circuit setup is shown in Fig. 3.3.

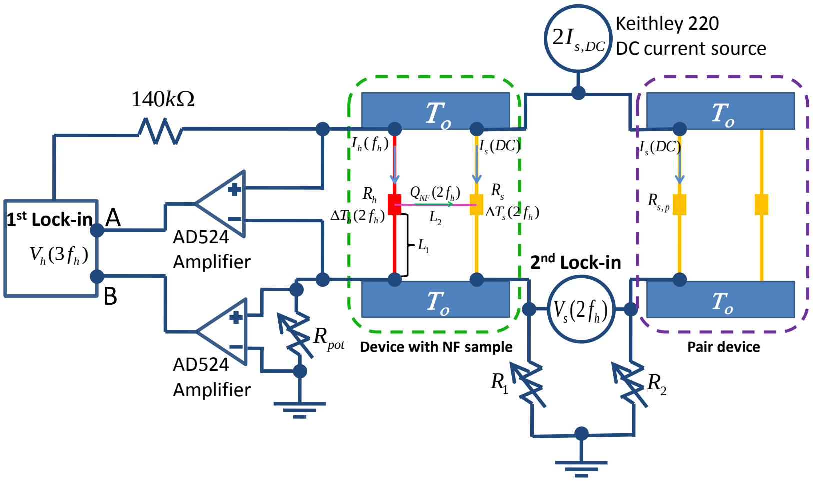

Figure 3.3: Circuit diagram of the experimental setup.

In the low-frequency regime, the temperature on the heating and sensing sides are related to the measured voltage by:

$$\Delta T_h = 3\frac{V_{h,3f_h}}{I_{f_h}}\left(\frac{dR_h}{dT}\right)^{-1} \tag{3.1}$$

$$\Delta T_s = \sqrt{2}\,\frac{V_{s,2f_h}\left(R_s + R_{s,p} + R_1 + R_2\right)}{I_{s,DC}R_2}\left(\frac{dR_s}{dT}\right)^{-1} \tag{3.2}$$

where I_{f_h} and $I_{s,DC}$ are the RMS of the AC heating current and amplitude of the applied DC sensing current, respectively. dR_h / dT and dR_s / dT are the temperature coefficients of resistance (TCR) for the heating and sensing beams, respectively. R_s, $R_{s,p}$, R_1, and R_2 are the four resistors in the bridge circuit. Note that R_s and $R_{s,p}$ are located inside the vacuum chamber and will change when the sample temperature changes.

3.4 Analytical and Numerical Model for C$_p$ Extraction

The experimental system can be simplified as a one-dimensional system as shown schematically in Fig. 3.4.

For the nanofiber (NF) and sensing beams, the one-dimensional (1D) steady-state heat conduction equation in the frequency domain can be written as[25]:

$$\frac{d^2\Delta T\left(x,\omega\right)}{dx^2} = a^2\Delta T\left(x,\omega\right) \tag{3.3}$$

For the sensing beam:

$$\Delta T_{s,beam}\left(x,\omega\right) = C_1\cosh(a_1 x) + C_2\cosh(a_1 x) \tag{3.4}$$

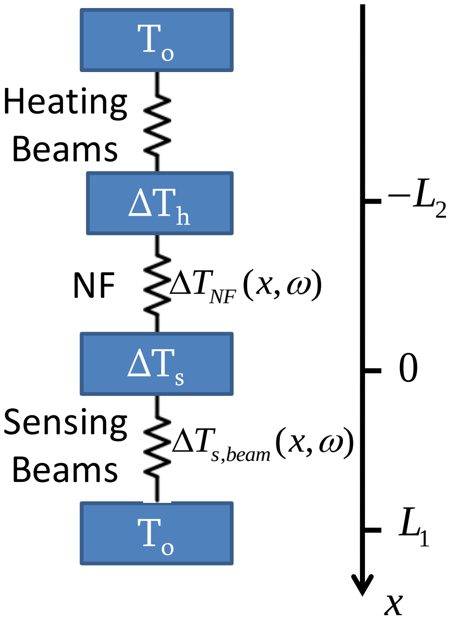

Figure 3.4: Equivalent circuit diagram of the 1D analytical model. $\Delta T_h(\omega)$ can be calculated from Lu *et al.*'s analytical model[15]. The 1D steady-state heat conduction equation in the frequency domain is solved to get $\Delta T_s(\omega)$. The temperature profile of NF is $\Delta T_{NF}(x,\omega)$, and that of sensing beams is $\Delta T_{s,beam}(x,\omega)$.

For the NF:

$$\Delta T_{NF}\left(x,\omega\right)=C_3\cosh(a_2 x)+C_4\cosh(a_2 x) \tag{3.5}$$

where C_1, C_2, C_3 and C_4 are unknown constants; $a=\sqrt{\dfrac{j\omega\rho c}{\kappa}}$, j is the imaginary unit; ρ, c and κ represent density, specific heat, and thermal conductivity, respectively; and ω is the thermal angular frequency. Note that the thermal angular frequency is twice the electrical angular frequency in our measurement. Subscript '1' is for the beams and subscript '2' is for the NF.

The boundary conditions are:

$$\Delta T_{NF}\left(-L_2,\omega\right)=\Delta T_h\left(\omega\right) \tag{3.6}$$

$$\Delta T_{NF}\left(0,\omega\right)=\Delta T_{s,beam}\left(0,\omega\right) \tag{3.7}$$

$$\kappa_1 A_1 \frac{\partial \Delta T_{s,beam}}{\partial x}\Big|_{x=0} = \kappa_2 A_2 \frac{\partial \Delta T_{NF}}{\partial x}\Big|_{x=0} \tag{3.8}$$

$$\Delta T_{s,beam}\left(L_1,\omega\right) = 0 \tag{3.9}$$

where L_1 is half the beam length, L_2 is the length of the NF; and A_1 and A_2 are the cross-sectional area of the beam and NF, respectively.

Equations (S2) and (S3) can be solved and the sensing side temperature can be expressed as

$$\Delta T_s\left(\omega\right) = \frac{\Delta T_h\left(\omega\right)}{\cosh(a_2 L_2) + \dfrac{\kappa_1 A_1 a_1 \sinh(a_2 L_2)}{\kappa_2 A_2 a_2 \tanh(a_1 L_1)}} \tag{3.10}$$

Here $\Delta T_h\left(\omega\right)$ can be calculated as[15]

$$\Delta T_h\left(\omega\right) = \Delta_0 \sum_{n=1}^{\infty} \frac{\left[1-\left(-1\right)^n\right]}{2n^3} \sin\frac{n\pi}{2} \frac{\exp(j\phi_n)}{\sqrt{1+\cot^2\phi_n}} \tag{3.11}$$

Where $\Delta_0 = 4I_{f_h}^2 R_h L_1 / \left(\pi^3 \kappa_1 A_1\right)$, and $\cot\phi_n = \dfrac{8\omega L_1^2 \rho_1 c_1}{\pi^2 \kappa_1 n^2}$; I_{f_h} is the root-mean-squared (RMS) value of the applied modulated current, and R_h is the resistance of the whole heating beam.

In order to evaluate the applicable range of the analytical model, a one-dimensional numerical model for this device is developed. In this model, we solve the heat conduction equation for the heating and sensing beams, as well as the NW specimen, which can be written as:

$$\left(\rho C\right)_i \frac{\partial T}{\partial t} = \kappa_i \frac{\partial^2 T}{\partial x^2} + q_i \tag{3.12}$$

where ρ , C and κ represent density, specific heat, and thermal conductivity, respectively; i=1 for the heating beam, i=2 for the NW sample, and i=3 for the sensing beam. In this case, $q_1 = I_h^2 R_h / \left(2A_b L_b\right)$, where R_h and A_b are the electrical resistance and cross sectional area of the heating beam, and $q_2 = q_3 = 0$.

Figure 3.5 shows the analytical and numerical model results for NFs with diameters of 150 nm and 600 nm. For D=150 nm, the results from these two models are identical. However, for D=600 nm, there is a discrepancy between these two models. This discrepancy is due to the heat capacity of the NF, *i.e.*, $\left(\rho cV\right)_{NF}$. In the model, $\left(\rho c\right)_{NF} = 1.717\times10^6 \frac{J}{m^3 \bullet K}$, $V_{NF} = \frac{L_{NF}\pi D^2}{4} = 50\mu m\times\frac{\pi D^2}{4}$, and $\left(\rho c\right)_b = 3.187\times10^6 \frac{J}{m^3 \bullet K}$, $V_b = L_b w_b t_b = 100\mu m\times 2\mu m\times 168nm = 1.68\times10^{-17} m^3$ for NF and beams, respectively.

The ratio of the heat capacity of the NF ($\left(\rho cV\right)_{NF}$) to that of the beam ($\left(\rho cV\right)_b$) is

$$\frac{\left(\rho cV\right)_{NF}}{\left(\rho cV\right)_b} = \frac{\left(\rho c\right)_{NF}}{\left(\rho c\right)_b}\frac{V_{NF}}{V_b} = 0.54\frac{V_{NF}}{V_b} \tag{3.13}$$

In the analytical model, the calculation of $\Delta T_h\left(\omega\right)$ is based on the assumption that the heat conduction to the NF is negligible, as was done by Lu et al[15]. This assumption stands for NFs with D=150 nm, because the heat capacity of the NF is much less than that of the beams, *i.e.*, $\frac{\left(\rho cV\right)_{NF}}{\left(\rho cV\right)_b} = 0.014 \ll 1$. When the diameter of the NF is large (e.g., D=600 nm), $\frac{\left(\rho cV\right)_{NF}}{\left(\rho cV\right)_b} = 0.227$. In this case, the heat capacity of the NF is on the same order of that of the beams and should be taken into account in the calculation of $\Delta T_h(\omega)$.

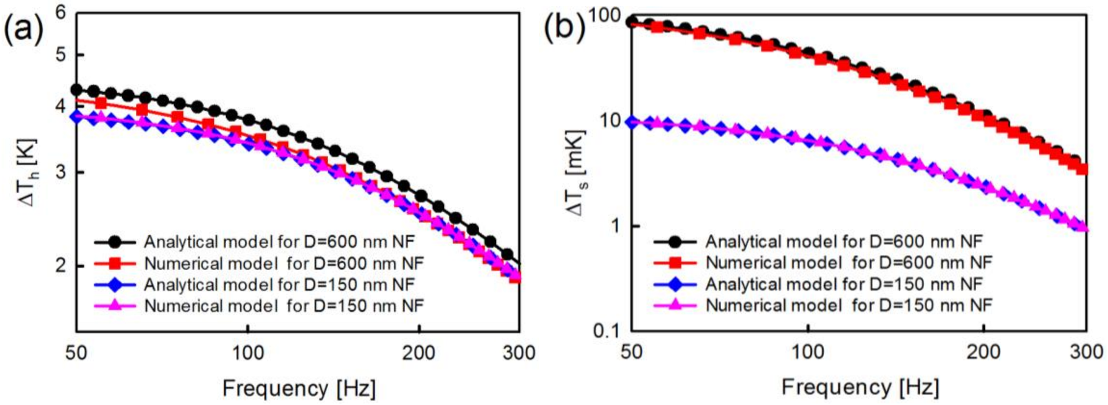

Figure 3.5: Comparison between the analytical and numerical model for (a) heating side; (b) sensing side. The analytical model calculated $\Delta \mathrm{T_h}(\omega)$ independently, without considering the NF. In contrast, the numerical model regards the heating beam, NF, and the sensing beam as a whole system. For the D=150 nm NF, the heat capacity of the NF is negligible compared to that of the beams, and the results from analytical and numerical model are identical. However, for the D=600 nm NF, the heat capacity of the NF is on the same order of magnitude as that of the beams, discrepancy exists due to the breakdown of the assumption of the analytical model. This discrepancy will be further transferred to $\Delta \mathrm{T}_s(\omega)$ according to equation (3.10).

In contrast, the numerical model takes into account the influence of the NF on the $\Delta T_h(\omega)$ calculation. Therefore, the numerical model is an accurate model for NFs with both small and large diameters. Since our NF samples are ~600-700 nm in diameter, we employed the numerical model to extract the specific heat in this work.

In the numerical model, we are able to add contact resistance (R_c) between the sample and the beams, and investigate the effect of R_c on the specific heat fitting process. In Fig 3.6(a), the black line is the frequency dependent curve of $\Delta T_{s,pad}$ without R_c, assuming the sample thermal resistance is 1 GK/W, with a sample length of 50 µm and a diameter of 600 nm. Equivalently, the sample thermal conductivity is 0.1768 W/m-K. Then we keep the total thermal resistance the same, but attribute 10% of the total thermal resistance to R_c. This means the intrinsic thermal resistance of the sample is 900 MK/W, *i.e.*, intrinsic thermal conductivity is 0.1963 W/m-K, and the contact resistance is 100 MK/W. The difference between $\Delta T_{s,pad}$ with and without R_c becomes larger with increasing frequency. Fig. 3.6(b) shows the ratio of $\Delta T_{s,pad}$ change with R_c to $\Delta T_{s,pad}$ without R_c, where $\delta\Delta T_{s,pad} = \Delta T_{s,pad,withoutRc} - \Delta T_{s,pad,withRc}$. At a frequency of around 100 Hz, 10% R_c will lead to 13% changes in $\Delta T_{s,pad}$, which has the same order of magnitude effect on the $\Delta T_{s,pad}$ as the effect from specific heat, as shown in Fig. 3.7(b). Therefore, we should take into account R_c if it is large. As pointed out by Zhong *et al.*[26], the R_c between Nylon-11 NFs with diameter larger than 400 nm is very small. Therefore, for the samples we measured with diameter of ~600-700 nm, the effect of R_c is negligible.

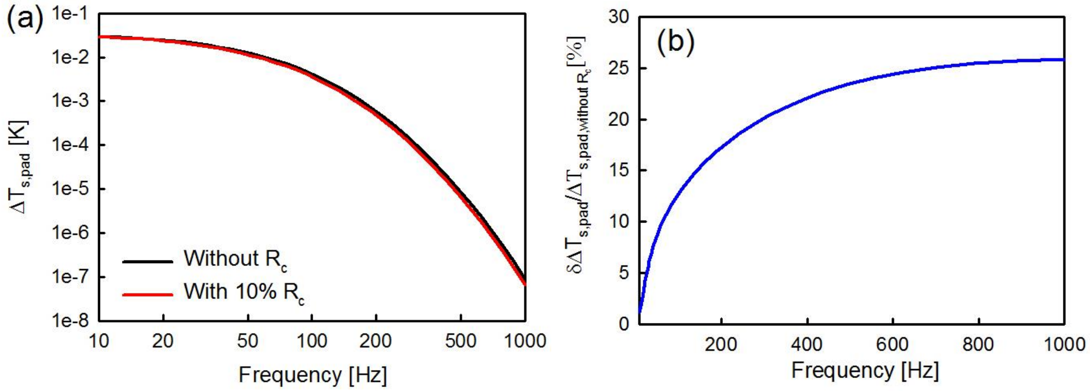

Figure 3.6: (a) Frequency dependent curve for sensing side temperature without and with 10% contact resistance. (b) The ratio of change of $\Delta T_{s,pad}$ with 10% R_c to $\Delta T_{s,pad}$ without R_c.

3.5 C_p Measurement Sensitivity

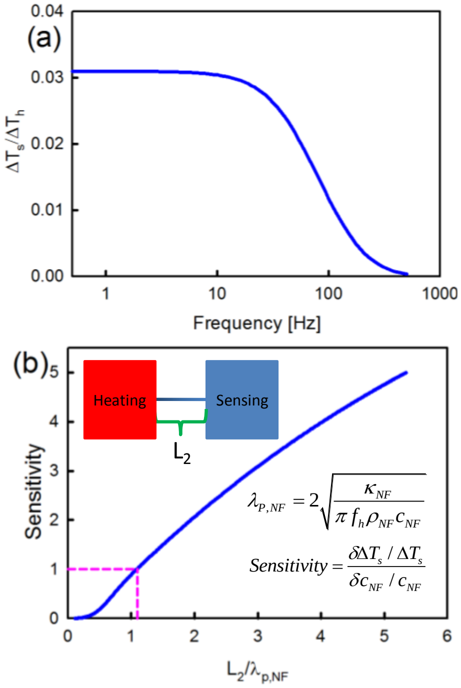

Figure 3.7: Modeled $\Delta \mathrm{T_s}/\Delta \mathrm{T_h}$ as a function of frequency ($\mathrm{f_h}$) based on Eq. (5). In the low frequency regime, $\Delta \mathrm{T_s}/\Delta \mathrm{T_h}$ is frequency-independent; when the frequency increases, the thermal penetration depth is comparable with or shorter than the length of the NF and beams, causing attenuation of the thermal wave. (b) $\mathrm{C_p}$ measurement sensitivity vs. $\mathrm{L_2}/\lambda_{p,NF}$. The sensitivity is defined as the ratio of the change of $\Delta \mathrm{T_s}$ to change in $\mathrm{C_p}$ of the NF. The thermal penetration depth of the NF, $\lambda_{\mathrm{p,NF}}$, is defined as $\lambda_{p,NF} = 2\sqrt{\frac{\alpha_{NF}}{\pi f_h}}$.When $L_2 = 1.1\lambda_{p,NF}$, the sensitivity is 1.0, meaning$\Delta \mathrm{T_s}$ is changed by 10% if $\mathrm{C_p}$ is changed by 10%.

Figure 3.7(a) plots $\Delta T_s / \Delta T_h$ as a function of the frequency (f_h) of the applied electrical current based on Eq. 3.10. As one would expect, at the low frequency ($a_1 L_1$ and $a_2 L_2 \ll 1$), $\Delta T_s / \Delta T_h$ is a constant and is only related to the ratio between the thermal conductance of the NF and the beams:

$$\frac{\Delta T_s}{\Delta T_h} = \frac{G_{NF}}{G_{NF} + G_b} \tag{3.14}$$

This is the same as the case of the DC heating scheme previously used for κ measurements of 1D nanostructures[1].

At the higher frequency, however, a_1L_1 and a_2L_2 are increasing and as a result, $\Delta T_s / \Delta T_h$ is decreasing with frequency. This occurs when the thermal penetration depth is comparable to the length of the NF (L_2) and the sensing beam (L_1), causing attenuation of the thermal wave. However, the attenuation of ΔT_s could originate from both the NF and the beams. To properly determine the experimental conditions under which the measurement is sensitive to the NF specific heat, we define and calculate the sensitivity of the C_p measurement, which measures the relative change in ΔT_s for a given change in C_p of the NF, namely, $\frac{\delta \Delta T_s / \Delta T_s}{\delta c_{NF} / c_{NF}}$. As one would expect, the sensitivity depends on the length, κ, and C_p of the NF (c_{NF}), as well as f_h. It turns out that the sensitivity only depends on one lumped dimensionless parameter, which is the ratio between the NF length and the thermal penetration depth in the NF, namely, $\frac{L_2}{\lambda_{p,NF}}$, where the penetration depth of the rod-like structure is defined as[27]:

$$\lambda_{p,NF} = 2\sqrt{\frac{\alpha_{NF}}{\pi f_h}} \tag{3.15}$$

where α_{NF} is the thermal diffusivity of the NF.

Figure 3.7(b) shows the relationship between the sensitivity and the ratio $\frac{L_2}{\lambda_{p,NF}}$. At low frequency, *i.e.*, $\frac{L_2}{\lambda_{p,NF}} \ll 1$, ΔT_s only dependents on κ_{NF} and is insensitive to c_{NF}.

As f_h increases, $\lambda_{p,NF}$ decreases and when it is comparable to L_2, ΔT_s is also sensitive to c_{NF}. At $\frac{L_2}{\lambda_{p,NF}} \approx 1.1$, the sensitivity is about 1, which means a 10% change in c_{NF} would result in a 10% change in ΔT_s. Therefore, κ_{NF} and c_{NF} can be extracted in the low and high frequency regimes, respectively. To ensure a measurement sensitivity of at least 1, it is necessary to choose experimental conditions such that $\frac{L_2}{\lambda_{p,NF}}$ is greater than 1.1. Note that both ΔT_h and ΔT_s will attenuate as f_h increases, so the highest operating frequency is limited by the temperature resolution of the measurements, which is about 50-100 μK in our experimental setup [22].

Before running the frequency-dependent measurement of $\mathrm{V_{s,2f_h}}$, we can estimate the heating frequency range that yields sufficiently high sensitivity in the specific heat measurement of the NFs. Adopting the measured thermal conductivity of the Nylon-11 NF at 615 nm ($\kappa_{\mathrm{NW}} = 0.3868\ W\ m^{-1}K^{-1}$), and bulk specific heat of the Nylon-11 NF, the cut-off frequency could be estimated at $\mathrm{R_{L-\lambda}} = \frac{L}{\lambda_p} \approx 1.1$. In other words, the estimated cut-off frequency can be written as

$$f_h = \frac{4.84 \bullet \kappa_{NF}}{\pi \rho_{NF} C_{NF} L_{NF}} = \frac{4.84 \times 0.3868}{\pi \times 1040 \times 1903.89 \times (0.0000519)^2} = 111.7 Hz \tag{3.16}$$

Therefore, to get good fitting sensitivity for the frequency-dependent curve of $\Delta \mathrm{T_{s,pad}}$, the heating frequency should be higher than 111.7 Hz. In the actual experiment, the heating frequency can usually go up to 300 Hz.

As indicated in Fig. 3.7(a), we first obtain the thermal conductance of the beams and the NFs using measurements in the low-frequency regime, in this case, at $f_h = 8.185 Hz$ [22]. The conductance of the NF (G_{NF}) is given by[1]:

$$G_{NF} = \frac{\Delta T_s}{\Delta T_h - \Delta T_s} G_b \tag{3.17}$$

We then proceeded to increase the modulation frequency f_h while keeping the heating current amplitude constant to obtain the frequency-dependent data for $V_{h,3f_h}$ and $V_{s,2f_h}$, which are fitted to the one-dimensional numerical model of the heating and sensing sides to yield the specific heat of the beam and the NF, respectively.

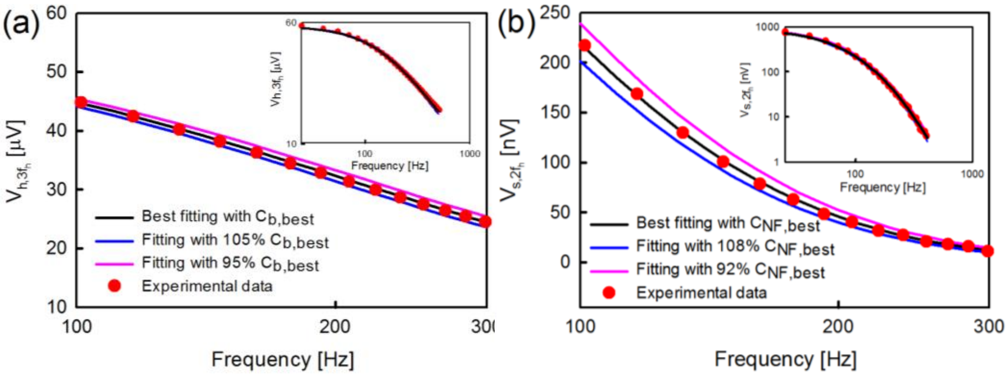

Figure 3.8: Measured frequency-dependent $V_{h,3f_h}$, $V_{s,2f_h}$, and fitting results for the (a) heating side and (b) sensing side, respectively, with f_h ranging from 100 to 300 Hz. Inset: fitting curves from 10 to 400 Hz. The data is for the NF with D=615 nm at 300 K. The blue and pink curves represent the fitting results with the largest uncertainty 5% and 8%, respectively, for the heating and sensing sides.

Fig. 3.3(a) and (b) show the best fitting results to the experimentally measured $V_{h,3f_h}$ and $V_{s,2f_h}$, respectively, on a 615 nm diameter NF. Also shown are curves representing a $\pm 5\%$

change in the C_p of the beams and a ±8% change in c_{NF}, which indicates the uncertainty of the data fitting procedure in the specific heat measurements.

3.6 Results and Discussions

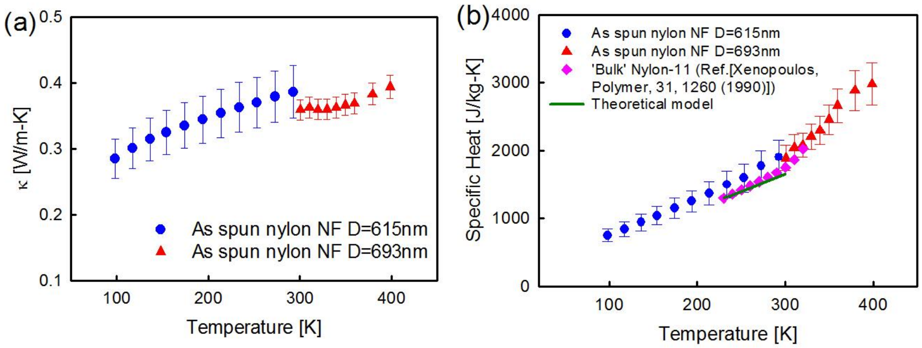

Figure 3.9: Measured temperature dependent (a) thermal conductivity and (b) specific heat for the 615 nm (blue circle) and 693 nm (red triangle) diameter Nylon-11 NFs. The increased κ of the NF compared with the bulk value, 0.24 W/m-K at 300 K, is attributed to the enhanced crystallite orientation and better aligned molecular chains. The C_p of the NFs with diameters of ~600-700 nm is similar to that of bulk Nylon-11[28] (pink diamond), which is further verified with the theoretical model[24, 28] (Green solid line).

Figure 3.9(a) shows κ_{NF} for the NFs with diameter of 615 nm (100-300 K) and of 693 nm (300-400 K). At room temperature, the measured thermal conductivities are 0.39 W/m-K and 0.36 W/m-K, respectively, which are consistent with our prior work[29] with the traditional DC heating scheme and thereby validate our AC measurements. At 300 K, the measured κ_{NF} values are approximately 50% larger than the bulk value (~0.24 W/m-K[29]), due to the better alignment of the crystallite domains in the electrospun NFs[29].

Figure 3.9(b) shows the measured specific heat of the Nylon-11 NFs. At 300 K, the measured specific heats are 1900±245 J/kg-K and 1890±187 J/kg-K for NFs with

D=615nm and 693 nm, respectively. The error bars of the measured C_p shown in Fig. 3.9(b) are the combination of the NF diameter measurement (using SEM) and the uncertainty in the data fitting (Fig. 3.8). The results are in good agreement with the bulk value 1751 J/kg-K for Nylon-11 with a similar crystallinity of 40%[28], within the uncertainty of the measurement. The specific heat of the NFs decreases with temperature, which also follows the trend of bulk Nylon-11[28]. The measurement uncertainty, about 13% and 10% for NFs with D=615nm and 693 nm, mainly comes from the geometry of the NFs (length and diameter) and the TCR of the devices. Note that the thermal contact resistance between the NFs and beams can also affect the fitting result (see Fig. 3.6). But for NFs with diameter larger than 400 nm, the thermal contact resistance is shown to be very small[29], which results in insignificant influence on the specific heat result.

It is well known that specific heat is related to a material's Debye temperature (θ_D), which is related to the Young's modulus (*E*). It has been reported that moduli of a variety of polymer NFs increase with decreasing diameter[30]. For instance, *E* of Nylon-6.6 is increased by 6 times over the bulk values when the diameter is 400 nm [30]. While there is no Young's modulus data on Nylon-11 NFs in the literature, we would expect an increase in *E* as well. To understand why the specific heat does not change in NFs of ~600-700 nm diameter, we carried out a theoretical model to examine the effect of θ_D on the specific heat of Nylon-11 following Xenopoulos *et al.*[28]. The model shows that even with a 300% increase in θ_D, which corresponds to a 900% increase in *E,* the specific heat of Nylon-11 still follows bulk-like behavior within the temperature range of 200-300 K, which is consistent with our experimental observation.

The vibrational modes of linear macromolecules, e.g., polyethylene and Nylon, can be separated into two groups[31]: skeletal vibrations and group vibrations. Both of these sources contribute to the specific heat of linear macromolecules at constant volume (C_V), *i.e.*

$$C_V = C_{V,sk} + C_{V,gr} \tag{3.18}$$

where $C_{V,sk}$ is the specific heat from skeletal vibrations, and $C_{V,gr}$ the specific from the group vibrations.

Based on an elastic rod approximation model and considering anisotropic effects of the molecular chains, Tarasov[32] derived an expression for the specific heat of skeletal vibration modes:

$$\frac{C_{V,sk}}{N_{sk}R} = D_1\left(\frac{\theta_1}{T}\right) - \left(\frac{\theta_3}{\theta_1}\right)\left[D_1\left(\frac{\theta_3}{T}\right) - D_3\left(\frac{\theta_3}{T}\right)\right] \tag{3.19}$$

where N_{sk} is the number of the skeletal modes, R is the gas constant $8.3143\frac{J}{mol \bullet K}$, θ_1 is the one-dimensional (1D) Debye temperature, θ_3 the three-dimensional (3D) Debye temperature, $D_1\left(\frac{\theta_1}{T}\right)$ is the 1D Debye function, and $D_3\left(\frac{\theta_3}{T}\right)$ is the 3D Debye function, which are given as

$$D_1\left(\frac{\theta_1}{T}\right) = \frac{T}{\theta_1}\int_0^{\frac{\theta_1}{T}} \frac{\left(\frac{\theta}{T}\right)^2 \exp\left(\frac{\theta}{T}\right)}{\left[\exp\left(\frac{\theta}{T}\right) - 1\right]^2} d\left(\frac{\theta}{T}\right) \tag{3.20}$$

$$D_3\left(\frac{\theta_3}{T}\right)=3\left(\frac{T}{\theta_3}\right)^3\int_0^{\frac{\theta_3}{T}}\frac{\left(\frac{\theta}{T}\right)^4\exp\left(\frac{\theta}{T}\right)}{\left[\exp\left(\frac{\theta}{T}\right)-1\right]^2}d\left(\frac{\theta}{T}\right) \tag{3.21}$$

Note that the 1D Debye function describes the intramolecular vibrations, and the 3D Debye function describes intermolecular vibrations[33]. The recommended parameters for Nylon-11 in the range of 230-300K are listed in Table 3.1[34].

Table 3.1: Recommended parameters for skeletal specific heat (230-300K)of Nylon-11[34].

Polymer	Number of skeletal modes	θ_1 [K]	θ_3 [K]
Nylon-11	24	419.8	67.4

Wunderlich[35] found that apart from the skeletal modes, group vibrations, *i.e.*, independent rotation and vibration due to the side atoms disturbing the linearity of the linear macromolecular structure, are necessary in the calculation of specific heat of polymers. The frequency spectra of group vibrations are obtained from the interpretation of infrared and Raman spectrum of polymers, and can be further divided into two terms: box terms and Einstein terms.

$$C_{V,gr}=C_{V,box}+C_{V,E} \tag{3.22}$$

$$\frac{C_{V,box}}{N_{box}R}=\sum_i\frac{\left(\Theta_{E,i}/T\right)^2\exp\left(\Theta_{E,i}/T\right)}{\left[\exp\left(\Theta_{E,i}/T\right)-1\right]^2} \tag{3.23}$$

$$\frac{C_{V,E}}{N_E R}=\frac{\Theta_U}{\Theta_U-\Theta_L}\left[D_1\left(\frac{\Theta_U}{T}\right)-\frac{\Theta_L}{\Theta_U}D_1\left(\frac{\Theta_L}{T}\right)\right] \tag{3.24}$$

where N_{box} and N_E are the number of modes for box terms and Einstein terms, respectively; $\Theta_{E,i} = \frac{h\upsilon_i}{k}$ represents the Einstein frequencies in kelvin, and h and k are Planck's and Boltzmann's constants, respectively. Θ_L and Θ_U are the lower and upper limit of the frequency interval within which the vibration distribution is uniform. Table 3.2 lists the approximate group vibration frequency spectra of Nylon-11[34].

Table 3.2: The approximate group vibration frequency spectra of Nylon-11[34]

Einstein terms		Box terms		
N_E	Θ_E	N_{box}	Θ_L	Θ_U
1	1009	1	2370	2428
1	886	1	2181	2193
1	4764	1	1862	1875
10	4148	0.32	863	885
10	4098	0.68	885	1061
10	2075	6.5	1698	1977
3.5	1977	4.8	1690	1874
5.2	1874	5.9	1038	1494
0.4	1494	3.06	1378	1638
3.7	1079	3.15	1378	1525
2.79	1525	0.37	1392	1417
		0.63	1258	1392
		0.28	1583	1600
		0.46	1482	1583
		0.26	1459	1482

Employing the parameters in Table 3.1 and 3.2, we can calculate C_V for Nylon-11 from equation (3.18). Then the specific heat at constant pressure (C_p) can be calculated as[34]

$$C_p = \frac{1-\sqrt{1-12RA_0\frac{T}{T_m}}}{6RA_0\frac{T}{T_m}} C_V \tag{3.25}$$

where R is the gas constant, A_0 is a experiment-fitted constant ($A_0 = 0.00801\frac{K\bullet mol}{J}$ for Nylon-11[34]), T is the temperature, and T_m is the equilibrium temperature (493 K for Nylon-11[34]).

The calculated C_p , C_V , and respective contributions from skeletal and group modes are shown in Fig. 3.10(a). Note that the parameters in Table 3.1 and Table 3.2 are only applicable for temperatures ranging between 230 and 300 K. The calculated specific heat below 230 K has not yet been demonstrated by bulk experimental data.

While previous work shows that the thermal conductivity[36] and Young's modulus[30] are significantly enhanced for Nylon NFs with diameters below 500 nm, no change of the specific heat relative to bulk value is observed for as-spun Nylon-11 NFs with diameter of around 615 nm in our measurement. Debye temperature of the materials is proportional to the square root of Young's modulus[37], *i.e.*, $\theta_D \sim \sqrt{E}$. With the increasing Young's modulus, the Debye temperature of as-spun Nylon-11 NFs will increase. Based on Arinstein *et al.*'s work, the Young's modulus of the NFs can be 10 times as large as bulk when the diameter decreases to less than 400 nm. Then θ_D would be $\sqrt{10} = 3.16$ times as large as bulk. Note that for NFs with diameter of ~600 nm, the increase of Young's modulus and Debye temperature will probably be much smaller.

Meanwhile, the Debye temperature of the materials is related to the 1D (θ_1) and 3D (θ_3) Debye temperatures in the theoretical model as[34]

$$\theta_D = \left(\theta_1 \theta_3^2\right)^{1/3} \tag{3.26}$$

Cheban *et al.* showed that macroconformation of the polymer materials probably will not change the intramolecular frequency distribution. This means that θ_1 will not change when the NFs are drawn to small diameters. Therefore, the change of θ_D is mainly from the change of θ_3. If θ_D is 3.16 times as large as bulk, equivalently θ_3 will be 5.62 times as large as bulk based on Eq. 3.26. Fig. 3.10(b) shows the calculated specific heat with bulk θ_D and $3.16\theta_D$ in the temperature range of 230-300 K. The maximum deviation is 4.5% at 230 K. The results imply that no significant change in specific heat of the NFs can be observed even though the Young's modulus is increased 10-fold, in good agreement with our experiment.

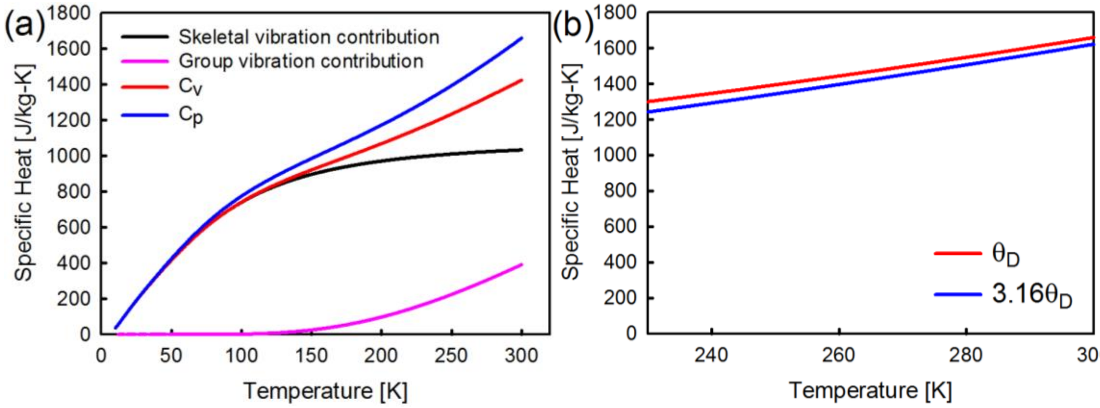

Figure 3.10: (a) Theoretical model for calculated C_p, C_V, skeletal vibration contribution, and group vibration contribution. (b) Theoretical result with θ_D and $3.16\theta_D$. The $3.16\theta_D$ case corresponds to NFs with a 10-fold increase in Young's modulus. The results imply that no significant change of the specific heat of NFs can be observed even though the Young's modulus is increased 10 times, in good agreement with our experiment.

Finally, our measurements also yield the temperature-dependent thermal diffusivity, as shown in Fig. 3.11. Based on the kinetic theory for thermal conductivity, $\alpha \sim lv$, where l is the phonon MFP and v is the phonon velocity. Assuming v is independent of temperature, Fig. 3.11 suggests that l decreases with increasing temperature between 100 and 400 K, which indicates that intrinsic anharmonic phonon scattering plays a role in the phonon transport process in the measured electrospun Nylon-11 NFs. However, the slope of l vs T is smaller than $1/T$, suggesting that scattering due to structural defects is also important in the semicrystalline NFs studied here. This is different from the case for crystalline polyethylene fibers[38] where κ scales as $1/T$ above room temperature, presumably because the PE fibers are more structurally aligned and have higher crystallinity.

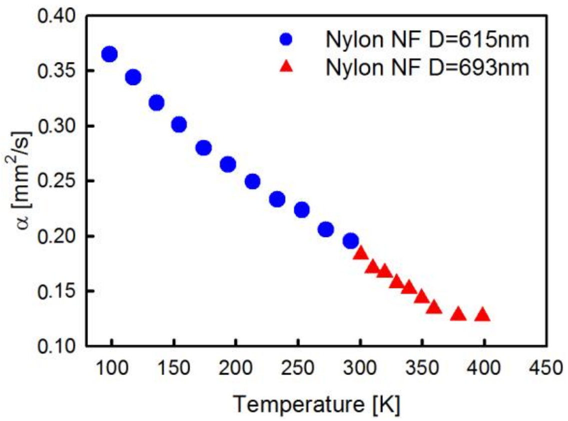

Figure 3.11: Diffusivity for the 615 nm (blue circle) and 693 nm (red triangle) diameter Nylon-11 NFs. α decreases with temperature, indicating that intrinsic phonon-phonon scattering starts playing a role in the NF.

3.7 Conclusion

In conclusion, we report the first simultaneous thermal conductivity and specific heat measurements on individual nanostructures, demonstrated on electrospun Nylon-11 NFs. The results show that the specific heat of the ~600-700 nm diameter NFs exhibit bulk-like behavior while the thermal conductivity is increased by 50% due to better alignment of crystalline domains in the electrospun NFs. The measured thermal diffusivity of the NFs decreases with temperature from 100 to 400 K, suggesting that anharmonic phonon scattering starts playing a role in phonon transport in the NFs. The platform here is also applicable for semiconductor nanostructures (1-D nanowires or 2-D thin films). The combined thermal conductivity and specific heat measurements thus provide a new platform for probing the phonon spectra and transport physics, and could find broad applications in studying semiconductor nanostructures.

Acknowledgments

The majority of chapter 3 is a reprint of J. Zheng, M. C. Wingert, and R. Chen, "Simultaneous Specific Heat and Thermal Conductivity Measurement of Individual Nanostructures," Semiconductor Science and Technology, 31(8), 084005 (2016), with some portions of J. Zheng*, M. C. Wingert*, E. Dechaumphai*, R. Chen, "Sub-picowatt/Kelvin Resistive Thermometry for Probing Nanoscale Thermal Transport," *Review of Scientific Instruments,* 84, 114901 (2013). *These authors contributed equally to the respective works.

References

1. L. Shi, D. Li, C. Yu, W. Jang, D. Kim, Z. Yao, P. Kim and A. Majumdar, Journal of Heat Transfer **125** (5), 881 (2003).

2. D. Li, Y. Wu, P. Kim, L. Shi, P. Yang and A. Majumdar, Applied Physics Letters **83** (14), 2934 (2003).

3. A. I. Hochbaum, R. K. Chen, R. D. Delgado, W. J. Liang, E. C. Garnett, M. Najarian, A. Majumdar and P. D. Yang, Nature **451** (7175), 163-U165 (2008).

4. P. Kim, L. Shi, A. Majumdar and P. L. McEuen, Physical Review Letters **87** (21) (2001).

5. J. Yang, M. Shen, Y. Yang, W. Evans, J. Z. Wei, W. Chen, A. A. Zinn, Y. Chen, R. Prasher, T. T. Xu, P. Keblinski and D. Li, Phys. Rev. Lett. **112**, 205901 (2014).

6. A. A. Balandin, S. Ghosh, W. Z. Bao, I. Calizo, D. Teweldebrhan, F. Miao and C. N. Lau, Nano Letters **8** (3), 902-907 (2008).

7. J. H. Seol, I. Jo, A. L. Moore, L. Lindsay, Z. H. Aitken, M. T. Pettes, X. S. Li, Z. Yao, R. Huang, D. Broido, N. Mingo, R. S. Ruoff and L. Shi, Science **328** (5975), 213-216 (2010).

8. M. H. Bae, Z. Y. Li, Z. Aksamija, P. N. Martin, F. Xiong, Z. Y. Ong, I. Knezevic and E. Pop, Nature Communications **4** (2013).

9. L. Lindsay and D. A. Broido, Physical Review B **84** (15) (2011).

10. I. Jo, M. T. Pettes, J. Kim, K. Watanabe, T. Taniguchi, Z. Yao and L. Shi, Nano Letters **13** (2), 550-554 (2013).

11. J. Hone, Science **289** (5485), 1730-1733 (2000).

12. C. Dames, B. Poudel, W. Z. Wang, J. Y. Huang, Z. F. Ren, Y. Sun, J. I. Oh, C. Opeil, M. J. Naughton and G. Chen, Applied Physics Letters **87** (3), 031901 (2005).

13. P. Sullivan and G. Seidel, Physical Review **173** (3), 679-685 (1968).

14. J. Kurtz, R. Johnson, M. Tian, N. Kumar, Z. Ma, S. Xu and M. Chan, Physical Review Letters **98** (24) (2007).

15. L. Lu, W. Yi and D. L. Zhang, Review of Scientific Instruments **72** (7), 2996 (2001).

16. M. C. Wingert, Z. C. Y. Chen, E. Dechaumphai, J. Moon, J.-H. Kim, J. Xiang and R. Chen, Nano Letters **11** (12), 5507-5513 (2011).

17. M. Fujii, X. Zhang, H. Xie, H. Ago, K. Takahashi, T. Ikuta, H. Abe and T. Shimizu, Physical Review Letters **95** (6) (2005).

18. M. C. Wingert, Z. C. Y. Chen, S. Kwon, J. Xiang and R. Chen, Review of Scientific Instruments **83** (2), 024901 (2012).

19. D. H. Reneker and A. L. Yarin, Polymer **49** (10), 2387-2425 (2008).

20. J. K. Yang, Y. Yang, S. W. Waltermire, T. Gutu, A. A. Zinn, T. T. Xu, Y. F. Chen and D. Y. Li, Small **7** (16), 2334-2340 (2011).

21. T. Y. Choi, D. Poulikakos, J. Tharian and U. Sennhauser, Nano Letters **6** (8), 1589-1593 (2006).

22. J. Zheng, M. C. Wingert, E. Dechaumphai and R. Chen, Review of Scientific Instruments **84** (11), 114901 (2013).

23. S. Sadat, E. Meyhofer and P. Reddy, Applied Physics Letters **102** (16), 163110 (2013).

24. W. Holmes, J. M. Gildemeister, P. L. Richards and V. Kotsubo, Applied Physics Letters **72** (18), 2250-2252 (1998).

25. X. J. Hu, A. A. Padilla, J. Xu, T. S. Fisher and K. E. Goodson, Journal of Heat Transfer **128** (2006).

26. Z. Zhong, M. C. Wingert, J. Strzalka, H.-H. Wang, T. Sun, J. Wang, R. Chen and Z. Jiang, Nanoscale **6** (14), 8283 (2014).

27. F.P. Incropera, D.P. DeWitt, T.L. Bergman, and A.S. Lavine, Introduction to Heat Transfer, 5th ed., pp. 299

28. A. Xenopoulos and B. Wunderlich, Polymer **31** (1990).

29. Zhong. Z, M. C. Wingert, J. Strzalka, H. Wang, T. Sun, J. Wang, R. Chen and Z. Jiang, Nanoscale **6**, 0.1039/C1034NR00547C (2014).

30. A. Arinstein, M. Burman, O. Gendelman and E. Zussman, Nat Nanotechnol **2** (1), 59-62 (2007).

31. M. Pyda, M. Bartkowiak and B. Wunderlich, Journal of Thermal Analysis **52** (1998).

32. V. V. Tarasov, Zh. Fiz, Khim. **24** (1950).

33. Yu. V. Cheban, S. -F. Lau and B. Wunderlich, Colloid & Polymer Science **260** (1982).

34. A. Xenopoulos and B. Wunderlich, Polymer **31** (1989).

35. B. Wunderlich, The Journal of Chemical Physics **37** (6), 1207 (1962).

36. Z. Zhong, M. C. Wingert, J. Strzalka, H.-H. Wang, T. Sun, J. Wang, R. Chen and Z. Jiang, Nanoscale **6** (2014).

37. G. Carini, G. D'Angelo, G. Tripodo, A. Bartolotta and G. D. Marco, Physical Review B **54** (1996).

38. X. Wang, V. Ho, R. A. Segalman and D. G. Cahill, Macromolecules **46** (12), 4937-4943 (2013).

Chapter 4: Phonon Engineering in Nano-crystalline Bi-Sb-Te (BST) with Dielectric Nanoparticles at Low Temperature

4.1 Introduction

Intensive research is undergoing to improve thermoelectric (TE) properties. One of the most important applications is thermoelectric cooling, with particular interest at temperature of around 300K or below. Thermoelectric cooling has many advantages, such as small size, portable, fast response, and with no moving parts. These make it a very attractive option for cooling sensors in aerospace and high power density electronics. However, the broad application of TE cooling is limited by the low energy conversion efficiency, especially at low temperature. The thermoelectric figure of merit is defined as $\mathrm{ZT} = \mathrm{S}^2\sigma\mathrm{T}/\kappa$, where S is Seebeck coefficient, σ is electric conductivity, T is temperature, κ is thermal conductivity. The representative ZT results[1-8] at low temperature are summarized in Fig. 4.1. In order to enhance the thermoelectric cooling efficiency, one need to improve the TE power factor ($\mathrm{PF} = \mathrm{S}^2\sigma$) and/or reduce the thermal conductivity.

One common method to improve ZT is to introduce nano-grained structure. The high density of grain boundaries enhance the scattering of phonon (quantum of lattice vibration), thus can effectively reduce the lattice thermal conductivity without much degradation in PF[9]. However, Wang *et al.*[10] found that the phonon transmission through the grain boundary depends on their frequency. The low frequency phonons, which tend to dominate the thermal transport at low temperature[10], have higher probability to transmit through the grain boundaries than the high frequency ones[11]. Therefore, the nano-grained structure may not effectively scatter the low frequency phonons.

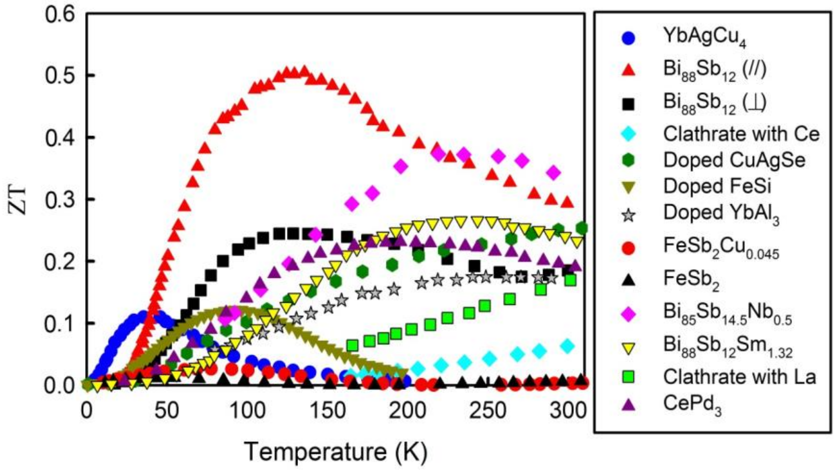

Figure 4.1: Summary of the ZT at low temperature[1-8].

One way to further suppress thermal conductivity is to embed nanoparticles (NPs) in nano-grained materials. There is plenty of previous work on embedding NPs into nano-grained materials[4, 12-16]. However, most of these work were focused on high temperature (>300K) for energy harvesting application. For example, Dou *et al.*[12] mixed 40 nm SiO_2 NPs with BST powders, and found ~20% improvement of ZT at 363 K, which is owing to both enhancing PF and reducing thermal conductivity. However, Dou *et al.*'s work didn't study the SiO_2 NPs effect at temperature below 300K. Furthermore, it will be interesting to use SiO2 NPs with size smaller than 40nm, because previous numerical study by Katcho *et al.*[17] showed that the NPs with diameter down to 10 nm can have stronger scattering effect on the lattice thermal conductivity.

In this paper, we investigated the NPs effect on lattice thermal conductivity in the NG materials at low temperature (<300K). We have mixed 10 nm SiO_2 NPs and 15 nm diamond NPs with BST nanopowders, and observed strong reduction of thermal conductivity in the NPs mixing samples. Furthermore, we found that the diamond/BST sample showed stronger scattering than the SiO_2/BST sample. This is due to the larger acoustic mismatch of the diamond/BST than that of the SiO_2/BST. The thermal boundary resistance of diamond/BSTwas found to be 10 times as large as the SiO_2/BST.

4.2 Samples Preparation and Characterization

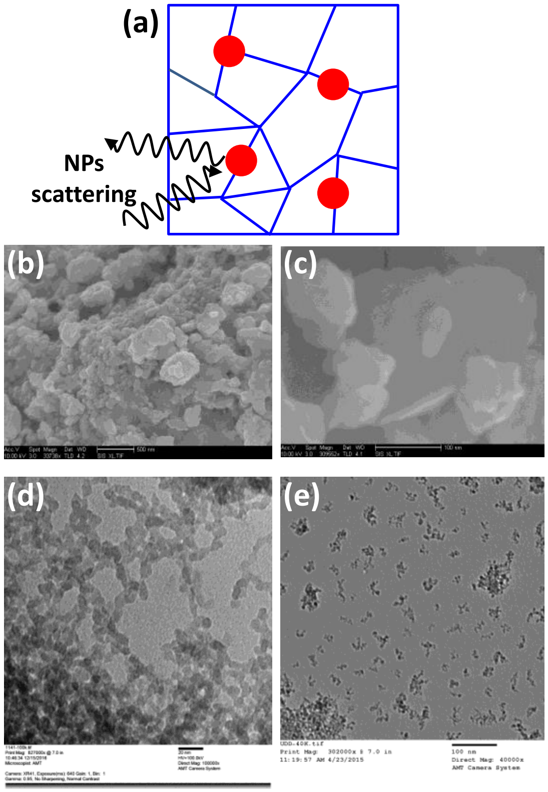

Figure 4.2: (a) Schematic of phonon scattering by NPs (red filled circles) on the grain boundaries (blue lines); SEM images of nano-powders after BM with scale bar of (b) 500nm and (c) 50nm; TEM images of (d) 10 nm SiO_2 NPs and (e) 15 nm diamond NPs.

The BST nanopowders were obtained by high energy ball milling (BM) (SPEX 8000M mixer/mill) for 10 hrs in Argon atmosphere. Then the BST nanopowders were mixed with target nanoparticles (SiO_2 or diamond) at certain volumetric concentration, and ball milled for additional 4hrs in Ethanol solution and Argon atmosphere. The wet mixing method is to avoid possible agglomeration of nanoparticles before mixing with BST nanopowders. After that, the milling jar will be moved into glovebox with O_2 level less than 0.5ppm. The mixed powders were dried up and pre-pressed into the graphite die in the glovebox. Then we conducted hot press in glovebox (400C, 60MPa, 3mins), and obtained a dense disk-like sample. The sample will be polished into regular cuboid shape (2mm*2mm*10mm). The material properties of the samples, including thermal conductivity, electrical conductivity, and Seebeck coefficient, are measured with PPMS system (Quantum Design).

Figure 4.2a shows the schematic of the NPs embedded in the BST matrix. The embedded NPs are uniformly distributed around the nano-grained boundaries. The long MFP phonons that pass through the grain boundary will be scattered by the NPs. This can effectively restrict the long MFP phonon transport, and reduce the lattice thermal conductivity in nano-grained materials.

Figure 4.2b and 4.2c show the SEM images of the nano-powders after ball milling (BM). The powder size is dominantly less than 100 nm. Fig. 4.2d and 4.2e show the TEM images of SiO_2 NPs and diamond NPs, with diameter of 10 nm and 15 nm, respectively.

The sample after hot-pressing is in disk-like shape with 1.27cm diameter and 2mm thickness, as shown in the Fig. 4.3a. Fig. 4.3b shows the XRD data for the BST samples mixing with NPs at different volumetric ratio. The average grain size can be estimated from the XRD data to be 27 nm using the Scherrer equation[18]:

$$\mathrm{D}_{\mathrm{avg}} = \frac{K\lambda}{\beta cos(\theta)}, \tag{4.1}$$

where λ is the wavelength ($\lambda = 0.154$nm), K is shape factor, β is line broadening at half the maximum intensity, θ is Bragg angle.

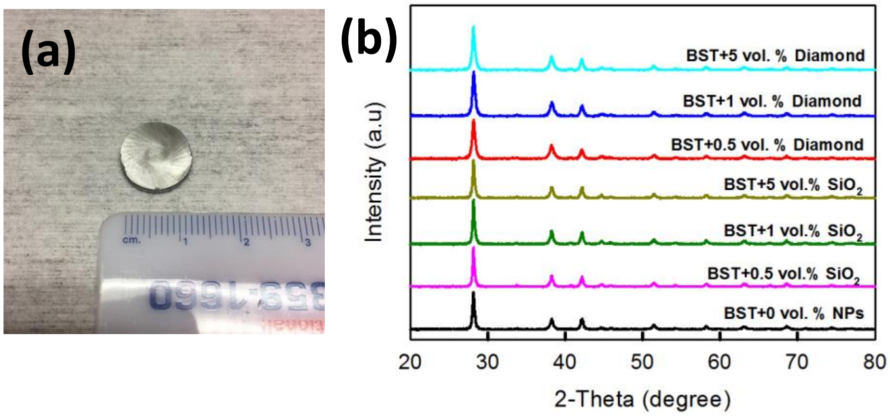

Figure 4.3: (a) Sample after hot pressing; (b) XRD characterization for BST with SiO$_2$ and diamond NPs.

4.3 Thermal Conductivity Measurement and Modeling

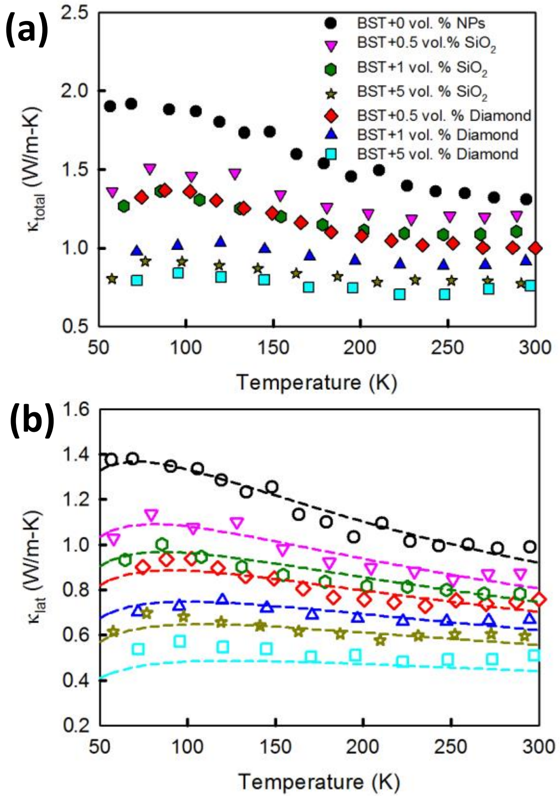

Figure 4.4: Temperature dependence of (a) measured total thermal conductivity; (b) lattice thermal conductivity. The theoretical model results with the nominal NPs diameter (10nm for SiO$_2$ NPs, and 15nm for diamond NPs) have been shown as dash line.

Figure 4.4a shows the temperature dependent measured thermal conductivity for BST mixing with SiO_2 and diamond NPs at different volumetric ratio. Comparing with the non-NPs mixing BST sample, *i.e.*, 0 vol. % NPs, the samples mixing with SiO_2 or diamond NPs show significant reduction of thermal conductivity.

The measured thermal conductivity $\kappa_{\mathrm{total}} = \kappa_e + \kappa_{bp} + \kappa_{lat}$, where κ_{e}, κ_{bp}, and κ_{lat} are majority carrier electronic, bipolar electronic, and lattice thermal conductivity, respectively. For $(Bi,Sb)_2Te_3$ materials, Kim *et al.*[19] showed that the bipolar thermal conductivity is negligible for T<300K. Therefore, the total thermal conductivity can be approximated as $\kappa_{\mathrm{total}} = \kappa_e + \kappa_{lat}$. The κ_{lat} can be obtained by subtracting κ_e from κ_{total}, as shown in Fig. 4.4b. Here the κ_e is calculated based on Wiedemann–Franz law, *i.e.*, $\kappa_e = L\sigma T$, , where σ is electrical conductivity, T is temperature, and L is Lorentz number. Fig. 4.4b shows that the κ_{lat} have been significantly reduced by embedding NPs in the BST matrix.

The lattice thermal conductivity can be modelled as[10, 20, 21]

$$\kappa_{lat} = \frac{1}{3}\sum_i \int C v_i \Lambda_{eff,i} d\omega = \frac{k_B}{6\pi^2}\left(\frac{k_B T}{\hbar}\right)^3 \sum_i \int_0^\infty \frac{x^4 e^x \Lambda_{eff,i}}{v_i^2 (e^x - 1)^2} dx, \tag{4.2}$$

where C is specific heat, i=1,2,3 represents two transverse one longitudinal phonon mode, respectively, v is speed of sound, k_B is the Boltzmann constant, $\hbar$ is the reduced Planck's constant, and $x = \frac{\hbar\omega}{k_B T}$. Λ_{eff} is the effective mean free path of phonon[10]

$$\Lambda_{eff}^{-1} = \Lambda_d^{-1} + \Lambda_u^{-1} + \Lambda_b^{-1} + \Lambda_{np}^{-1}, \tag{4.3}$$

where $\Lambda_d^{-1} = A\omega^4/v_s$ is for defect scattering, $\Lambda_u^{-1} = B\omega^2 T/v_s$ for *Umklapp* scattering, $\Lambda_b^{-1} = 0.7 D_{avg}(\omega_0/\omega)$ for frequency-dependent boundary scattering[10], and $\Lambda_{np}^{-1} = N_{np}\sigma_{np}$ for nanoparticle scattering[22, 23]. D_{avg}=27nm is the average grain size from XRD,

ω_0 is the cut-off frequency, 'A', 'B', and 'C' are adjustable parameters, $N_{np} = f/(\frac{1}{6}\pi D_{np}^3)$ is volume concentration of NPs, f is volume concentration ratio, $\sigma_{np}^{-1} = \sigma_s^{-1} + \sigma_l^{-1}$ is the effective scattering cross section, σ_s and σ_l are scattering cross section for short and long wavelength phonons, given as[22, 24]

$$\sigma_s = \pi D_{np}^2/2, \tag{4.4}$$

$$\frac{\sigma_l}{\pi D_{np}^2} = \frac{1}{144} E\left(qD_{np}\right)^4 \delta^2, \tag{4.5}$$

where $\delta = \sqrt{(\Delta\rho/\rho)^2 + 3(2\Delta\nu/\nu)^2}$, $\Delta\rho/\rho$ and $\Delta\nu/\nu$ are difference of density and speed of sound, respectively, $q = \omega/\nu$ is the phonon wave vector, and E is an adjustable parameter.

To fit the model with experimental κ_{lat} in Fig. 3b, we firstly adjust the 'A', 'B', and 'C' with $f = 0$ for the non-NPs mixing sample. The model fits well with the experimental data for the non-NPs mixing sample, and the optimal parameters are $A = 2.76 \times 10^{-41}\ s^{-1} rads^{-4}$, $B = 1.10 \times 10^{-17}\ s^{-1} K^{-1} rads^{-2}$. Kim *et al.*[25] measured and fitted the κ_{lat} of bulk $(Bi,Sb)_2Te_3$, and found that $A = 3.73 \times 10^{-41}\ s^{-1} rads^{-4}$, $B = 1.39 \times 10^{-17}\ s^{-1} K^{-1} rads^{-2}$. The *Umklapp* scattering terms were fairly close, but the impurity scattering of Kim *et al.*'s samples was stronger than our samples, which may due to different impurity and defect concentration.

Next we consider the NP scattering effect for different mixing concentration. The diameter of SiO_2 and diamond NPs are 10 nm and 15 nm, respectively, and the volumetric concentration f varies from 0.5 %, 1 %, to 5%. By fixing the 'A', 'B', and 'C', we adjusted the parameter 'E', and found the optimal fitting results with E=7 and E=28 for the SiO_2 and diamond mixing samples, respectively. Note that we used the same 'E' for the same type of NPs at different volumetric concentration. The model fits well for both types of NPs at different volumetric concentration, as shown in Fig. 4.4b.

4.4 Mean Free Path Distribution

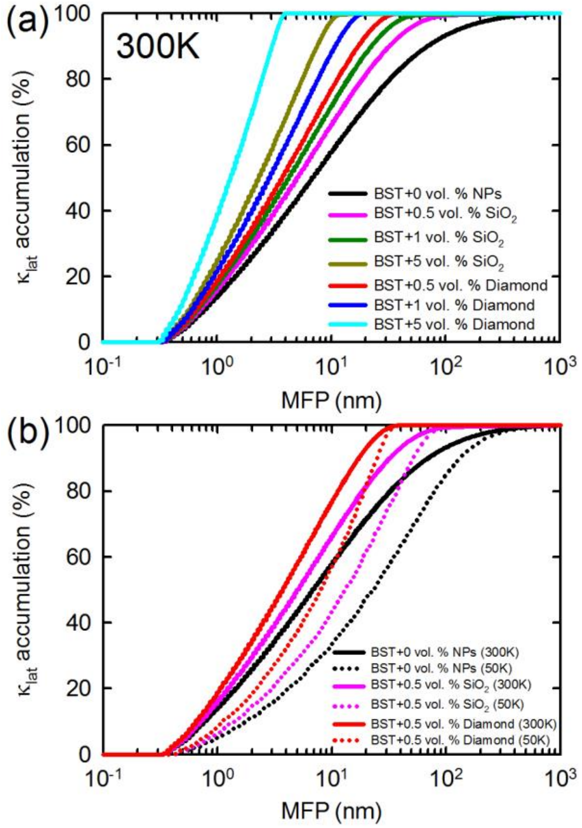

Figure 4.5: Comparison of MFP distribution for (a) different mixing NPs ratio at 300K; (b) different temperature.

Since we have seen significant reduction of lattice thermal conductivity in the NPs mixing samples in Fig. 4.4b, it will be interesting to investigate the MFP distribution of phonon in these materials. After fitting the temperature dependent κ_{lat}, we used the same fitting parameters, and calculated the corresponding MFP distribution of κ_{lat}. The MFP distribution can be modelled by transforming the integration in Eq. (2) from phonon frequency ω to phonon MFP. Fig. 4.5a shows the MFP distribution for BST samples with and without NPs at 300K. The MFP distribution of the NPs mixing samples are shift toward shorter MFP ranger than that of the non-NPs mixing sample. This clearly demonstrates that the embedded NPs can effectively scatter the long MFP phonons, thus reduced the lattice thermal conductivity. Furthermore, the MFP reduction of the 0.5 vol. % diamond sample is stronger than that of the SiO2 sample with the same mixing volumetric concentration.

The different scattering strength of SiO_2 and diamond NPs can be understood from their acoustic properties. Table 4.1 shows the mass density and speeds of sound of BST, SiO_2, and diamond. The thermal boundary resistance of medium 1 and medium 2 (e.g., SiO_2 and BST) can be calculated as[26, 27],

$$\mathrm{R_{bd}} = \left[\frac{\pi^2}{15}\frac{k_B^4}{\hbar}\left(\sum_j v_{1,j}^{-2}\Gamma_{1,j}\right)\right]^{-1} T^{-3} = \left[2.04 \times 10^{10}\left(\sum_j v_{1,j}^{-2}\Gamma_{1,j}\right)\right]^{-1} T^{-3}, \qquad (4.6)$$

where ‘j’ is phonon mode number, v is the speed of sound, Γ is heat transfer coefficient between medium 1 and medium 2, which can be calculated depending on the density ratio and speed of sound ratio of the two mediums[27]. The calculated thermal boundary resistance of SiO_2/BST and diamond/BST are listed in Table 4.2. The R_{bd} of diamond/BST is $75.06/T^3$, 10 times larger than that of SiO_2/BST ($7.58/T^3$), where ‘T’ is temperature. The large difference of R_{bd} explains the stronger scattering of the embedded diamond NPs in BST. In our theoretical model above, we have a fitting parameter ‘E’, which represents the effective scattering strength of the NPs to the phonons. The ‘E’ of the diamond/BST is ~4 times as large as that of the SiO_2/BST. The larger scattering strength in diamond/BST samples is consistent with the fact that diamond/BST interface has higher R_{bd}.

Table 4.1: Mass density and speeds of sound of BST, SiO_2 and Diamond

	Density (kg/m^3)	v_t (m/s)	v_l (m/s)
BST	6887	1780	2884
SiO_2	2660	4100	6090
Diamond	3512	17500	12800

Table 4.2: Calculated thermal boundary resistance for SiO_2/BST and Diamond/BST

	$\frac{\rho_{BST}}{\rho_{np}}$	$\frac{v_{t,BST}}{v_{t,np}}$	$\frac{v_{l,BST}}{v_{l,np}}$	Γ	R_{bd} (K-cm^2/W)	E
SiO_2/BST	2.59	0.43	0.47	2.4	$7.58/T^3$	7
Diamond/BST	1.96	0.14	0.16	2	$75.06/T^3$	28

We also investigated the low temperature effect on phonon MFP distribution, as shown in Fig. 4.5b. We compared the MFP distribution for non-NPs mixing sample, 0.5 vol. % SiO_2 and diamond NPs mixing samples at 300K and 50K, and found that at 50K, the MFP distribution is significantly moved to long MFP range. For example, phonons with MFP larger than 50 nm contribute 20% of lattice thermal conductivity at 300K for the non-NPs mixing sample. When temperature decreases to be 50K, this ratio increases to 40%. Since the embedded NPs will dominantly scatter the long MFP phonons, it will be more significant to enhance phonon scattering with NPs at low temperature than at high temperature.

4.5 Electrical Properties and ZT Measurement

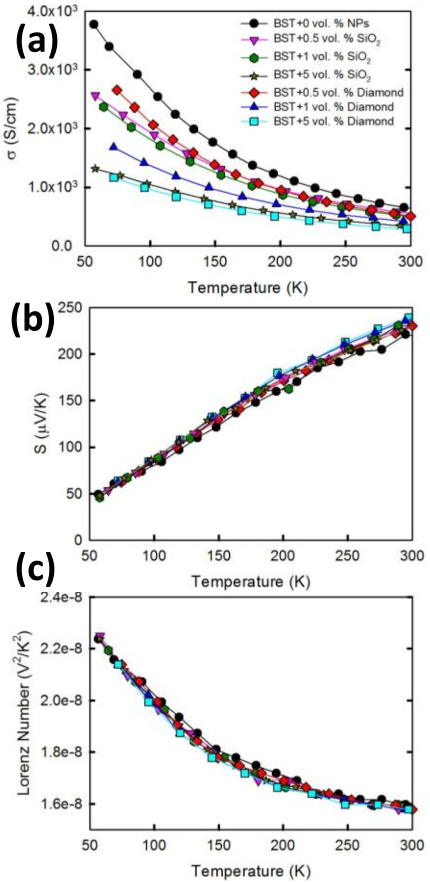

Figure 4.6: (a) Electrical conductivity, (b) Seebeck coefficient, and (c) Calculated Lorenz number for BST mixing with SiO_2 and Diamond NPs.

The κ_e that we used to subtract from κ_{total} was modeled with Wiedemann–Franz law ($\kappa_e = L\sigma T$), which requires measured the electrical conductivity (σ) and calculated the Lorenz number. Fig. 4.6a shows the measured σ as a function of temperature for different samples. The Lorenz number can be calculated with single parabolic band model[28-30], which is obtained by solving Boltzmann transport equation,

$$L = \left(\frac{k_B}{e}\right)^2 \left[\frac{(r+7/2)F_{r+5/2}(\eta)}{(r+3/2)F_{r+1/2}(\eta)} - \left(\frac{(r+5/2)F_{r+3/2}(\eta)}{(r+3/2)F_{r+1/2}(\eta)}\right)^2\right], \quad (4.7)$$

where λ is scattering parameter (λ=-1/2 for acoustic phonon scattering). η is the reduced Fermi energy, which can be solved with inputting measured Seebeck coefficient (Fig. 4.6b):

$$S = \frac{k_B}{e}\left(\frac{(r+5/2)F_{r+3/2}(\eta)}{(r+3/2)F_{r+1/2}(\eta)} - \eta\right), \tag{4.8}$$

where $F_j(\eta) = \int_0^\infty \frac{\epsilon^j}{1+\exp(\epsilon-\eta)} d\epsilon$ is the Fermi integral.

The calculated temperature dependent Lorenz numbers were shown in Fig. 4.6c. The Lorenz number shows strong temperature dependence, ranging from $1.6 \times 10^{-8}\ V^2/K^2$ at 300K to $2.3 \times 10^{-8}\ V^2/K^2$ at 50K.

From Fig. 4.6a, we have seen that the embedded dielectric NPs will have negative effect on the σ. This may be because of the large potential difference between the NPs and BST matrix, thus the electron transport has been partially impeded by the embedded NPs. Previous study[31] has shown that mixing NPs can potentially lower electrical conductivity. On the other hand, the Seebeck coefficient in the NPs mixing samples has been slightly improved compared with the non-NPs mixing sample, as shown in Fig. 4.6b.

The significant reduction of κ_{lat} can potentially improve the thermoelectric performance of the nano-grained materials[9]. Fig. 4.7 shows the ZT numbers for different samples at 50-300K. We have observed 15% and 10 % improvement of ZT in the 0.5 vol. % and 1 vol. % diamond NPs mixing samples at 300K. However, ZT is decreasing with further increasing diamond mixing ratio, which is mainly because of the reduction of electrical conductivity for samples with higher volumetric concentration, as shown in Fig. 4a. The κ_{lat} reduction is not as strong in SiO_2 mixing samples, thus we couldn't see significant improvement in ZT for the SiO_2 mixing samples. For samples with higher mixing concentration, the reduction of power factor (PF=$S^2\sigma$) will be similar or larger than the reduction of thermal conductivity, thus the ZT remains the same or decreased compared with the non-NPs mixing samples. Future focus will be on maintaining the PF while reducing the thermal conductivity by embedding NPs.

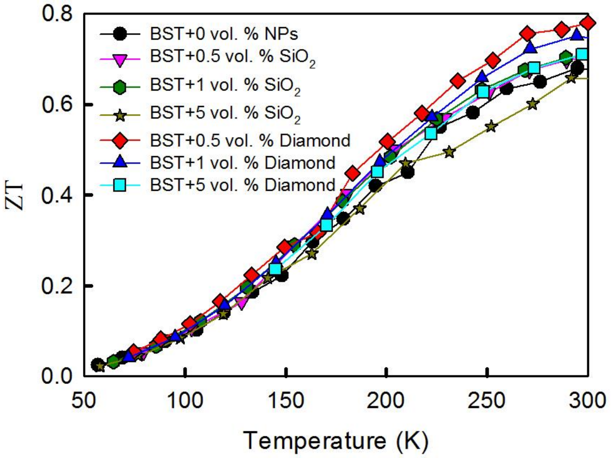

Figure 4.7: ZT for BST mixing with SiO_2 and Diamond NPs.

4.6 Conclusion

In summary, we have demonstrated the strong reduction of thermal conductivity in nano-grained BST with embedded SiO_2 or diamond NPs. The diamond NPs at 5 vol. % can effectively reduce κ_{lat} up to 41% at 300K, and 60% at 55K. The reduction is mainly due to the strong NPs scattering for the long MFP phonons. The MFP distribution of NPs/BST samples are shifting significantly toward shorter range. The phonons with MFP>10nm contribute 42% to κ_{lat} in the non-NPs BST at 300 K, but this ratio decreases to 35% and 25% in 0.5 vol. % SiO_2/BST and diamond/BST, respectively. SiO_2 and diamond NPs showed different scattering strength for the long MFP phonons, which is due to the different acoustic mismatch with the BST. The thermal boundary resistance of diamond/BST is found to be 10 times as large as SiO_2/BST. We have observed 15% and 10 % improvement of ZT in the 0.5 vol. % and 1 vol. % diamond NPs mixing samples at 300K.

Acknowledgments

Chapter 4 is a reprint of material currently being prepared for submission for publication by J. Zheng, X. Xu, R. Ihnfeldt, L. Rubin, S. Jin, and R. Chen, “Suppression of Thermal Conductivity of Nano-grained Materials by Embedding Nanoparticles at Low Temperature,” (To be submitted).

References

1. S. Ishiwata, Y. Shiomi, J. Lee, M. Bahramy, T. Suzuki, M. Uchida, R. Arita, Y. Taguchi and Y. Tokura, Nat Mater **12** (6), 512 (2013).

2. R. Wolfe and G. Smith, Applied Physics Letters **1** (1), 5-7 (1962).

3. A. Prokofiev, A. Sidorenko, K. Hradil, M. Ikeda, R. Svagera, M. Waas, H. Winkler, K. Neumaier and S. Paschen, Nat Mater **12** (12), 1096 (2013).

4. M. Koirala, H. Zhao, M. Pokharel, S. Chen, T. Dahal, C. Opeil, G. Chen and Z. Ren, Applied Physics Letters **102** (21), 213111 (2013).

5. D.-Y. Chung, T. Hogan, P. Brazis, M. Rocci-Lane, C. Kannewurf, M. Bastea, C. Uher and M. G. Kanatzidis, Science **287** (5455), 1024-1027 (2000).

6. G. Mahan and B. Sales, Physics Today **50** (3), 42-47 (1997).

7. C. P. Opeil and K. C. Lukas, in *Nanoscale Thermoelectrics* (Springer, 2014), pp. 255-270.

8. M. Koirala, H. Wang, M. Pokharel, Y. Lan, C. Guo, C. Opeil and Z. Ren, Nano letters **14** (9), 5016-5020 (2014).

9. B. Poudel, Q. Hao, Y. Ma, Y. Lan, A. Minnich, B. Yu, X. Yan, D. Wang, A. Muto and D. Vashaee, Science **320** (5876), 634-638 (2008).

10. Z. Wang, J. E. Alaniz, W. Jang, J. E. Garay and C. Dames, Nano letters **11** (6), 2206-2213 (2011).

11. C. Hua and A. J. Minnich, Semiconductor Science and Technology **29** (12), 124004 (2014).

12. Y. Dou, X. Qin, D. Li, L. Li, T. Zou and Q. Wang, Journal of Applied Physics **114** (4), 044906 (2013).

13. D. Cederkrantz, N. Farahi, K. A. Borup, B. B. Iversen, M. Nygren and A. Palmqvist, Journal of Applied Physics **111** (2), 023701 (2012).

14. Z.-Y. Li, J.-F. Li, W.-Y. Zhao, Q. Tan, T.-R. Wei, C.-F. Wu and Z.-B. Xing, Applied Physics Letters **104** (11), 113905 (2014).

15. Q. Zhang, X. Ai, L. Wang, Y. Chang, W. Luo, W. Jiang and L. Chen, Advanced Functional Materials **25** (6), 966-976 (2015).

16. K. T. Kim and G. H. Ha, Journal of nanomaterials **2013**, 8 (2013).

17. N. A. Katcho, N. Mingo and D. Broido, Physical Review B **85** (11), 115208 (2012).

18. R. Jenkins, *An introduction to X-ray powder diffractometry*. (Philips Gloeilampenfabrieken, 1970).

19. H.-S. Kim, K. H. Lee, J. Yoo, W. H. Shin, J. W. Roh, J.-Y. Hwang, S. W. Kim and S.-i. Kim, Journal of Alloys and Compounds **741**, 869-874 (2018).

20. S. Kwon, J. Zheng, M. C. Wingert, S. Cui and R. Chen, ACS nano **11** (3), 2470-2476 (2017).

21. S. Kwon, M. C. Wingert, J. Zheng, J. Xiang and R. Chen, Nanoscale **8** (27), 13155-13167 (2016).

22. L. Bulat, V. Osvenskii and D. Pshenai-Severin, Physics of the Solid State **55** (12), 2442-2449 (2013).

23. W. Kim and A. Majumdar, Journal of Applied Physics **99** (8), 084306 (2006).

24. L. P. Bulat, V. B. Osvenskii, Y. N. Parkhomenko and D. A. Pshenay-Severin, Journal of Solid State Chemistry **193**, 122-126 (2012).

25. H. S. Kim, S. I. Kim, K. H. Lee, S. W. Kim and G. J. Snyder, physica status solidi (b) **254** (5) (2017).

26. E. T. Swartz and R. O. Pohl, Reviews of modern physics **61** (3), 605 (1989).

27. J. Cheeke, H. Ettinger and B. Hebral, Canadian Journal of Physics **54** (17), 1749-1771 (1976).

28. S. Seo, K. Lee, Y. Jeong, M.-W. Oh and B. Yoo, The Journal of Physical Chemistry C **119** (32), 18038-18045 (2015).

29. H.-S. Kim, Z. M. Gibbs, Y. Tang, H. Wang and G. J. Snyder, APL materials **3** (4), 041506 (2015).

30. L. Huang, Q. Zhang, Y. Wang, R. He, J. Shuai, J. Zhang, C. Wang and Z. Ren, Physical Chemistry Chemical Physics **19** (37), 25683-25690 (2017).

31. S. Ganguly, C. Zhou, D. Morelli, J. Sakamoto, C. Uher and S. L. Brock, Journal of Solid State Chemistry **184** (12), 3195-3201 (2011).

Chapter 5: Summary and Future Work

5.1 Summary

Thermal transport in disordered materials is very important but yet is relatively less studied compared with that in the crystalline materials. Understanding the thermal transport in disordered materials is practically useful for engineering the thermal properties, including thermal conductivity and specific heat, which are important to optimize the thermal design of modern electronics devices, and improve the energy conversion efficiency in thermoelectric application.

We firstly systematically studied in-plane κ ($\kappa_{\parallel}$) of a-Si nanotubes and films of 5 nm to 1.7 μm thickness and showed strong size dependence: $\kappa_{\parallel}$ at 300 K increased from ~1.5 W.m^{-1}K^{-1} in 5 nm NT to over ~5.5 W.m^{-1}K^{-1} in 1.7 μm film. In addition, our cross-plane ($\kappa_{\perp}$) data on the same films, which are consistent with the prior $\kappa_{\perp}$ results, revealed significant anisotropy in the films. We have developed theoretical thermal model to study the underlying scattering mechanisms, including *Umklapp* scattering, impurity scattering, and two-level system scattering. The model fits very well with the temperature dependent experimental data. We also developed an MFP reconstruction model, and reconstructed the MFP distribution of the a-Si based on the size dependent $\kappa_{\parallel}$ and $\kappa_{\perp}$. The propagon MFP distribution at 300K ranges from 10 nm to 10 μm, and those with MFP greater than 1 μm contribute to ~30% of propagon κ in a-Si. Our model shows that the large anisotropy in thermal conductivity of the films is caused by the broad propagon MFP spectra and partial specular boundary scattering.

We also developed a platform to study for specific heat and thermal conductivity measurements of individual rod-like nanostructures such as nanowires and nanofibers.

This technique was demonstrated by measuring the specific heat and thermal conductivity of single ~600-700 nm diameter Nylon-11 NFs. The results showed that the thermal conductivity of the NF is increased by 50% over the bulk value, while the specific heat of the NFs exhibits bulk-like behavior. We found that the thermal diffusivity obtained from the measurement, which is related to phonon MFP, decreases with temperature, indicating that the intrinsic phonon *Umklapp* scattering plays a role in the NFs. This platform can also be applied to one- and two- dimensional semiconductor nanostructures to probe size effects on the phonon spectra and other transport physics.

Furthermore, we engineered the thermal conductivity in nano-crystalline bismuth-antimony-telluride (BST) by embedding SiO_2 or diamond nanoparticles (NPs) at temperature below 300K, which has important application in thermoelectric cooling. We have shown that the embedded NPs work as additional scattering centers for phonons, and can effectively scatter the long MFP phonons in BST. We calculated the thermal boundary resistance of SiO_2/BST and diamond/BST, and found that the diamond/BST have 10 times as large thermal boundary resistance as the SiO_2/BST. Due to the larger acoustic mismatch of diamond/BST than that of SiO_2/BST, diamond/BST samples shows stronger reduction of κ_{lat}. This reduction is mainly due to the stronger scattering on the long MFP phonons in the diamond/BST. The MFP distribution shows that the average MFP of the NPs mixing samples shift to shorter range with embedded NPs. We have observed 23% reduction of thermal conductivity, and 15% improvement of thermoelectric figure of merit (ZT) in the 0.5 vol. % Diamond NPs mixing sample, compared to the non-NPs nano-crystalline BST.

5.2 Future Work

For the thermal transport study in amorphous solid, we have studied the MFP distribution in a-Si at different temperature, but the underlying scattering mechanisms are not fully understood, especially at low temperature. We considered the anharmonic two-level-system (TLS) scattering in our a-Si in order to explain the temperature dependent data. Some previous study showed that the TLS in a-Si highly depend on the material growth conditions. It will be interesting to study the a-Si grown at different conditions with varying TLS scattering strength. Additionally, it will be interesting to study MFP distribution of other amorphous materials, such as a-Ge and a-SiGe with the platform we developed.

For the specific heat measurement, it will be useful and interesting to apply this technique on other low-dimensional structures, such as carbon nanotubes and graphenes, and observe the quantum size effect on the phonon spectrum of these nanostructures. Furthermore, since specific heat will have an abrupt change at the glass transition temperature (T_g), we can also use specific heat measurement to find the glass transition temperature in nanostructures. T_g is an important material property that indicates the transition between glassy state and rubbery state in amorphous or semi-crystalline materials. Previous research suggests that one should observe T_g deviates from bulk value as the material structure shrinks down, but further experimental work will be needed. Our specific heat measurement technique provides the possibility to study the size effect on the T_g.

For the thermoelectric cooling, future effort should be focused on minimizing the reduction of power factor when embedding NPs. Although we observed significant reduction of thermal conductivity with embedded NPs in the nano-grained BST, the improvement of ZT is not as strong. This is mainly because the power factor has degraded with the existence of NPs. Other types of NPs with varying size should be investigated to minimize the impact on power factor from the NPs. On the other hand, the BST samples we have measured showed the ZT peak around room temperature. It will be interesting to look for materials that have ZT peak at lower temperature (<200K). This will have important applications in electronics cooling in space and hydrogen storage at cryogenic temperature.